Composite Microstructures, Microactuators, and Sensors for Biologically Inspired Micro Air Vehicles

by

Robert John Wood

B.S. (Syracuse University) 1998
M.S. (University of California at Berkeley) 2001

A dissertation submitted in partial satisfaction of the
requirements for the degree of
Doctor of Philosophy

in

Electrical Engineering

in the

GRADUATE DIVISION
of the
UNIVERSITY OF CALIFORNIA, BERKELEY

Committee in charge:
Professor Ronald S. Fearing, Chair
Professor Albert P. Pisano
Professor Andrew K. Packard

Fall 2004

The dissertation of Robert John Wood is approved:

Chair Date

Date

Date

University of California, Berkeley

Fall 2004

Composite Microstructures, Microactuators, and Sensors for Biologically Inspired Micro Air Vehicles

by

Robert John Wood

Abstract

Composite Microstructures, Microactuators, and Sensors for Biologically Inspired Micro Air Vehicles

by

Robert John Wood

Doctor of Philosophy in Electrical Engineering

University of California, Berkeley

Professor Ronald S. Fearing, Chair

Unique among all nature's fliers, flying insects exhibit extreme maneuverability along with the ability to navigate in constricted environments. Advances in microrobotics, electroactive and composite materials, along with a greater understanding of the time-varying aerodynamic forces generated by insect wings have lead to the exploration of millimeter-scale flapping-wing autonomous robotic insects. The micromechanical flying insect (MFI) project has the goal of creating a flying insect capable of sustained autonomous flight. This work describes the MFI project in detail with close attention to the design and construction of a thorax and wing transmission system, high power density actuators, and the design and construction of a class of biologically inspired sensors along with empirical results from each.

Professor Ronald S. Fearing
Dissertation Committee Chair

To my grandfathers,

Dr. Paul J. Brennan,

Thomas J. Wood Sr,

my inspiration from childhood, not only in my studies but for being a man.

Contents

List of Figures

List of Tables

Acknowledgments

I wish to first thank my family for encouragement and support, my friends around the world

In particular i would like to thank Srinath Avadhanula, Joe Yan, Metin Sitti, Gabe Moy,

Part I

Introduction and Motivations

Chapter 1

Introduction

This work describes key points in the realization of an ultra small flying vehicle called the Micromechanical Flying Insect (MFI). The MFI project has the goal of producing an autonomous flying robotic insect the size of a housefly. An autonomous platform of this size would produce unparalleled maneuverability, creating numerous applications. An example of a recent version of the two wing MFI is shown in figure 1.1.

Biological insight is used for actuation, transmission, sensing, and control. To assist in the design of the MFI it is necessary to establish an understanding of various insect functions both from a performance aspect and from a need-based evolutionary stance. This reverse engineering process often yields useful shortcuts toward similar performance merits as observed in nature. Using this biomimetic approach, coupled with a new understanding of the aerodynamics of insect flight, the necessary kinematic and dynamic parameters for an insect-sized flying vehicle are realized.

Being modeled on flying insects places the MFI on a scale which is in between

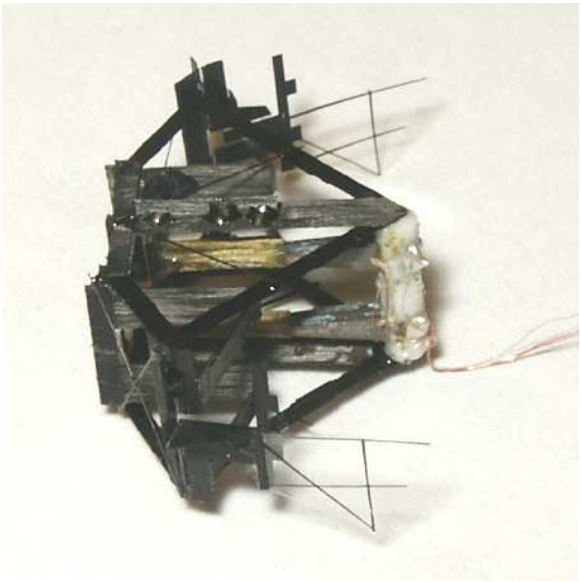

Figure 1.1: Recent two wing version of the MFI.

traditional robotics and MEMS-based microrobotics approaches. Thus it is imperative that a unique 'kit of parts' be established which recreates the performance of larger scale counterparts. This is accomplished via a number of enabling technologies all based upon layered laser-micromachined composite structures. Typical macro-scale robotics components such as pin joints, electromagnetic motors, and translational joints would not be feasible at these dimensions for reasons of friction scaling and efficiency. Also, traditional MEMS approaches are either too restrictive in material selection and available geometry, or again exhibit sub-optimal efficiency.

The overall theme for the inception of the wing drive is to create a system which is inherently controllable and can effectively transmit the input mechanical power to the wing, and thus to the air. This is done by first designing a transmission system capable of the required kinematics, then optimizing all articulating members for high stiffness and

low mass. Tuning the thorax dynamic properties is given further emphasis since the wing is driven at resonance (for reasons of efficiency). Beams which are too compliant can cause a decrease in serial stiffness and perhaps lead to either nonlinearities in plant dynamics or losses in the transmission. Links which are too heavy will cause the resonant frequency to drop, decreasing the wing velocity (and thus drastically decreasing the work done on the air). Thus it is of the utmost importance that all structural members be as stiff and lightweight as possible. A novel thorax design incorporating composite materials will be introduced and shown as an enabling technology for such a device at this scale.

Another key aspect of the MFI design is the creation of high power density actuators. Such actuators are based upon electroactive materials and use a number of techniques which allow the active materials to be driven very close to their strain limit. It will be shown that these actuators exceed the performance of similar commercially available platforms by orders of magnitude and can rival the performance of traditional electromagnetic motors. Other important considerations that will arise are the losses inherent in each active and passive member both for power delivery calculations and controllability.

Insects use a hierarchical sensor modality control architecture to traverse their environment. With limited computation available, fixed-optics, and binary strain sensors, insects are somehow able to exhibit extreme maneuverability in tight environments. Using the same principles, a biomimetic sensor suite is constructed and verified, showing the feasibility of recreating a simple insect-like control system.

The overall objective of this work is to create an entomologically inspired MAV with the ability to generate sufficient lift while minimizing mass so as to allow the recreation

of flying insect maneuverability. While the final goal of the MFI project is to create an autonomous flying insect, the figure of merit here is a step along this path; the development of an insect sized structure capable of generating a lift-to-weight ratio of greater than unity through the use of two flapping wings.

1.1 An Introduction to Micro Air Vehicles

The need for more encompassing surveillance and reconnaissance as well as search and rescue operations in hazardous environments have motivated the recent advances in micro air vehicles (MAVs). Micro air vehicles are generally defined as being small ($< 30cm$) and lightweight ($< 100g$) though the range of devices which fit in to this broad category can be of the order of a large bird to small flying insects. Such platforms can offer the advantages of disposability, extreme agility in flight, and portability that emanate from their small scale, high power-to-weight ratios, and inexpensive manufacturing that are inherent with such low mass. Because of the small scale, many MAVs can be transported and deployed with limited resources. Additional payload could include any number of sensing technologies, which coupled with RF communications can produce mobile networks capable of a wide variety of tasks.

The size of MAV platforms has interesting aerodynamic implications displayed in part in Figure 1.2. As displayed in Figure 1.2, as the size of the flying body is reduced, the Reynolds number decreases in a similar fashion. The Reynolds number is the ratio of the fluid inertial forces to the fluid viscous forces and is defined as follows:

$$Re = \frac{vL\rho}{\mu} \tag{1.1}$$

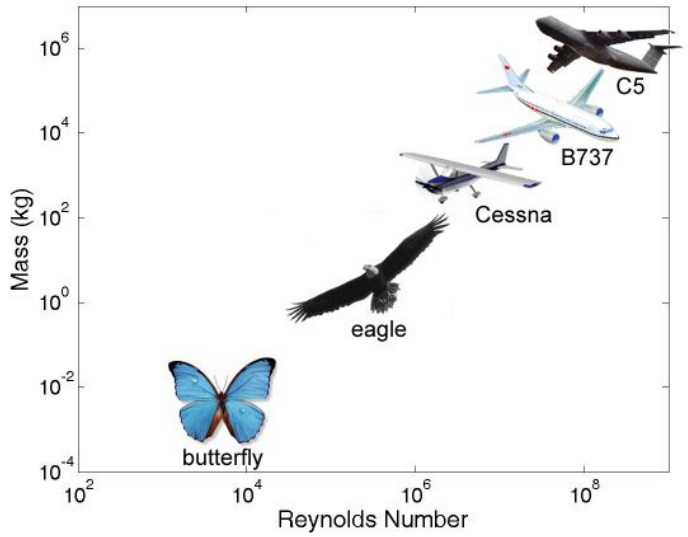

Figure 1.2: Reynolds number and mass for various flying bodies, demonstrating an inherent aerodynamic relationship.

where v, L, ρ, and μ are the mean fluid velocity, characteristic length, fluid density, and fluid kinematic viscosity respectively. Thus smaller flying vehicles are less effected by the fluid inertial forces and more influenced by viscous fluid forces. For an MAV the size of a flying insect, the surrounding air feels more like a viscous fluid to its wings, and noteworthy aerodynamic effects from this are involved. The Reynolds number indicates what fluid flow near and around the airfoil is like: low Re implies laminar flow and high Re (> 2000) indicates turbulent flow. Note that in order for a flying vehicle to remain in the same flow regime as the size decreases, the Reynolds number must remain the same. Thus from equation 1.1, to maintain the same aerodynamics as the size is reduced, the velocity of the airfoil with respect to the surrounding fluid must increase.

One way of normalizing aircraft and flying animal airfoils irrespective of size or flow conditions is to use the lift and drag coefficients. The lift and drag coefficients are

typically an empirical measurement and are defined as follows [30]:

$$C_{\{L,D\}} = \frac{2F_{\{L,D\}}}{v^2 S\rho} \tag{1.2}$$

where $F_{\{L,D\}}$ are the lift and drag forces and S is the characteristic area of the airfoil (most often the planform wing area).

Micro air vehicles can be split into four categories: fixed wing, rotary wing, flapping wing, and lighter-than-air. Examples of each these will be discussed in section 2, however the benefits and drawbacks of each class of MAV will be discussed first here with respect to the desired performance metrics.

Fixed wing MAVs have the obvious benefits of simple construction because of minimal moving parts, possible passive stability, and the possible use of standard aerodynamic modeling tools for analysis. However, as at the macro scale, fixed wing miniature aircraft cannot hover and thus the maneuverability is limited by its flight speed and turning radius. Also, as discussed above, small vehicles need to fly faster than their larger counterparts to generate the same lift. This creates problems in increasing the controller bandwidth, decreasing the maneuverability, and putting harder constraints on the power source to overcome drag.

At this point it is of use to introduce the concept of the D/R ratio as a figure of merit for maneuverability. The maneuverability of a vehicle can be quantified by the distance to the the nearest obstacle ('D') divided by the smallest possible turning radius ('R').

Rotary wing micro air vehicles have the capability of hovering and thus the D/R ratio is very large. However, the airfoils still rely upon quasi-steady airflow and thus the

rotors are required to spin faster for the same reasons fixed wing micro air vehicles require relatively high velocities. Also, rotary motors and gears at the micro scale can create further complications due to the increased percentage of surface area exposed to frictional forces as the size decreases.

Flapping wing micro air vehicles on the size scale of a bird have an advance ratio on the order of unity and thus they take advantage of a combination of quasi-steady and unsteady aerodynamics. However, of the current prototyped ornithopter micro air vehicles, none have the ability to hover. Flapping wing MAVs which have the capability to glide such as in butterflies (order Lepidoptera) and dragonflies (order Odonata) can be passively stable. Motor efficiency for flapping wing MAVs can be increased by running at mechanical resonance since the wing motion is in general periodic. Flapping wing micro air vehicles of insect size will have a Reynolds number which is approximately in transitional region between the laminar and turbulent flow ranges. As such, insects utilize a number of aerodynamic mechanisms, both steady and unsteady as will be described in section 1.2.

Although lighter-than-air MAVs can hover without expending power, they are generally too large (on the order of $1m$) and thus cannot traverse the regions of interest for this study and will not be considered further.

The MFI will be initially based entirely upon typical two wing flying insects. A typical blowfly (*Calliphora erythrocephala*) has a wing span of approximately $25mm$ and a mass of $100mg$. Thus, the scale of the MFI is smaller than any current micro air vehicle platform. The recreation of insect flight capabilities will also place the MFI as the most maneuverable MAV platform in existence.

1.2 Biological Motivations

The inspiration for the micromechanical flying insect project comes from the functionality and morphology of flying insects of the order Diptera. Such insects have evolved into efficient fliers through the evolution of two wings with three degrees of freedom (DOF) each. The MFI is based upon the parameters of the blowfly *Calliphora* which can be summarized in Table 1.1. Dipteran wings have 3 degrees of freedom: flapping, pronation and supination (henceforth rotation about the wing longitudinal axis), and stroke plane deviation. It has been suggested in [92] that the out-of-plane motion does not contribute significantly to the insect lift generation (though it may have a significant effect on maneuverability). Thus the MFI wings will need only two DOFs.

Table 1.1: Parameters for the blowfly *Calliphora*.

Parameter	Notation	Value	Units
Actuator mass	m_a	50	mg
Actuator power	P_a	10-20	mW
Actuator power density	D_P	200-400	$kWkg^{-1}$
Wing power	P_w	5	mW
Wing span	l_w	11	mm
Wing inertia	J_w	20	$mg \cdot mm^2$
Quality factor	Q	1-3	—
Wing beat frequency	f_0	150	Hz
Flapping amplitude	A_f	± 60	$^\circ$
Rotation amplitude	A_r	± 45	$^\circ$
mass	m	100	mg

Recent breakthroughs have given insight into the method of insect flight [27, 33]. Previous studies in insect flight using steady state aerodynamic analysis have predicted insufficient lift force required for flight given the insect's body mass. To determine the origin of the actual lift forces, a large dynamically scaled model of two *Drosophila melanogaster*

wings were created by Dickinson [27]. Each of these wings is capable of the same 3DOF motion as the actual insect's wings. Obtaining the same Reynolds numbers for both real insect flight and a scaled simulation assures that the proper ratio between viscous and inertial air forces on the wings, giving a true account of the force coefficients and thus the forces seen by the insect during flight. For this dynamically scaled model with a wing span of $25cm$, the wings are immersed in a tank with two tons of mineral oil and flap at low frequency ($< 1Hz$). A high speed, 3-dimensional imaging system then records video images of a *Drosophila* in various free flight situations. These recorded sequences are then explored off line to extract the insect's wing kinematics. These kinematics are then played back through Robofly and the forces and moments acting on the wings are recorded through the use of force sensors at the proximal end each scale model wing while a particle image velocimetry (PIV) system records the wing vorticity at various times during the stroke by illuminating air bubbles infused in the mineral oil.

The measured forces and moments can be used to directly calculate the lift and drag force coefficients (via equation 1.2) for the *Drosophila* and other flying insects of similar size, but more importantly, they give a real time estimate of the actual lift and drag that the insect sees during flight. During hovering, for example, steady state blade element analysis predicts approximately one half of the lift force required to keep the insect in the air [33]. The complete analysis performed over the entire wing stoke shows three distinct lift generation modes collectively termed the unsteady aerodynamics [27]. During hovering flight the wings undergo a large wing stroke of roughly constant velocity and angle of attack, a quick rotation or wing flip, then a stroke reversal. The first mode of lift generation occurs

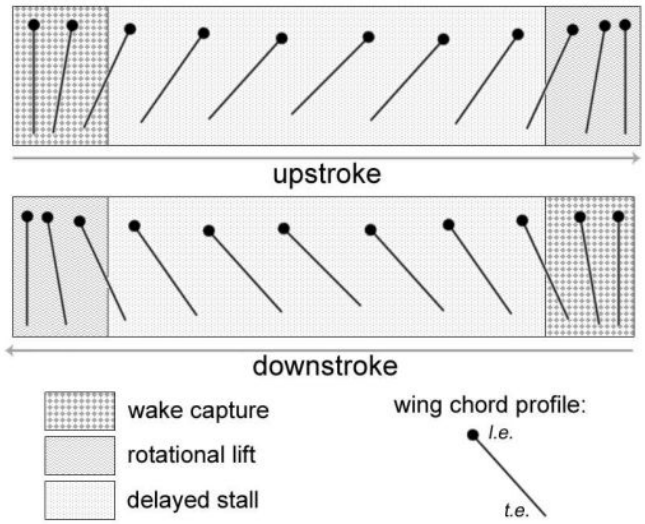

Figure 1.3: End on view of mean wing chord through one complete wing stroke (wing positions all have approximately equal temporal spacing). $l.e$ and $t.e$ are the leading and trailing edges respectively.

during the constant angle of attack portions of the wing stroke is termed delayed stall and is analogous to steady state aerodynamics. The second mode occurs during the wing flip and is termed the rotational lift. The last is achieved during the stroke reversal when the wake from the previous stroke is collected or captured, thus called wake capture. Figure 1.3 shows the detail of a typical insect wing stroke seen at the chord, again only considering flapping and rotation. The first mode of insect lift generation is derived from steady state aerodynamics. The kinematics of the wing during this mode consist of a nearly constant velocity and constant angle of attack. The typical angle of attack in this region is very high relative to traditional airfoils. A commercial jet operating at cruising speeds will stall at only a few degrees angle of attack due to unbound leading edge vortex growth and subsequent shedding. Initially it was thought that an insect is able to maintain a very high

angle of attack by continuously shedding its vortex along the span wise axis during the stroke. However it was shown by Birch et. al. that the mechanism for controlling vortex growth is associated with the downward flow of tip vortices [25]. Also, the Wagner effect causes the vortex not to stabilize until approximately 7-8 chord lengths are traveled [30]. Thus the leading edge vortex is not allowed to grow unstably, high angles of attack are achieved, and large lift is generated.

The second mode of insect lift generation is called rotational lift and occurs at the end of the wing stroke when there is a rapid wing rotation or wing flip (see Figure 1.3). This mode of lift generation arises from enhances wing circulation from the rotating wing analogous to that of a spinning baseball [27]. Also, the insect has control over when the flip begins and ends during the wing stroke. Thus it can modulate the magnitude of the lift generated by the rotation as well as the moments generated which contribute to both pitch and roll body torques.

The third and final mode of lift generation derives from captured fluid from previous half strokes. There is a pocket of trapped fluid traveling behind the wing during each wing half stroke. After the rapid rotation and stroke reversal, this fluid is traveling in the opposite direction of the wing, doubling the effective wing velocity with respect to this fluid. This is seen as spikes in lift generation at the stroke reversals (see [27]).

These three combined unsteady aerodynamic effects yield an average lift to weight ratio of approximately 2 for a *Drosophila* or *Calliphora*. Ancillary benefits of this mode of lift generation are the relatively simple creation of body torques on a stroke-by-stroke basis. Wing motion is achieved by the dorsolongitudinal and dorsoventral indirect flight muscles

acting to displace the notum with respect to the rest of the thorax (in a similar way as the MFI flight muscles displace sections of the thorax with respect to the exoskeleton) [30]. Insects can control the timing of wing flips, relative bilateral wing stroke amplitudes, and flip duration for each stroke via flight musculature acting directly on the pleural wing process [37].

Despite limited computational power, flying insects exhibit excellent capabilities in traversing their environments. This is due not only to excellent maneuverability, but a set of simple, yet effective inertial and photoreceptive sensors. Ancient insect of this order had four wings, much like the present day dragon flies (order Odonata). Flies of the order Diptera evolved such that their hind wings did not perform any aerodynamic function, but instead serve as gyroscopic devices [59]. These devices have the characteristics of very high sensitivity at high angular rates [60]. Along with the halteres of insects of the order Diptera, photoreceptive sensors called the ocelli and the compound eye can be used for angular and linear velocity estimation, horizon detection, orientation estimation, and obstacle avoidance [71].

It has been hypothesized that insects use different subsets of their sensors for different flight modes [72, 24]. Example flight modes could be hover, fly straight, saccade left, etc. For each of these modes, one or more sensor is used for stabilization or obstacle avoidance, depending upon the bandwidth of the sensors and the desired motion. For example in straight flight, insects may use ocelli for stabilization with respect to the horizon while observing optic flow with their eyes for obstacle avoidance. As soon as an optic flow threshold is reached (i.e. an object is rapidly approaching the image plane), a saccade

is triggered [37]. During the saccade, the haltere is used to stabilize the turn since the angular velocities experienced by the fly can be much too large for optic flow mediated turns ($> 1000° s^{-1}$ [60]). After a fixed time has elapsed, the fly will switch back to straight flight and the sequence begins again.

Creating an autonomous flying robotic insect presents many challenges to the engineer. However, evolution has many millions of years to come up with many solutions to these problems. The knowledge of the workings of these biological mechanisms forms the basis for the design of a two-wing flying robotic insect.

1.3 An Introduction to the Micromechanical Flying Insect

The evolution of the MFI obviously does not have the luxury of millions of years, but also does not have the availability of any off-the-shelf (OTS) components for use in the construction. To achieve the wing beat parameters described in section 1.2 using the technologies available from current micro air vehicles described in section 1.1 would not be possible since the MFI is working on a difficult and scarcely explored size scale. Micro air vehicles with dimensions of a few tens of centimeters can utilize commercial off the shelf (COTS) micro motors such as ultrasonic or small electromagnetic (for example the $91mg$ Faulhaber micro brushless DC motor). At the scale of the MFI, such motor power densities drop off rapidly and gears or bearings exhibit friction problems. For microrobots on the scale of a millimeter, high force, small displacement combdrive motors are available in MEMS processes. However, joints such as hinges or flexures are very brittle and not typically capable of large deflections. Thus all components of the MFI must be invented or

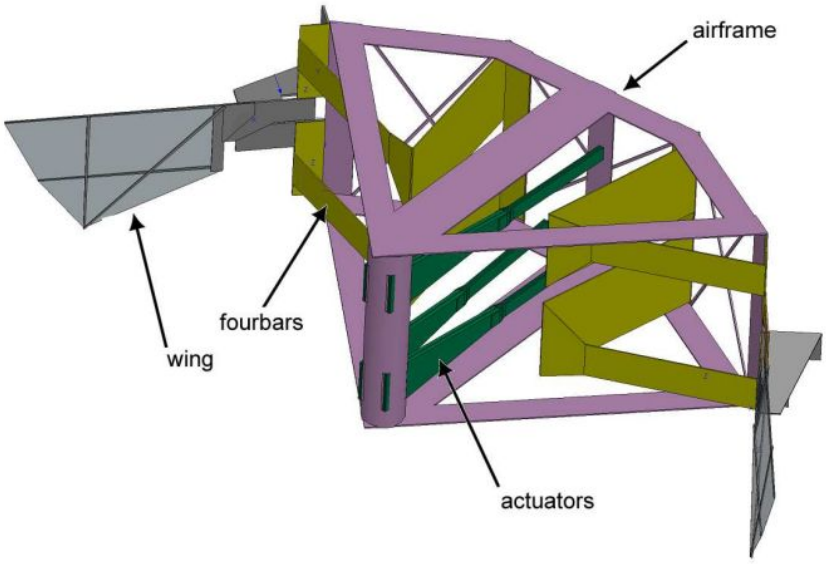

Figure 1.4: Drawing of the MFI showing relevant areas of discussion.

adapted from other technologies.

The MFI is split up into four distinct mechanical components: the thorax, wings, actuators, and airframe. A drawing of the MFI showing these four constituent components is shown in Figure 1.4. The actuators are analogous to the direct and indirect flight musculature of Dipteran insects [29]. The MFI thorax consists of a mechanical amplifier and a differential mechanism which is connected ultimately to a wing. The airframe is a tensegrity-based exoskeleton which serves as a mechanical ground for all the drive components. The MFI mechanical design and fabrication techniques are described in detail in chapters 3 and 4.

The flight muscles of the MFI are piezoelectric bending actuators. With respect to the MFI application, this class of actuators has small displacements and relatively large generative forces. In order to drive the wings through large angles, a mechanical amplifier

is used. Instead of gears and rotary joints, a planar parallel flexure-based mechanism (four bar) is used. This accepts a rotary input and yields an amplified rotary output. To generate the rotary input, a slider-crank mechanism is used to transform the approximately linear motion of the actuators to a rotation at the input of the four bar. For each wing, two actuators, four bars, and slider-cranks are symmetrically opposed. The outputs of the two four bars are mapped through a spherical parallel differential mechanism (five bar) such that in-phase rotations yield flapping while out-of-phase rotations cause rotation about the span wise wing axis. A slider-crank mechanism is used to transform the approximately linear motion of the actuators to a rotation at the input of the four bar. For each wing, two actuators, four bars, and slider-cranks are symmetrically opposed. The outputs of the two four bars are mapped through a spherical parallel differential mechanism (five bar) such that in-phase rotations yield flapping while out-of-phase rotations cause rotation about the span wise wing axis. The dual four bar, slider-cranks, and differential are collectively termed the thorax.

In addition to the mechanical transmission and actuation, a class of biologically inspired sensors has been designed and demonstrated which exhibit advantages over existing commercial sensors. The proposed control of the MFI relies on these biomimetic sensors for state estimation such as angular position and angular velocity. Chapter 5 describes a biomimetic gyroscope (halteres), angular position sensors (ocelli), and an optic flow sensor for angular and linear velocity estimates.

Finally, the actuators, thoraxes, wings, and airframe are assembled together to form the complete mechanical body of the MFI as described in chapter 6. Along with this

mechanical integration, the wings are driven with biomimetic kinematics and a liftoff test is performed.

Chapter 2

Previous Work

There has been a great deal of interest in unmanned air vehicles (UAVs) and more specifically micro air vehicles (MAVs or μAVs) recently. In general, although not exclusively, such work is focused upon the use of fixed or rotary wings.

AeroVironment developed the "Black Widow", a six inch fixed wing MAV with DARPA support. This MAV has a range of $1.8km$ flying for $30min$, though the maneuverability is limited due to a $14ms^{-1}$ flight speed.

Researchers at Didel and EPFL [62], and Drexel University (Closed Quarter Aerial Robotics [44]), have created a class of indoor slow flyers capable of extremely slow flight and thus impressive maneuverability in closed environments. Such fixed wing MAVs are as light as $6g$ and can operate in rooms the size of small gymnasiums as slow as $1ms^{-1}$.

A team at Stanford University headed by Ilan Kroo attempted to create a quadrotor MAV the size of a quarter called the Mesicopter. This consisted of four rotors mounted to a fuselage housing a battery and controller. Prototypes of the Mesicopter showed the

ability to generate thrust, but also displayed the inherent instability of such structures at the small scale.

Epson corporation has produced a counter-rotating blade miniature autonomous helicopter. This MAV is powered by ultrasonic motors, weighs $12.3g$, and has a flight time of $3min$. Similar to Epson's MAV, a more traditional style rotocraft was constructed in 2003 by a Belgian hobbyist Alexander Van de Rostyne. This is a remote controlled $6.9g$ helicopter constructed mainly from composite weaves and carbon tubes.

It is understood that as the size of the UAV becomes smaller, the Reynolds number becomes smaller, thus fixed wings become less efficient for lift production because of the need for increased speed. Flapping or rotating airfoils solve this problem by increasing the speed of the wings relative to the surrounding fluid. Goldfarb [17, 41] noted this as the motivation for his piezoelectrically actuated flapping wing MAV prototype. This MAV attempted to mimic the functionality of a dragon fly using resonant, piezoelectrically actuated wings. Two wings were actuated by a single drive actuator at the system resonance. The wings were tuned such that bilateral wings had identical flapping resonances, but slightly different rotational resonances [16]. In this way, roll torques could be generated via slight variations in the drive frequency such that one wing achieved larger rotation amplitudes.

Robert Michelson at Georgia Tech is leading an "Entomopter" project geared at creating a multimodal aerial robot [57] using reciprocating chemical muscles to power the $100g$ $4DOF$ flapping wing device.

At team at the California Institute of Technology in collaboration with researchers at the University of California at Los Angeles and AeroVironment has created a biologically

inspired ornithopter dubbed the Microbat [68, 67]. Using the principles of birds and flying mammals, the microbat generates reciprocating wing motions through an electromagnetic drive and is capable of remote control for a few minute span.

Under the leadership of Sunil Agrawwal at the University of Delaware another ornithopter has been created and has also demonstrated stable flight [6].

Thus there has been significant work on the creation of MAVs and microrobotcs in general, however the underlying mechanisms and principles are quite diverse. Researchers at the University of California at Berkeley have used polysilicon hinges and panels to create rigid links and flexible joints [106] for a solar powered crawling microrobot [105, 47]. Another walking microrobot was constructed using thermally actuated hinges as legs [31]. On a larger scale, Goldfarb [38] actuated vibrating legs with piezoelectric materials to create a hopping microrobot. With respect to the MFI project, Shimada discussed a semi-automatic desktop microassembly plant, Fearing described the initial wing drive of the MFI [35], Yan further described the prototyping methods used [103], Avadhanula [3] and Wood [96] described initial composite process and the dynamic tuning of each member.

There have been numerous models presented for the mechanics of rectangular piezoelectric transducers. DeVoe [23] presented a model for MEMS cantilever actuators considering multiple passive layers. Smits [77, 78] and Weinberg [93] described in detail a one-dimensional analysis of piezoelectric bending actuator performance using energy methods. More specific to this work, Wang [87] modeled a bimorph with a central passive layer and the effects thereof. For microrobotics applications, Sitti [76] described the design of millimeter scale bending actuators. For greater generality, laminate plate theory is used in

chapter 3 to describe the interaction between the external and internal forces and moments with the layer stresses and strains as in [98, 99].

Other than modeling, there have been a number of novel construction techniques for piezoelectric bending actuators. Goo [42] and Yoon [108] have described the construction and performance of a lightweight piezocomposite curved actuator (LIPCA), Wise [94], Li [53], and Wang [88] have characterized the performance of reduced and internally biased oxide wafer (RAINBOW) and thin unimorph driver (THUNDER) actuators.

There have also been a myriad of biomimetic sensor work suitable for such platforms. Wood described force sensors [97] mounted along electro-active actuator surfaces analogous to campaniform sensilla in insect wings and legs. Chahl [12] created a horizon detection sensor similar to insect ocelli. Barrows [8] described an optical flow sensor suitable for obstacle avoidance and navigation for highly maneuverable MAVs. It is hypothesized that the algorithms used in such a sensor are similar to those used by insects to process their visual data with high temporal resolution and low spatial resolution. Simple and efficient versions of these sensors along with additional sensor platforms will be discussed in Chapter 5.

2.1 Contributions

This work brings benefits to the fields of microrobotics, robotics in general, material science, electrical and mechanical engineering through the following contributions:

1. The development of a laminate plate theory model for bending transducers encompassing any number or orientation of layers, intrinsic and extrinsic geometry, and

excitations.

2. The demonstration of an optimal bending actuator design using this model displaying the usefulness of the model and the exemplary performance of actuators with respect to the state of the art.

3. The creation of a process to utilize composite materials into articulating and statically determinate microrobotic structures and the demonstration of the benefits relative to previous methods.

4. The development and demonstration of a class of biomimetic sensors for use in low mass, low power mobile platforms.

5. The overall integration of actuators and thorax into an MAV platform capable of generating a thrust to weight of greater than unity.

Part II

Design and Fabrication of a Biologically Inspired Flying Robotic Insect

Chapter 3

Composite Microactuators

The flight muscles of flying insects pull either indirectly (dorsolongitudinal and dorsoventral muscles) or directly (subalar and basalar) on a wing drive transmission to power the wings [30]. This is true also for the MFI wing muscles. The MFI actuators are essentially a force source. They pull (or push) upon either the wing directly, or indirectly through a transmission system. Such a transmission system is necessary to tailor the kinematic and dynamic properties of the MFI wing to the requirements and is described in chapter 4. The MFI must have two wings, each with two DOFs for a total of four independent DOF. Thus the MFI requires four actuators. This chapter describes in detail the requirements, design, fabrication, and results of these actuators along with a comparison to other published and commercial piezoelectric bending actuators.

First it is of use to note the motivations behind the choice of actuator morphology. It has already been stated that rotary micromotors would be too inefficient due to higher friction as the size decreases. The rotary motor which is the closest to fitting the needs of

Table 3.1: Active material parameters.

Material[1]	PZT-5H	PVDF	PMN	Terfenol-D	Nitinol[2]	Units
Description	piezo-ceramic	piezo film	electro-strictive	magneto-strictive	SMA	
Max. Strain	0.3	0.07	0.1	0.2	8.0	%
Modulus	62	2	65	30	41	GPa
Density	7800	1780	7800	9250	6500	kgm^{-3}
Energy Density	36	0.28	4.17	6.48	20000	Jkg^{-1}

[1]from Mide (www.mide.com) and empirical measurements

[2]data form www.nitinol.com

the MFI is the Faulhaber 0206 drive system. This motor has an output power of $60mW$ and a mass of $91mg$. Very high shaft speeds and relatively low torques would require this motor to have a gearing system that would further reduce the power density below the acceptable range for the MFI. Thus a frictionless alternative would be ideal. The needs of the wing drive, as alluded to in chapter 1 tend to suggest the use of an oscillating actuator since the desired wing motion is periodic. Of these oscillating actuators, three morphologies are common: stacks, domes, and bending cantilevers. Stacks have the characteristics of large force generation, small displacements and high bandwidths. Bending cantilevers use geometric constraints to create relatively large motion with a reduction in force production while domes bridge the gap between these two extremes. Bending actuators are used for this application since large displacements are the goal for the wing drive.

Next, the class of actuator material should be chosen. Active materials can take on a number of forms generally classified by energy domain: electric, magnetic, or thermal. Table 3.1 gives a comparison of example active materials of various classes. Shape memory alloy have the highest energy densities, however they typically have low bandwidths and are thus not appropriate for this application. Alternatively, electroactive materials have decent

energy densities and typically high bandwidths (depending upon morphology). Thus, the choice between piezoelectric and electrostrictive dissolves to logistics. Piezoelectric materials are chosen since they can achieve high strains at much lower fields than electrostrictive materials and since the field-strain relationship is approximately linear for piezoelectric materials and quadratic for electrostrictive materials.

In considering the design of induced strain actuators, and particularly for bending morphologies, the key issue is how to bring each infinitesimal electroactive element close to its fracture strain. In doing this a number of key questions must be addressed: what is the fracture toughness and can this fracture toughness be improved, how can you get uniformly distributed strain throughout the actuator, and how hard can you drive the active elements (both internally and externally). These questions will be addressed in sections 3.2, 3.3, and 3.5 respectively. Next, once the design is complete, the quasi-static performance is evaluated and reported in section 3.6. Such actuators are traditionally notorious for having static nonlinearities. These will also be examined in section 3.6. Finally, the dynamic model and power delivery capabilities will be discussed in 3.7.

Most high performance piezoelectric materials are subject to defects because of their ceramic or crystalline structure. This does not show up so much in the use of these materials for sensing applications (an exception being sensors which experience high hydrostatic pressure, for example sonar applications), however this is a major factor when using piezoelectric materials as part of unimorph or multimorph bending actuators. Surface and edge defects from processing or growth are initial cracks which cause stress concentrations limiting the usable working stress range, thus lowering the strain energy compared to a

defect free sample. The fracture mechanics of piezoceramics and methods for improving the fracture toughness are discussed in section 3.2.

3.1 Requirements and Design

The flight muscles for a flying robotic insect must meet extremely stringent power and mass requirements. In most applications, needs for greater mechanical energy are met by increasing the volume of the actuator material used. The MFI does not have this liberty since the mass budget allotment for the actuators is set at approximately $50mg$ (to be discussed in chapter 4). Thus, a minimum of actuator material must be used in an optimized manner to deliver the required power to the transmission.

3.1.1 Power requirements

Lehmann and Dickinson [51] estimated the power density in the indirect flight muscles of *Drosophila melanogaster* to be at most $200Wkg^{-1}$. This number was subsequently updated to show that when necessary (for escape, for example) this can be increased by a factor of two [52, 26]. However, it should be noted that insects can deliver this power to their wings very efficiently. Thus, the MFI actuators use a baseline minimum of $400Wkg^{-1}$ for design. For performance comparisons, the mechanical energy is defined as the area under the force-displacement curve:cessary (for escape, for example) this can be increased by a factor of two [52, 26]. However, it should be noted that insects can deliver this power to their wings very efficiently. Thus, the MFI actuators use a baseline minimum of $400Wkg^{-1}$ for design. For performance comparisons, the mechanical energy is defined as the area under

the force-displacement curve:

$$U_m = \frac{1}{2} F_b \delta_{max} \tag{3.1}$$

where F_b and δ_{max} are the peak-to-peak blocked force and unloaded maximum tip displacement respectively for a given field. This work assumes that the actuators are driven quasi-static ($f << f_0$), thus the power is a linear function of the drive frequency. However for such actuators driving resonant systems ([4, 96, 103]) the power able to be delivered to a given load is a function of internal dissipations. The dissipation effects on the power delivery capabilities for resonant systems are quantified in equation (3.2).

$$P = \begin{cases} \frac{1}{8} 2\pi f_0 F_b \delta Q_l & \text{for } Q_a >> Q_l \\ \frac{1}{16} 2\pi f_0 F_b \delta Q & \text{for } Q_a \approx Q_l \end{cases} \tag{3.2}$$

In equation (3.2) f_0 is the total system resonant frequency and the mechanical Q (Q_a and Q_l are for the actuator and load respectively) is a function of the lumped system stiffness, mass, and loss: $Q = \sqrt{km}/b$. Section 3.7 describes the complete dynamic model of the actuator and estimates the power delivery capabilities for known wing and thorax parameters. Thus, until section 3.7, energy density will be the performance metric used. Table 3.2 lists the energy densities for commercially available piezoelectric bending actuators.

Note that the magnitudes of the applied fields in Table 3.2 for the first two actuators are small compared to the field applied to the bimorphs in question ($> 2V\mu m^{-1}$ as will be discussed in section 3.5). There are four key factors that can limit the magnitude of field applied to piezoelectric actuators: mechanical failure (fracture), electrical failure (dielectric breakdown), depolarization, or saturation of the piezoelectric effect. Bimorphs connected in series or parallel to the drive source are limited by depolarization (as is the case with

Table 3.2: Commercially available clamped-free cantilever piezoelectric bending actuator specifications.

Actuator	δ_{max} [1] (μm)	F_b [1] (mN)	m (mg)	D_U (Jkg^{-1})	Field [2] ($V\mu m^{-1}$)	Piezo Mat. [3]
T219-H4CL-103X [4]	610	160	320	0.153	0.25	5H
QP21B [5]	790	460	2800	0.065	0.50	5A
TH-8R [6]	1900	111	1780	0.059	1.75	5H
optimized bimorph [7]	520	123	12	2.730	2.36	5H
Max. strain energy density for bulk free plate[8]				4.0	2.5	5H

[1] peak to peak

[2] maximum drive field

[3] either PZT-5H or PZT-5A

[4] Piezo Systems (www.piezo.com)

[5] Mide QuickPack actuators (www.mide.com/quickpack/qp_pricelist.html)

[6] THin layer UNimorph DrivER and sensor from Face Thunder (from empirical measurements and www.face-int.com/thunder/thunder.htm)

[7] strain-optimized bimorph micro-actuators for the MFI

[8] for d_{31} actuation

the first two actuators in Table 3.2). Unimorphs are not subject to depoling so long as the field is unipolar in the poling direction, or a small magnitude bipolar field. The THUNDER actuators in Table 1 are unimorphs and the field limit listed is based upon commercial specifications. The actuators described here are limited by breakdown and mechanical failure; little saturation has been observed before either electrical or mechanical failure. It is important to note that it is not only the driving method that allows these actuators to be driven at such high fields. The intrinsic and extrinsic geometry modifications give the capability to run the actuator at fields which would fracture traditional rectangular bimorphs. All peak field data for commercially available actuators shown in Table 3.2 are directly quoted from the manufacturer.

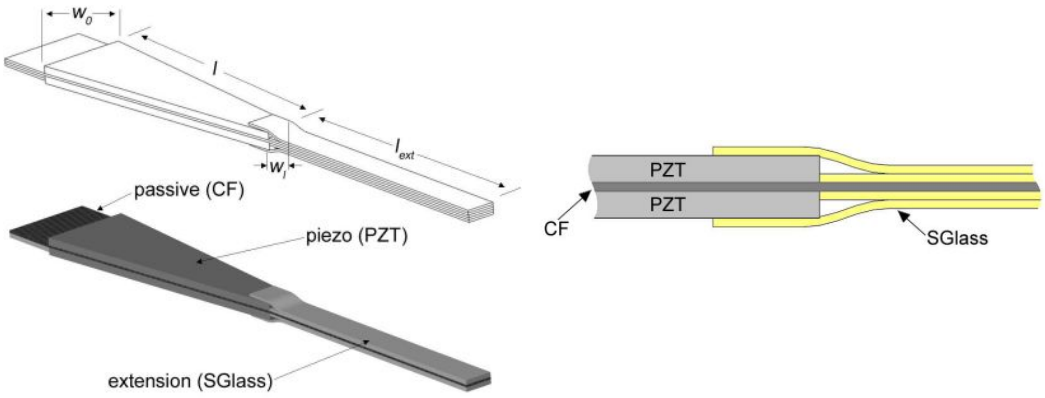

Figure 3.1: Bimorph drawing with pertinent dimension descriptions.

3.1.2 Design Preliminaries

Figure 3.1 show drawings of the bimorph actuators for design purposes. Note that the width is tapered along the length; the actuator geometry will be discussed in section 3.3. Also, the elastic (passive) material is drawn as one material. In reality, however, it could be composed of a number of layers in arbitrary orientations as will be discussed in section 3.1.3. The extension will be described in section 3.3.2.

3.1.3 Laminate Plate Theory for the Design of Multilayer Bending Actuators

Throughout the following discussion, there are a number of assumptions that are made. First, the amorphous ceramic piezoelectric materials are assumed to be transversely isotropic, that is $d_{31} = d_{32}$ and $d_{36} = 0$. This is only true for the case of amorphous piezoelectric materials, for single crystal materials the piezoelectric constant will very with the orientation relative to the crystal directions. However, if the crystal is cut properly so that the crystal planes are aligned to the actuator geometry, then this assumption holds for

the single crystal case as well. Second, there is no external axial loading, only transverse loading which is applied at the distal end of the actuator. Also, this loading is assumed to be uniformly distributed along the width of the distal end. Third, the bonding between each layer is assumed to be perfect, that is, there are no shear strains between layers. Fourthly, for all laminate calculations, the laminates are considered free from moisture and any moisture-induced strains. Similarly, for thermal calculations, there is no gradient in temperature through the thickness of any lamina. These last two simply state that the lamina properties do not vary through the thickness. Also, electrostriction and higher order effects are ignored. Since the stresses within the piezoelectric layers will vary through the thickness during normal operation, electromechanical coupling of the material can change the effective field in that layer. The effects on actuator performance based on this effect have been quantified [83]. From this study, the error from the electromechanical coupling is a function of k^2, which is small for the piezoelectric materials used. Finally, since the actuator width is much greater than the thickness, a plane strain state is incurred where $\epsilon_y == 0$ [93]. This causes the Young's modulus and piezoelectric properties to be modified as follows:

$$\begin{aligned} E_i &\rightarrow E_i \left(1 - \nu_i^2\right)^{-1} \\ d_{31} &\rightarrow d_{31} \left(1 + \nu_i\right) \end{aligned} \tag{3.3}$$

Figure 3.2 shows the cross section of a laminate consisting of an arbitrary lamina layup. This will be used to define the lamina geometry throughout this section. Applying an electric field to a piezoelectric layer creates a strain in a free plate. When there are passive elastic layers bonded to piezoelectric layer, motion is restricted and a stress develops. If the constituent layers are not symmetric in geometry and elasticity there is an effective moment

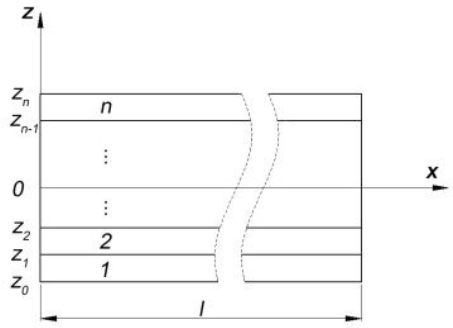

Figure 3.2: Actuator layup for arbitrary lamina materials and ply angles.

in the beam, causing a deflection. The strain in any layer is given by the following:

$$\epsilon_1 = \frac{1}{E}\sigma_1 + d_{31}E_3 p + \alpha_1 \Delta T \tag{3.4}$$

where σ is an applied stress, E_3 is the electric field, α is the coefficient of thermal expansion (CTE), and ΔT is the change in temperature, which for this application is the change from the cure temperature to room temperature (curing details are given in section 3.4) . The p term in (3.4) is a placeholder which is defined as follows:

$$p = \begin{cases} 1 & \text{field parallel to piezoelectric lamina poling direction} \\ -1 & \text{field antiparallel to piezoelectric lamina poling direction} \\ 0 & \text{else} \end{cases} \tag{3.5}$$

Thus, this model can be applied to any combination of piezoelectric and passive plates. Note that for the case of an anisotropic composite material, the stresses and strains are along the fiber direction, as is defined in Figure 3.3. More generally, the in-plane strains

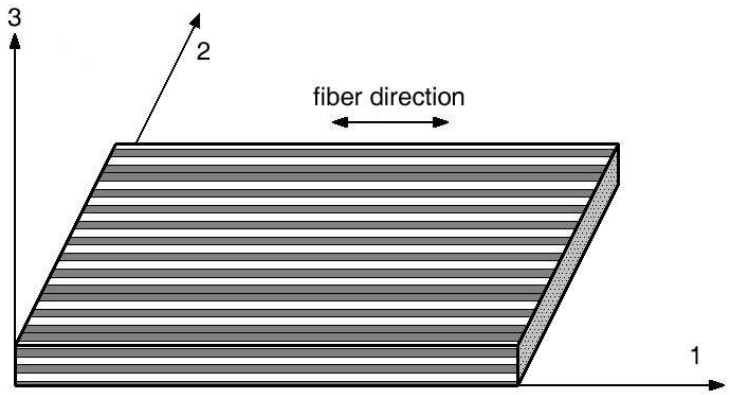

Figure 3.3: Lamina axes diagram.

are given in the following form:

$$\begin{bmatrix} \epsilon_1 \\ \epsilon_2 \\ \gamma_{12} \end{bmatrix}_n = \begin{bmatrix} S_{11} & S_{12} & 0 \\ S_{12} & S_{22} & 0 \\ 0 & 0 & S_{66} \end{bmatrix}_n \begin{bmatrix} \sigma_1 \\ \sigma_2 \\ \tau_{12} \end{bmatrix}_n + \begin{bmatrix} d_{31} \\ d_{32} \\ 0 \end{bmatrix}_n E_3^n + \begin{bmatrix} \alpha_1 \\ \alpha_2 \\ 0 \end{bmatrix}_n \Delta T \tag{3.6}$$

The $[S_{ij}]_n$ terms are the compliances of the n^{th} layer. Using the assumption that the piezoelectric layer is transversely isotropic ($d_{31} = d_{32}$), d_{36} is taken to be 0, thus there are no shearing forces or twisting moments applied by the piezoelectric [50]. Solving (3.6) for the stresses in the piezo layer gives the following:

$$\begin{bmatrix} \sigma_1 \\ \sigma_2 \\ \tau_{12} \end{bmatrix}_n = \begin{bmatrix} Q_{11} & Q_{12} & 0 \\ Q_{12} & Q_{22} & 0 \\ 0 & 0 & Q_{66} \end{bmatrix}_n \left(\begin{bmatrix} \epsilon_1 \\ \epsilon_2 \\ \gamma_{12} \end{bmatrix}_n - \begin{bmatrix} d_{31} \\ d_{32} \\ 0 \end{bmatrix}_n E_3^n - \begin{bmatrix} \alpha_1 \\ \alpha_2 \\ 0 \end{bmatrix}_n \Delta T \right)$$

In equations (3.6) and (3.7), the $[Q_{ij}]_n$ terms are the plane strain modified material constants of the lamina as given in Tables 3.3 and 4.3. To generalize this to arbitrary lamina

orientations, the following notation is used:

$$\begin{bmatrix} \sigma_x \\ \sigma_y \\ \tau_{xy} \end{bmatrix}_n = \begin{bmatrix} \overline{Q_{11}} & \overline{Q_{12}} & \overline{Q_{16}} \\ \overline{Q_{12}} & \overline{Q_{22}} & \overline{Q_{26}} \\ \overline{Q_{16}} & \overline{Q_{26}} & \overline{Q_{66}} \end{bmatrix}_n \left(\begin{bmatrix} \epsilon_x \\ \epsilon_y \\ \gamma_{xy} \end{bmatrix}_n - \begin{bmatrix} d_{31} \\ d_{32} \\ 0 \end{bmatrix}_n E_3^n - \begin{bmatrix} \overline{\alpha_x} \\ \overline{\alpha_y} \\ \overline{\alpha_{xy}} \end{bmatrix}_n \Delta T \right)$$

Where the new $[\overline{Q_{ij}}]_n$ is the adjusted stiffness matrix whose elements have the following properties:

$$\left[\overline{Q_{ij}}\right] = [T]^{-1} [Q_{ij}] [T]^{-T} \tag{3.7}$$

and the transformed CTE terms $[\overline{\alpha_i}]$ are as follows:

$$[\overline{\alpha}] = [T]^{-1} [\alpha] \tag{3.8}$$

where the matrix $[T]$ is defined as follows:

$$[T] = \begin{bmatrix} m^2 & n^2 & 2mn \\ n^2 & m^2 & -2mn \\ -mn & mn & m^2 - n^2 \end{bmatrix} \tag{3.9}$$

In (3.9), the terms m and n are $\cos(\theta)$ and $\sin(\theta)$ respectively where θ is the angle between the global axes and the lamina fiber direction (see Figure 3.4). Now the forces and moments (per unit width) are given as a function of the ply stresses:

$$\begin{aligned} \left[N_i\right] &= \int_0^t [\sigma_i]\, dz \\ \left[M_i\right] &= \int_0^h [\sigma_i] z\, dz \end{aligned} \tag{3.10}$$

In (3.10), the term t is the total actuator thickness, thus to solve for N_i and M_i the integrals need to be split into a summation over all layers of the actuator.

$$\begin{aligned} \left[N_i\right] &= \sum_n \int_{z_{n-1}}^{z_n} [\sigma_i]_n\, dz \\ \left[M_i\right] &= \sum_n \int_{z_{n-1}}^{z_n} [\sigma_i]_n z\, dz \end{aligned} \tag{3.11}$$

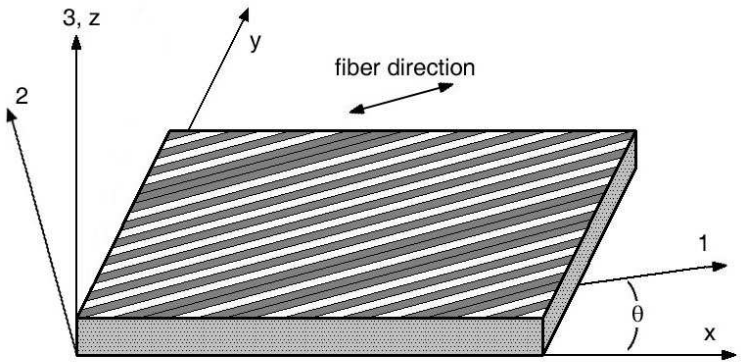

Figure 3.4: Lamina axes diagram with fiber direction not parallel to the global axes.

Next, the actuator properties are determined as a function of the ply layup using laminate plate theory. First, the relationship between the midplane strains and curvatures and the forces and moments is given by:

$$\begin{bmatrix} N \\ M \end{bmatrix} = \begin{bmatrix} A_{ij} & B_{ij} \\ B_{ij} & D_{ij} \end{bmatrix} \begin{bmatrix} \epsilon^0 \\ \kappa \end{bmatrix} \tag{3.12}$$

In equation (3.12) the A, B, and D terms are given as follows:

$$\begin{aligned} A_{ij} &= \textstyle\sum_n \left[\overline{Q_{ij}}\right]_n (z_n - z_{n-1}) \\ B_{ij} &= \tfrac{1}{2} \textstyle\sum_n \left[\overline{Q_{ij}}\right]_n (z_n^2 - z_{n-1}^2) \\ D_{ij} &= \tfrac{1}{3} \textstyle\sum_n \left[\overline{Q_{ij}}\right]_n (z_n^3 - z_{n-1}^3) \end{aligned} \tag{3.13}$$

In equation (3.13), the term z_n is the directed height of the n^{th} lamina with respect to the mid plane as is shown in Figure 3.2. In equation (3.12), the total forces and moments per unit width $[N\ M]^T$ can be split up into three terms: the externally applied moments and the internal forces and moments from the piezoelectric effect and thermal expansion all per

unit width.

$$\begin{bmatrix} N \\ M \end{bmatrix} = \begin{bmatrix} N_{ext} \\ M_{ext} \end{bmatrix} + \begin{bmatrix} N^p \\ M^p \end{bmatrix} + \begin{bmatrix} N^t \\ M^t \end{bmatrix} \tag{3.14}$$

The piezoelectric forces and moments are defined as follows:

$$\begin{aligned} \left[N_i\left(E_3\right)\right]^p &= \textstyle\sum_n \int_{z_{n-1}}^{z_n} [\overline{Q_{ij}}]_n d_{3j} E_3 \cdot p \; dz \\ \left[M_i\left(E_3\right)\right]^p &= \textstyle\sum_n \int_{z_{n-1}}^{z_n} [\overline{Q_{ij}}]_n d_{3j} E_3 z \cdot p \; dz \end{aligned} \tag{3.15}$$

Similarly, the thermal expansion forces and moments are:

$$\begin{aligned} \left[N_i\right]^t &= \textstyle\sum_n \int_{z_{n-1}}^{z_n} \left[\overline{Q_{ij}}\right]_n \left[\overline{\alpha_j}\right]_n \Delta T \; dz \\ \left[M_i\right]^t &= \textstyle\sum_n \int_{z_{n-1}}^{z_n} \left[\overline{Q_{ij}}\right]_n \left[\overline{\alpha_j}\right]_n \Delta T z \; dz \end{aligned} \tag{3.16}$$

Solving equation (3.12) for the midplane strains and curvatures yields the following:

$$\begin{bmatrix} \epsilon^0 \\ \kappa \end{bmatrix} = \begin{bmatrix} A_{ij} & B_{ij} \\ B_{ij} & D_{ij} \end{bmatrix}^{-1} \left(\begin{bmatrix} N_{ext} \\ M_{ext} \end{bmatrix} + \begin{bmatrix} N^p \\ M^p \end{bmatrix} + \begin{bmatrix} N^t \\ M^t \end{bmatrix} \right) \tag{3.17}$$

Finally, the free displacement and blocked force of the actuator are found as a function of the applied fields ($[E_3]_n$) and the external loading. Since axial strains do not contribute to lateral displacement of the distal end of the cantilever, the only quantity of interest from equation (3.17) is κ_x . First note that the curvature κ_x is related to the displacement as $\frac{d^2\delta(x)}{dx^2} = \kappa_x$ where $\delta\left(x\right)$ is the displacement of the actuator at any point along the x axis and define:

$$C = \begin{bmatrix} A_{ij} & B_{ij} \\ B_{ij} & D_{ij} \end{bmatrix}^{-1} \tag{3.18}$$

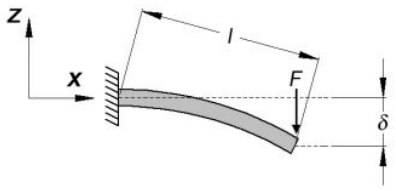

Figure 3.5: Actuator diagram with respect to external parameters.

Now include the external forces and moments into equation (3.17). Note that for a clamped-free cantilever with no external axial forces and an external moment about the y axis,

$$\begin{bmatrix} \epsilon_x^0 \\ \epsilon_y^0 \\ \epsilon_{xy}^0 \\ \kappa_x \\ \kappa_y \\ \kappa_{xy} \end{bmatrix} = [C_{ij}] \left(\begin{bmatrix} 0 \\ 0 \\ 0 \\ M_x(x) \\ 0 \\ 0 \end{bmatrix} + \begin{bmatrix} N_x^p \\ N_y^p \\ 0 \\ M_x^p \\ M_y^p \\ 0 \end{bmatrix} \right) \tag{3.19}$$

For convenience, define the following:

$$P(E_3) = C_{41} N_x^p(E_3) + C_{42} N_y^p(E_3) + C_{44} M_x^p(E_3) + C_{45} M_y^p(E_3) \tag{3.20}$$

Thus it can be seen that the curvature is related to the internal and external moments as follows (ignoring the static thermal forces and moments):

$$\frac{d^2\delta(x)}{dx^2} = P(E_3) + C_{44} M_x(x) \tag{3.21}$$

A functional diagram of the actuator with respect to the external parameters in equation (3.21) is shown in Figure 3.5. For the case of an actuator loaded transversely at the distal end with a point load, the moment per unit width term $M_x(x)$ is defined by cantilever

equations to be $-F\left(l-x\right)/w$. The differential equation in (3.21) is easily solved by noting the strict boundary conditions.

$$\begin{aligned} \left.\frac{d\delta(x)}{dx}\right|_{x=0} &= 0 \\ \delta\left(x\right)|_{x=0} &= 0 \end{aligned} \tag{3.22}$$

Solving (3.21) gives the displacement at any point along a bending cantilever due to an internal moment or external point load.

$$\delta = \frac{P\left(E_3\right)l^2}{2} - \frac{C_{44}F}{w}\left(\frac{lx^2}{2} - \frac{x^3}{6}\right) \tag{3.23}$$

In the above equation, l is the actuator length. The tip displacement is then given by the following:

$$\delta = \frac{P\left(E_3\right)l^2}{2} - \frac{C_{44}Fl^3}{3w} \tag{3.24}$$

The free displacement of the actuator, i.e. the displacement with no external loading is given in equation (3.25).

$$\delta = \frac{P\left(E_3\right)l^2}{2} \tag{3.25}$$

The term w in equation (3.24) represents the actuator width (assuming that the width is constant along the length). Note that in solving for δ, the displacement is independent of the width: actuator geometry will be discussed in section 3.3. Now all that remains is to find the blocked force of the actuator. The blocked force is defined as the force required to bring the actuator back to its neutral position for a given applied field. This is done by setting $\delta = 0$ in equation (3.24) and solving for the external force.

$$F_b = \frac{3P\left(E_3\right)w}{2C_{44}l} \tag{3.26}$$

Note that this form is very similar to that in [78]. Noting that C_{44} is equivalent to w/EI where EI is the beam's effective modulus and P is the equivalent of M/EI, equation

(3.24) can be placed in the traditional form for a clamped-free cantilever beam with an applied force and moment.

$$\delta = \frac{Ml^2}{2EI} - \frac{Fl^3}{3EI} \tag{3.27}$$

3.1.4 Piezoelectric Material Choice

One of the best criterion for choice of piezoelectric material is the strain energy density. The strain energy density is defined as follows:

$$e_{max} = \frac{1}{\rho}\left(\frac{1}{2}E\epsilon_{max}^2\right) \tag{3.28}$$

where e_{max} is the maximum strain energy density, ρ is the density, E is the Young's modulus, and ϵ_{max} is the maximum strain. This last term, ϵ_{max}, can be thought of as derived from one of two different elastic modes: either the strain developed from external loading, or the induced piezoelectric strain at a given field, namely $d_{ij}E_i$. Two piezoelectric materials are considered: PZT-5H, a soft polycrystalline ceramic, and PZN-PT, a ferroelectric relaxor-based single crystal [64, 107]. The former has the benefits of low cost, ease of availability, and relatively high elastic modulus while the latter has a much larger piezoelectric coupling coefficient with the drawbacks of cost, availability, and poor fracture properties. The properties of both materials are given in Table 3.3. To determine which strain to use in (3.28), choose $\min(d_{31}E_3, \epsilon_f)$, where ϵ_f is the mechanical fracture strain. Thus, because of the extremely low fracture toughness associated with single crystal materials, PZT shows a factor of two better performance. Therefore, polycrystalline piezoelectric materials are used throughout the following discussion.

Table 3.3: Piezoelectric material properties (taken from [64], [76], corporate data, and experimental data)

Parameter	Description	PZT-5H	PZN-PT	Units
E	Young's modulus	62	15	GPa
ν_{12}	Poisson's ratio	0.31	0.26	—
G_{12}	Shear modulus	24	6	GPa
d_{33}	Piezoelectric coefficient	650	2000	pCN^{-1}
d_{31}	Piezoelectric coefficient	-320	-970	pCN^{-1}
$E_{3,max}$	Maximum field	2.5	12	$V\mu m^{-1}$
$\epsilon_{1,max(p)}$	Max. piezo. strain	0.3	1.5	%
$\epsilon_{1,max(m)}$	Max. mech. strain	0.3	0.3	%
ρ	Density	7800	8300	$kg \cdot m^{-3}$
α	CTE	3	4	$(\mu m \cdot m^{-1})^{\circ}C^{-1}$
D_U	Energy Density [1]	4	2	Jkg^{-1}

[1] Bulk free energy density for d_{33} excitation.

3.2 Piezoceramic Fracture Mechanics

During actuation, the piezoelectric layer can be placed under high tensile stresses, often close to the ultimate stress. Thus any defects or stress concentrations will cause such actuators to fail under normal operation. These defects lower the fracture toughness of the brittle piezoelectric layer, which also significantly lowers the fatigue life of the actuator and thus the MFI. Increasing the fracture toughness of ceramics, and brittle materials in general, is limited to extrinsic means due to strict material constraints. Understandably, ceramics are seldom used as structural materials because of low fracture toughnesses as compared to metals.

Both amorphous ceramic and single crystal piezoelectric materials are extremely brittle. Brittle materials are characterized by exhibiting little to no plastic deformations which implies the yield stress is effectively equal to the ultimate stress and the stress-strain curves are linear to fracture. Most machining processes cause cracks of various sizes to

form in the given material; the quality of the machining can be thought of as how small or sparse these initial cracks are. The behavior of the cracked sample when under an applied load is a material property. Fracture mechanics, regardless of the material, states that unstable crack growth will occur when the work required to extend the crack (the surface energy of the newly extended crack faces and the energy lost in plastic deformation in the area surrounding the crack tip) is less than the elastic strain energy that is released by the potential crack growth. This is true when the region of plastic deformation is a small region near the crack tip. For ceramics, and brittle materials in general this is simplified by the effective lack of plastic domains anywhere in the sample and thus crack tip growth of any kind is usually unstable. Surrounding any crack in a sample that is subject to a nominal

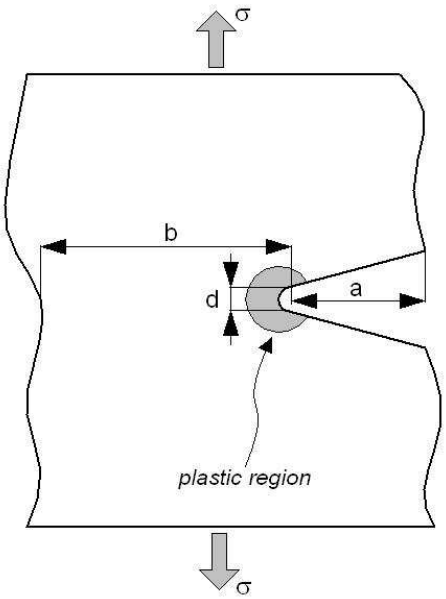

Figure 3.6: Diagram of cracked sample with applied load.

stress is a region of increased local stresses characterized by a stress intensity. The stress

intensity, termed K_i, is a function of the nominal stress σ and the crack size a as defined in the following:

$$K_i = Q\sigma\sqrt{\pi a} \tag{3.29}$$

where Q is a geometry dependent quantity. The subscript i in equation (3.29) is either I, II, or III depending upon the fracture mode present. The fracture mode describes the orientation of the applied stress to the crack growth direction. For the case of the MFI actuators, as well as being the most prominent fracture mode in general is Mode I fracture where the stresses act perpendicular to the crack faces as shown in Figure 3.6. This is under the assumption that the cracks originate on the edges or surface of the piezoelectric material as is observed in this case. Fracture occurs when K_I reaches a critical value K_{IC} which is called the *fracture toughness*. For some materials it is possible to increase the fracture toughness through slight physical modifications (material composition or grain sizes for example). This intrinsic fracture toughness increase is not feasible with crystalline materials since they are defined by the nature of their grain (crystal) structures. However, even though K_{IC} is a fixed material constant, through the use of certain tricks it is possible to extrinsically increase the effective fracture toughness of brittle materials. This is done through crack tip closing mechanisms and local stress biases. Once this optimal fracture toughness is achieved, the only ways to avoid fracture are to lower the operating stresses or lower the initial crack sizes. One goal of this section is to describe several methods for extrinsically increasing the fracture toughness of piezoelectric materials while reducing the initial crack sizes and the effective operating stresses.

3.2.1 Surface Roughness Improvements

The surface roughness is what will be called the initial crack size. There are currently two methods of cutting the piezoelectric materials, the first using a diamond saw and the second using a laser cutting stage. Both methods have benefits and drawbacks, and both methods create different surface roughnesses. Example surfaces for these two methods are shown in Figure 3.7.

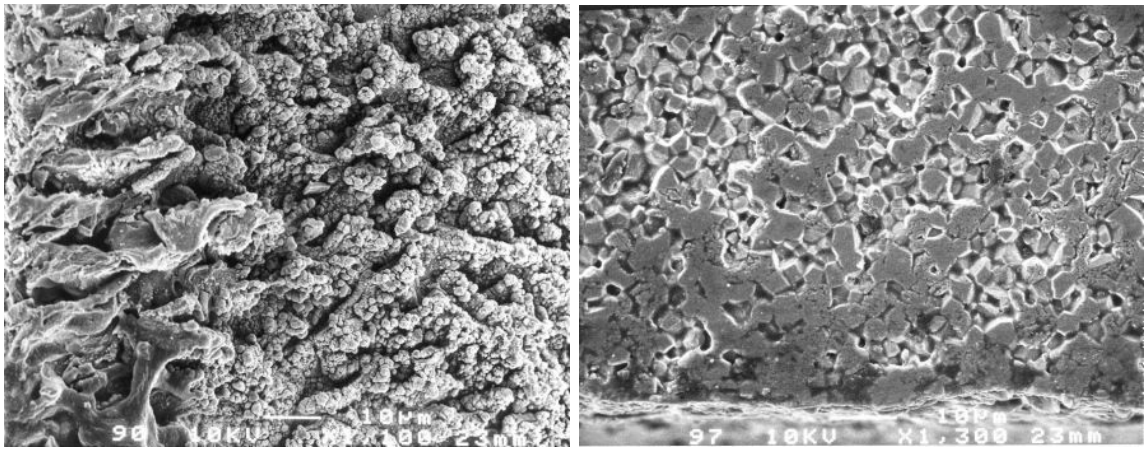

Figure 3.7: SEM scan of (a) laser cut (b) saw cut PZT edges.

The question of surface roughness improvements is linked to the grain size. One question that arises is the feasibility of decreasing the initial cracks to sub-grain sizes. An example cross section of an untreated PZT surface is shown in Figure 3.8.

Polishing such a grain structure to surface roughnesses less than the grain size will result in a layer of incomplete grains on the polished surface as is shown in Figure 3.9. This may cause one of two things. The remaining incomplete grains can be weaker due to the material's affinity for transgranular fracture. Or the material can exhibit intergran-

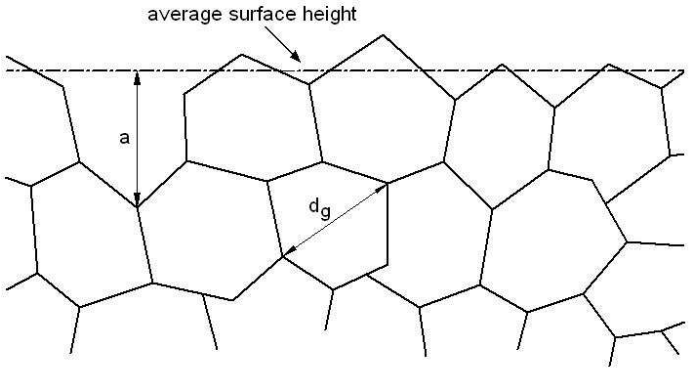

Figure 3.8: Grain structure of an unprocessed PZT edge.

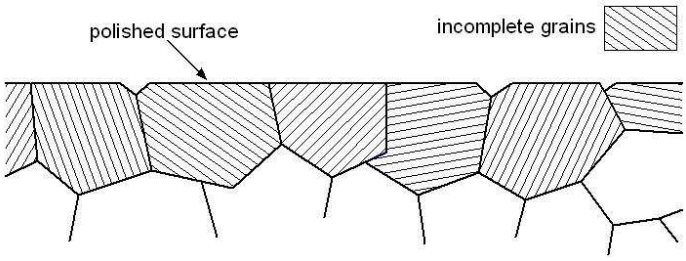

Figure 3.9: Grain structure of a polished PZT edge.

ular fracture, meaning that cracks will propagate via the grain boundaries. To test this, an unprocessed sample of PZT was cleaved and the newly created surface was observed in an SEM. The resulting image in Figure 3.10 clearly shows that the PZT demonstrates intergranular fracture, thus any removal of surface defects will result in decreased initial crack sizes. Laser micromachining allows the material to be cut into arbitrary shapes, as

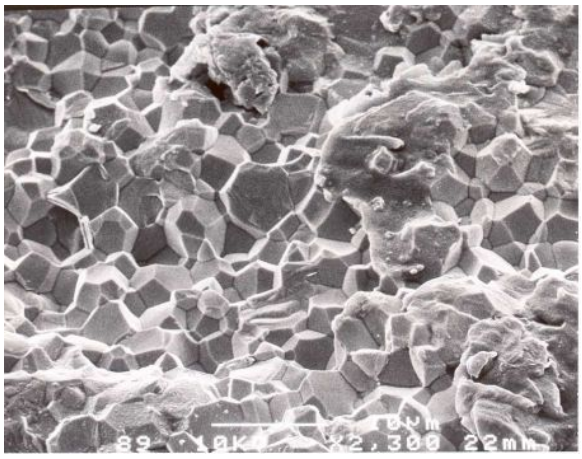

Figure 3.10: Cleaved PZT surface.

opposed to saw cutting which only allows for convex shapes with straight edges, and more practically, trapezoidal shapes are difficult to control. One concern with laser micromachining is the effect this process has on the surface features. It is easily observed that a laser cut sample no longer exhibits a crystalline structure on the cut surface (see Figures 3.7(a) and 3.11). There are two possibilities for the content of this new surface. During laser cutting, the surface is heated and vaporized instantly, thus if any of the constituent elements of the piezoelectric material have a relatively high vapor pressure, preferential out gassing can occur. This could potentially leave films or oxides on the surface which would

affect (either beneficially or adversely) the fracture mechanics of the sample as a whole. The other possibility is that the PZT is melted and then cools back to a crystalline state. Since this is a rapid, uncontrolled cooling, and since the grain size of amorphous crystal materials is determined by the rate of cooling, it is possible that the new surface is PZT with much reduced grain sizes. Figure 3.12 shows the effects of polishing this layer down to the unaffected PZT.

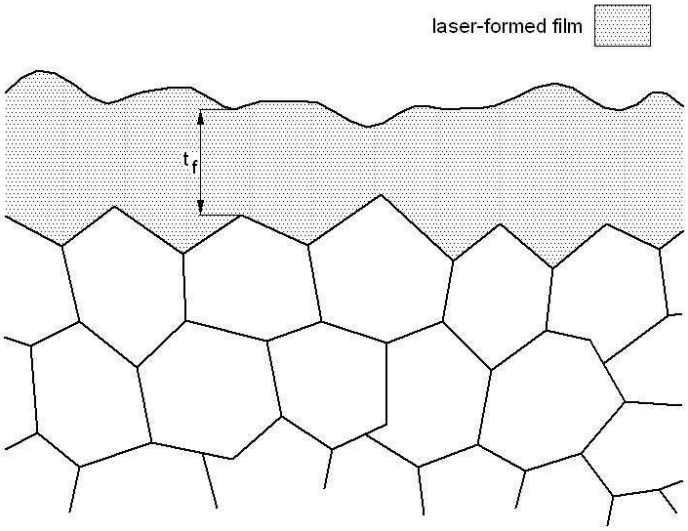

Figure 3.11: Cross section of a laser-micromachined PZT edge.

To determine which mechanism is at work, another SEM was performed to look for small grain structure. A sample that was lasercut was cleaned by flushing with isopropyl alcohol, then scanned. The results are shown in Figure 3.13. Thus, since no grain structure can be seen down to approximately the $10nm$ scale (approximately three orders of magnitude smaller than the undisturbed PZT grains), the surface film is assumed to be an oxide of a constituent material. This film surface was subsequently polished with decreasing grit

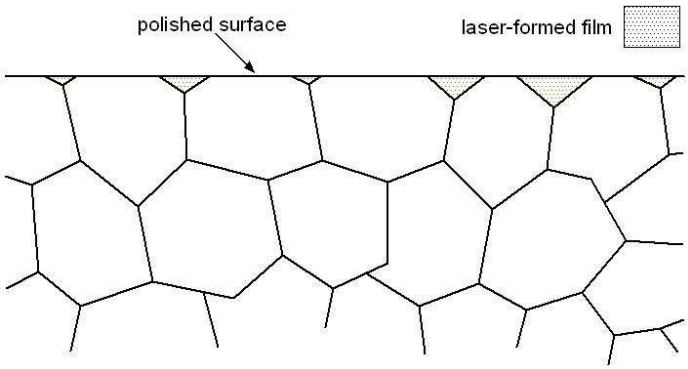

Figure 3.12: Polished laser-micromachined PZT edge.

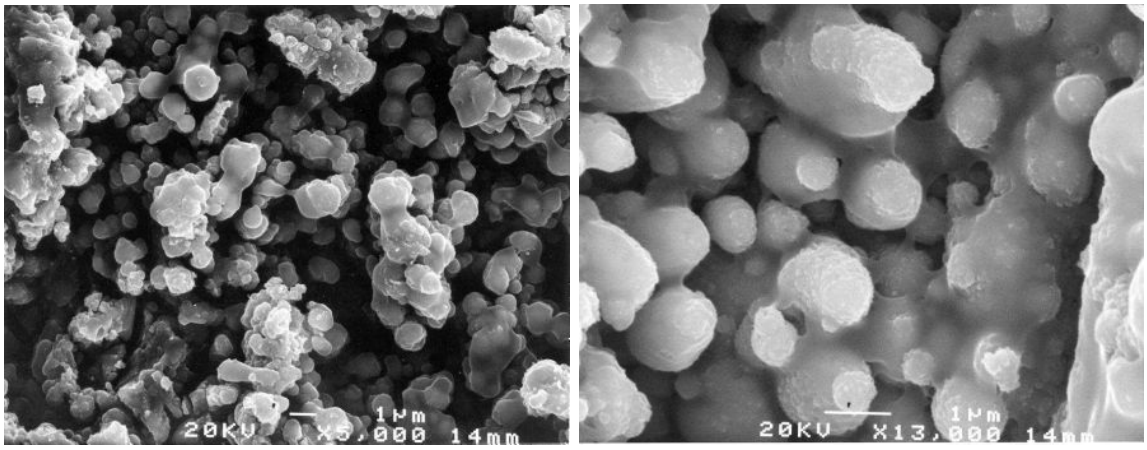

Figure 3.13: Laser cut surface zoomed in to search for grain structures.

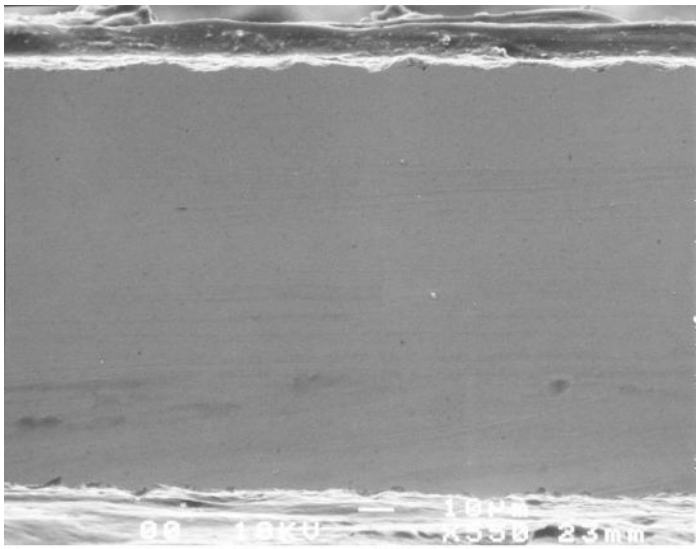

Figure 3.14: Final polished laser cut PZT surface.

size lapping films and scanned again to determine the initial crack size and to check for embedding of any of the polishing materials. An example of the polished surface is shown in Figure 3.14. In conclusion, regardless of the surface makeup, polishing helps reduce surface roughness and initial crack sizes because of intergranular fracture. Subsequent to laser micromachining and polishing, the cracks were reduced from approximately $5\mu m$ to $100nm$.

3.2.2 Crack Closing Techniques

After the surface is polished to reduce initial cracks, one common extrinsic method to increase the fracture toughness is implemented along the edges of the piezoelectric material. To limit the crack growth, a crack closing technique is typically used. Such a technique acts to stop, slow, or reverse the growth of a crack tip. Traditional embodiments of such

a technique involve the use of fibers embedded into the material oriented along the axis of maximum applied stress. In the case of the MFI actuators, all of the cracks are assumed to originate along the edge of the piezoceramic, where the cutting and subsequent processing takes place. Thus the piezoceramic material used does not need embedded fibers, but would benefit from a layer of constricting material applied to the edges of the actuator.

One method of external crack closing involves coating the edges with a layer in tension which will in turn place the edges in compression. In the presence of surface cracks, such a layer will act to negate the stress concentrations associated with the surface defects (which were unremovable via laser cutting and polishing). Figure 3.15 shows a cracked surface with a layer of compressive film.

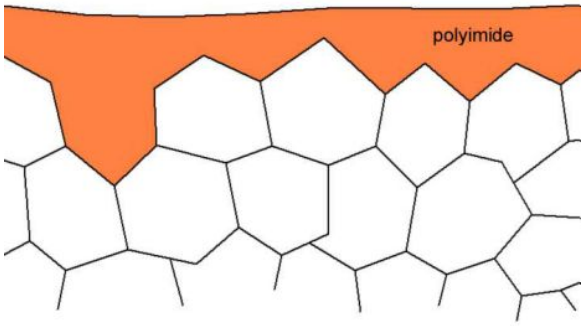

Figure 3.15: Cracked PZT surface with polyimide coating.

The stress intensity fields associated with an edges crack are defined by the stress concentration factor (K_t) which is the ratio of the maximum stress experienced at the crack tip to the nominal applied stress. For the case of the sample shown in Figure 3.6, which is a single notched specimen under tensile loading, the stress concentration factor $K_t = 3.0$. This puts the PZT close to its ultimate stress (locally) during normal operation (the total

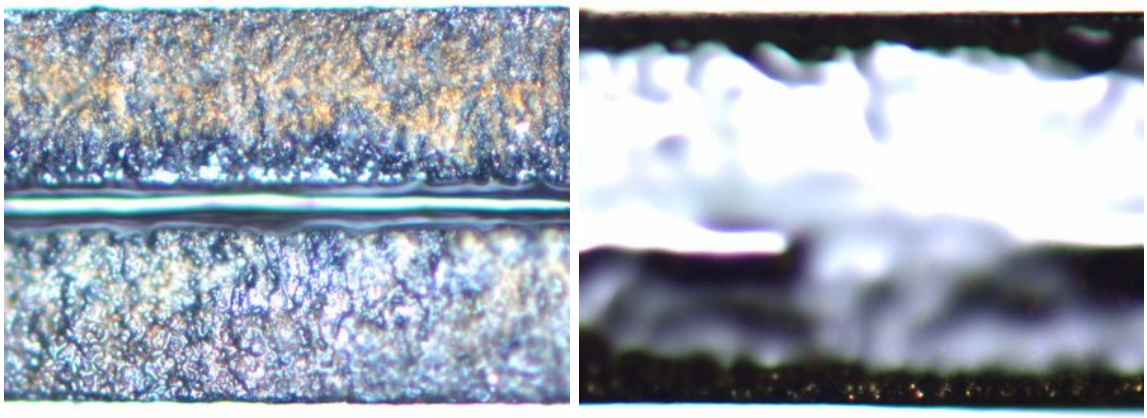

Figure 3.16: Optical microscope images of $250\mu m$ thick bare (a) and polyimide coated (b) actuator edges.

stresses and strains experienced by the actuator under normal operating conditions will be discussed in section 3.6).

To create such a layer, a high CTE polymer is used. One such candidate is a polyimide (PI-2525 from HD Microsystems), which has the following properties: $325°C$ cure temperature, $\alpha = 50\mu m/m°C$ CTE, and an elastic modulus of $2.5GPa$. This yields a residual compressive stress of $40MPa$ which is approximately a third of the ultimate stress of the PZT and therefore a significant contribution in negating the local stress intensity fields. Figure 3.16 shows actuator edges both coated and uncoated with a polyimide crack-closing layer. An ancillary benefit to coating the edges of the actuator is in the dielectric properties of the polymer as an insulating layer. The high fields associated with such electroactive materials necessitates precautionary measures to assure that no shorting occurs.

3.2.3 Thermal Stress Biasing

A common technique involved in the use of concrete for structures is prestressing. Concrete is a material which has a high strength in compression, but yields easily in tension. To bring this into a usable range, the concrete is given a compressive prestress which effectively increases the usable stress range of the material into greater a tensile region. This section describes a methods of adding a stress bias to the piezoelectric layer by exploiting the coefficient of thermal expansion (CTE) mismatches between constituent layers.

Every free solid material exhibits a strain when subjected to a change in temperature. Changing the temperature of a beam consisting of two materials which have the same CTE will cause the beam to elongate or contract depending upon the sign of the CTE and the change in temperature. In this case, no stress will develop within the beam. However, when there is a CTE mismatch, then one material will want to expand or contract more than the other, thus causing stress gradients through the thickness of the beam. This is the case in curing the actuators. Before curing, the materials in the actuator are free and when brought up to high temperatures for curing, they freely expand or contract depending upon the sign of their CTE. This state, before any significant cross linking of the matrix resin occurs, is referred to as the stress free state. Once bonding occurs, the materials are joined at the interface. By designing the elastic layer to have a proper CTE with respect to the piezoelectric layer (by keeping the CTE of the elastic layer greater than that of the piezoelectric layer), a compressive stress is applied to the piezoelectric material after the actuator is subsequently brought down to room temperature. Quantitatively, the thermal stresses develop in each layer of the laminate can be determined by examining the thermal

term in (3.17). Noting that the strain in the i^{th} given layer is then given by:

$$\epsilon_i = \epsilon^0 + \kappa z_i \tag{3.30}$$

yields the strain in each layer for internal (thermal and piezoelectric) and external loading. Section 3.6 shows a figure of the strains in the various layers of the actuators. An ancillary benefit to the laminate plate theory model of the actuator motion is the ease of strain and stress analysis which is inherent in this. Setting the piezoelectric and external terms in equation (3.17) to zero, solving for the strains, then using equation (3.30) gives the strain and each layer. Since the piezoelectric layer is assumed to be isotropic, this is sufficient to determine the stress in each direction. For anisotropic materials in arbitrary orientations, it is necessary to apply a transformation to get the strains in the global frame to the strains in the fiber frame. To transform the strains in the global axis to the individual lamina axis for a lamina with orientation θ, a simple transformation is given by the following:

$$\begin{bmatrix} \epsilon_1 \\ \epsilon_2 \\ \gamma_{12} \end{bmatrix} = T(\theta) \begin{bmatrix} \epsilon_x \\ \epsilon_y \\ \gamma_{xy} \end{bmatrix} \tag{3.31}$$

It is important to note here that caution must be used in designing the stress biases to be applied to the piezoelectric layer. While compressive stresses will effectively increase the usable stress range, it is well documented that applying compression to piezoelectric materials significantly decreases the piezoelectric coupling coefficients [1, 104, 56, 86, 112]. The inverse is also true (though the relation is nonlinear): tensile stress decreases the effective working range and increases the piezoelectric coupling coefficients.

3.3 Geometric Improvements

This section describes two methods of distributing the strain in the piezoceramic layer uniformly along the length. By achieving this, stress concentrations can be avoided and each infinitesimal piezoelectric element can be driven close to the fracture strain (as opposed to only those at the proximal end as is the case with traditional rectangular clamped-free cantilever actuators). The first (intrinsic) method involves altering the planar geometry of the piezoelectric lamina and the actuator as a whole. The second (extrinsic) method adds a rigid link to the output of the actuator to act as a lever mechanism.

3.3.1 Intrinsic Geometry

Under conditions in which there is no load applied to the distal end of the actuator, the electric field produces a strain in the piezoelectric layer which forms a uniform bending moment along the length of the actuator. Although the length of the piezoelectric material changes, producing a net strain, on a local scale the piezoelectric effect does not produce a significant strain. The reason for this is that as the domains change size, the lattice parameters increase, however adjacent domains apply minimal tensile force on each other. For the case of external loading, however, significant tensile stresses will be developed. For the case of a clamped-free cantilever, the moment per unit width generated in the beam is $M_x(x) = -F(l-x)/w$. For a constant cross section, this moment is proportional to the stress at a given point, thus the stresses will be maximum at the proximal end of the actuator. If the cross section varies along x, the stress profile can be controlled and large stresses can be eliminated. Varying the thickness of the piezoelectric material is

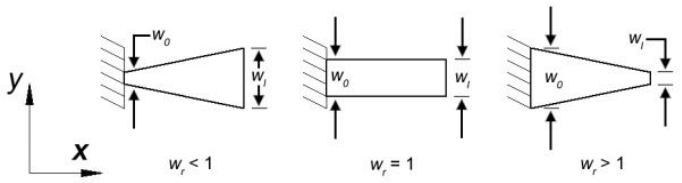

Figure 3.17: Three representative width profiles

not practical given the thickness of the commercially available PZT plates used ($127\mu m$); however, controlling the width is relatively simple. To explore this further, consider equation (3.21) and expand the external moment.

$$\frac{d^2\delta(x)}{dx^2} = P(E_3) - \frac{C_{44}F(l-x)}{w(x)} \tag{3.32}$$

Note that in section 3.1.3, the width was considered constant, i.e. $w(x) = w$. Now assume that the width varies as a function of x and again work through the differential equation.

$$\delta(x) = \frac{P(E_3)x^2}{2} - C_{44}F\int\int\frac{l-x}{w(x)}dxdx \tag{3.33}$$

Thus the free deflection (with $F == 0$) does not vary with a change in the width profile. Next it is necessary to determine $w(x)$ explicitly for each profile for use in equation (3.33). For the case of a trapezoidal profile, this is given by the following:

$$w(x) = \frac{2(w_{nom} - w_0)}{l}x + w_0 \tag{3.34}$$

Example width profiles are shown in Figure 3.17. For the above equation, w_{nom} is the nominal width (the width at $x = l/2$) which is the same for all trapezoidal width profiles (to keep the planform area and thus the mass constant for collateral comparisons). In this figure, w_0 and w_l are the width at the proximal and distal ends respectively. For

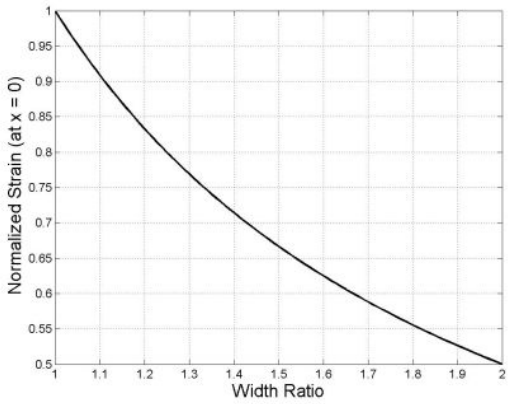

Figure 3.18: Normalized strain at the proximal end of the actuator for a varying width ratio.

comparison, the area for each of the profiles is kept constant. Thus for a rectangular area where $w_0 = w_l = w_{nom}$:

$$w_{nom} l = \frac{1}{2} (w_0 + w_l) l \tag{3.35}$$

For a constant area, substituting in $x = l$ into the above equation to yield $w_l = 2w_{nom} - w_0$. Next define the width ratio, $w_r = w_0/w_{nom}$ and rearrange the terms in equation (3.34) to yield:

$$w(x) = w_{nom} \left(\frac{2(1 - w_r)}{l} x + w_r \right) \tag{3.36}$$

It is simple to see that for a thin long clamped-free beam point loaded at the distal end, the strain at the proximal end is inversely proportional to the width ratio. This is shown in Figure 3.18. To illustrate this point more concisely, the normalized strain profile along the length of the actuator is plotted for a few width ratios in Figure 3.19. The strain is normalized to the strain at w_{nom}.

It is clear that altering the width can lower peak stresses, thus increasing the load

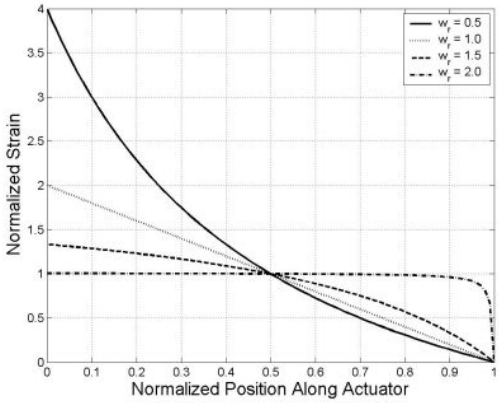

Figure 3.19: Strain profile for various width ratios.

to fracture, now it will be shown that for a fixed actuator area, varying the width can increase or decrease the blocked force. Now to examine the effect of varying width profiles, the normalized blocked force is determined as a function of the width ratio. Again the curvature is given by:

$$\frac{d^2\delta(x)}{dx^2} = P(E_3) - \frac{C_{44}F}{w_{nom}}\left[\frac{l-x}{\frac{2}{l}(1-w_r)x + w_r}\right] \tag{3.37}$$

For convenience, define the following: $a = -1$, $b = l$, $p = 2(1-w_r)/l$, and $q = w_r$. Now the terms in (3.37) can be rearranged in a simpler form and solved for the slope:

$$\frac{d\delta(x)}{dx} = P(E_3)x - \frac{C_{44}F}{w_{nom}}\int \frac{ax+b}{px+q}dx \tag{3.38}$$

This can be simplified, solving for the slope to yield the following:

$$\frac{d\delta(x)}{dx} = P(E_3)x - \frac{C_{44}F}{w_{nom}}\left[\frac{aq + apx + (bp-aq)\ln(px+q)}{p^2} + c_1\right] \tag{3.39}$$

Now note that for the boundary condition, the slope α at $x = 0$ is 0, thus the constant term

c_1 in (3.39) is:

$$c_1 = -\frac{aq + (bp - aq)\ln(q)}{p^2} \tag{3.40}$$

Thus the slope at any point along the length is defined as:

$$\frac{d\delta(x)}{dx} = P(E_3)\,x - \frac{C_{44}F}{w_{nom}}\left[\frac{apx + (bp - aq)\ln\left(\frac{px+q}{q}\right)}{p^2}\right] \tag{3.41}$$

Next the displacement is determined:

$$\delta(x) = \frac{P(E_3)\,x^2}{2} - \frac{C_{44}F}{w_{nom}}\int \frac{apx + (bp - aq)\ln\left(\frac{px+q}{q}\right)}{p^2}dx \tag{3.42}$$

Performing the integration yields:

$$\delta(x) = \frac{P(E_3)\,x^2}{2} - \frac{C_{44}F}{w_{nom}}\left[\frac{ax^2}{p} + \frac{(bp - aq)\,q}{p^3}\left(\left(\frac{px+q}{q}\right)\ln\left(\frac{px+q}{q}\right) - \left(\frac{px+q}{q}\right) + c_2\right)\right] \tag{3.43}$$

Again, considering the boundary condition that the displacement is zero at the proximal end, the constant $c_2 = 1$. Now allowing for width tapering as defined in equation (3.36), the displacement if modified as follows:

$$\delta(x) = \frac{P(E_3)\,x^2}{2} - \frac{C_{44}F}{w_{nom}}\left(\frac{l\left(2g_1x\left(g_2l + g_1x\right) + lg_2\left(lw_r - 2g_1x\right)g_3\right)}{8\left(1 - w_r\right)^3}\right) \tag{3.44}$$

where $g_1 = w_r - 1$, $g_2 = w_r - 2$, and $g_3 = \ln\left(\frac{-2g_1}{lw_r}x + 1\right)$ Choosing $x = l$ and simplifying (3.44) yields the modified displacement for arbitrary trapezoidal widths:

$$\delta(l) = \frac{P(E_3)\,l^2}{2} - \frac{C_{44}Fl^3}{w_{nom}}\left[\frac{(w_r - 2)^2\ln\left(\frac{2-w_r}{w_r}\right) - 2(3w_r - 4)(w_r - 1)}{8\left(1 - w_r\right)^3}\right] \tag{3.45}$$

Now when $\delta(l) = 0$, the blocked force, F_b, is defined as:

$$F_b = \frac{P(E_3)\,w_{nom}}{2C_{44}l}\left[\frac{8\left(1 - w_r\right)^3}{(w_r - 2)^2\ln\left(\frac{2-w_r}{w_r}\right) - 2(3w_r - 4)(w_r - 1)}\right] \tag{3.46}$$

For convenience, define the following as the width factor:

$$W = \frac{1}{3} \cdot \frac{8\left(1 - w_r\right)^3}{\left(w_r - 2\right)^2 \ln\left(\frac{2-w_r}{w_r}\right) - 2\left(3w_r - 4\right)\left(w_r - 1\right)} \tag{3.47}$$

$$F_b = \frac{3P\left(E_3\right) w_{nom}}{2C_{44}l} W \tag{3.48}$$

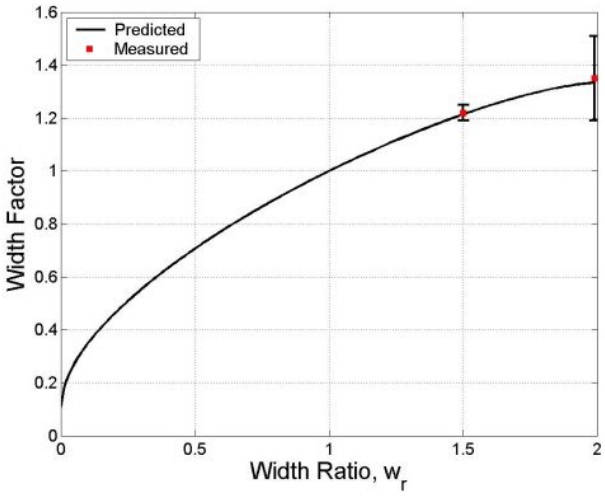

Figure 3.20: Width factor as a function of width ratio.

The width factor is plotted in Figure 3.20, showing the variation with the width ratio. Note that for $w_r = 1$, $W = 1$, yielding the same calculation for blocked force as in equation (3.26) for the rectangular case. From this point, the energy and energy density can be calculated. Substituting the blocked force and free displacement into equation (3.1) will yield the following:

$$U_m = \frac{3P\left(E_3\right)^2 w_{nom} l}{8C_{44}} W \tag{3.49}$$

Note that the term $w_{nom}l$ represents the area of the actuator, and that the energy is linear

with the area. To calculate the energy density, first define the mass as follows:

$$m_a = \sum_n \rho_n t_n w_{nom} l \tag{3.50}$$

Thus the energy density is given as:

$$D_U = \frac{\frac{3P(E_3)^2}{8C_{44}} W}{\sum_n \rho_n t_n} \tag{3.51}$$

Finally, the stiffness of the actuator can be calculated from the blocked force and the free displacement:

$$k_a = \frac{3w_{nom}}{C_{44} l^3} W \tag{3.52}$$

Thus the greatest energy, and energy density, and stiffness are obtained from a width ratio of 2, which represents a triangular actuator. The improvements for each of these quantities is given by the limit of W:

$$\lim_{w_r \to 2} W = \frac{4}{3} \tag{3.53}$$

3.3.2 Extrinsic Geometry

Another method of improving the energy density of a cantilever bending actuator is to add an extension to the distal end. The concept of a rigid extension was introduced by Campolo et al. [11]. This extension acts as a lever which converts the force on the tip to a force and moment at the interface between the piezo and the extension. By transforming the point load to a force and moment as seen by the active material, the strain is more uniformly distributed along the length. Because of this, large differences in stress between different sections are decreased and each infinitesimal section of the piezoelectric material can be driven closer to the fracture strain. Thus the extension does not add mechanical energy

to the system, but instead allows all parts of the actuator to contribute more uniformly to the work. To examine the effects of the extension, first the external moment term ($M_x(x)$)

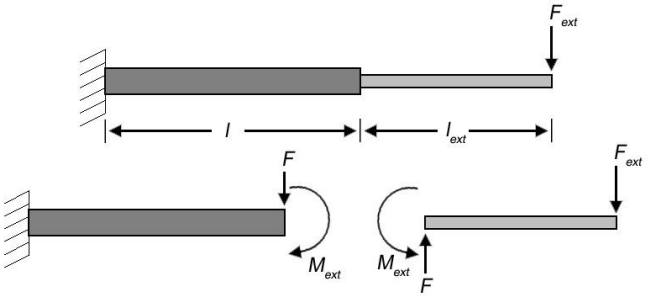

Figure 3.21: Exploded image of actuator with extension.

from equation (3.21) needs to be determined.

$$\begin{bmatrix} F \\ M_{ext} \end{bmatrix} = \begin{bmatrix} 1 \\ -l_{ext} \end{bmatrix} F_{ext} \tag{3.54}$$

Now it is clear that there will be a superposition of a pure moment and a moment generated by the point load. Thus:

$$M_x(x) = -\frac{F_{ext}\left((l + l_{ext}) - x\right)}{w_{nom}} \tag{3.55}$$

Note that in the above equation, the width is set to be constant and equal to w_{nom}. Next, the curvature in equation (3.21) is split into two terms, one from the internal piezoelectric moment ($\frac{d^2\delta_p(x)}{dx^2}$) and one from the externally applied moment ($\frac{d^2\delta_f(x)}{dx^2}$).

$$\frac{d^2\delta_p(x)}{dx^2} = P(E_3) \tag{3.56}$$

$$\frac{d^2\delta_f(x)}{dx^2} = C_{44}M_x(x) \tag{3.57}$$

Solving the above two equations for the slope yields the following:

$$\frac{d\delta_p(x)}{dx} = P(E_3)\,x \tag{3.58}$$

$$\frac{d\delta_f(x)}{dx} = -\frac{C_{44}F_{ext}\left((l+l_{ext})\,x - \frac{x^2}{2}\right)}{w_{nom}} \tag{3.59}$$

Finally, the displacement for both cases is given as follows:

$$\delta_p(x) = \frac{P(E_3)\,x^2}{2} \tag{3.60}$$

$$\delta_f(x) = -\frac{C_{44}F_{ext}\left((l+l_{ext})\,\frac{x^2}{2} - \frac{x^3}{6}\right)}{w_{nom}} \tag{3.61}$$

At $x = l$, the displacement at the interface between the piezo and extension is found using the above two equations.

$$\delta_p(l) = \frac{P(E_3)\,l^2}{2} \tag{3.62}$$

$$\delta_f(l) = -\frac{C_{44}F_{ext}}{w_{nom}}\left(\frac{l^3}{3} + \frac{l_{ext}l^2}{2}\right) \tag{3.63}$$

Next note that the displacement at the distal end of the extension is a function of the displacement at the interface, the slope at the interface and the extension length.

$$\delta(l+l_{ext}) = \delta(l) + \left.\frac{d\delta(x)}{dx}\right|_{x=l} l_{ext} \tag{3.64}$$

For the case of the internally induced displacement, this is given by:

$$\delta_p(l+l_{ext}) = \frac{P(E_3)\,l^2}{2} + P(E_3)\,ll_{ext} \tag{3.65}$$

And for the displacement induced by the external moment:

$$\delta_f(l+l_{ext}) = -\frac{C_{44}F_{ext}}{w_{nom}}\left(\frac{l^3}{3} + l^2l_{ext} + ll_{ext}^2\right) \tag{3.66}$$

Both of these can be simplified by introducing the length ratio, l_r, defined as the ratio of the extension length to the actuator length (without the extension).

$$\delta_p(l+l_{ext}) = \frac{P(E_3)\,l^2}{2}(1+2l_r) \tag{3.67}$$

$$\delta_f\left(l+l_{ext}\right)=-\frac{C_{44}F_{ext}l^3}{3w_{nom}}\left(1+3l_r+3l_r^2\right) \tag{3.68}$$

To solve for the blocked force at the extension, the superposition of the two displacements must be zero, i.e. $\delta_p\left(l+l_{ext}\right)+\delta_p\left(l+l_{ext}\right)=0$. Using this and solving for F_{ext} yields the blocked force as follows:

$$F_{b,ext}=\frac{3P\left(E_3\right)w_{nom}}{2C_{44}l}\frac{\left(1+2l_r\right)}{\left(1+3l_r+3l_r^2\right)} \tag{3.69}$$

Note that this is done without regard to the width profile, and setting the width to w_{nom}. Now the energy for the actuator with the extension is given as the follows by substituting the terms in (3.69) and the free displacement from (3.67) into (3.1):

$$U_{m,ext}=\frac{3P\left(E_3\right)^2lw_{nom}}{8C_{44}}L \tag{3.70}$$

The term L in the above equation is a unit-less function of the extension ratio:

$$L=\frac{\left(1+2l_r\right)^2}{\left(1+3l_r+3l_r^2\right)} \tag{3.71}$$

The stiffness of the actuator with extension is given as follows:

$$k_{ext}=\frac{3w_{nom}}{C_{44}l^3\left(1+3l_r+3l_r^2\right)} \tag{3.72}$$

Finally, assume that the extension adds negligible mass to the actuator, and thus the energy and energy density are proportional to L. The function L is plotted in Figure 3.22 as a function of the extension ratio l_r. The energy and energy density improvements from this extension are clearly proportional to L and are thus a function of l_r. To determine the maximum improvement in energy, note the following:

$$\lim_{l_r\to\infty}L=\frac{4}{3} \tag{3.73}$$

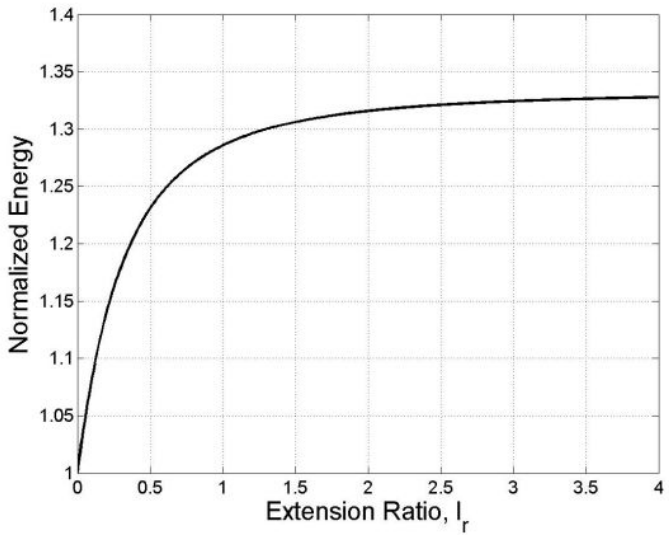

Figure 3.22: Energy improvement as a function of the extension ratio.

Thus the maximum improvement in energy and energy density is 4/3. Note that for all the equations in section 3.3.2 the extension is assumed to be perfectly rigid, or more practically, to have a stiffness $> 10\times$ that of the actuator without the extension.

3.3.3 Complete Model

Combining the results from sections 3.3 and 3.3.2 yields the complete description of the actuator performance. This is done by again performing the integrations on the curvature, but now combining the width and extension terms in the external moment.

$$M_x(x) = -\frac{F_{ext}\left(l\left(1+l_r\right)-x\right)}{w_{nom}\left(\frac{2(1-w_r)}{l}x+w_r\right)} \tag{3.74}$$

The remainder of the procedure is identical to that of section 3.3.2. First, the displacement due to the applied electric field is found, along with the displacement due to an external force. These are then added and set to zero to find the blocked force. Note that the free

displacement is identical to the results in section 3.3.2. Thus the displacement due to an external force is determined first.

$$\frac{d^2\delta_f(x)}{dx^2} = -C_{44}\frac{F_{ext}\left(l\left(1+l_r\right)-x\right)}{w_{nom}\left(\frac{2(1-w_r)}{l}x+w_r\right)} \tag{3.75}$$

Again, using similar notation to section 3.3, this can be rewritten as follows:

$$\frac{d^2\delta_f(x)}{dx^2} = -\frac{C_{44}F_{ext}}{w_{nom}}\left(\frac{ax+b}{px+q}\right) \tag{3.76}$$

where $a=-1$, $b=l\left(1+l_r\right)$, $p=\frac{2(1-w_r)}{l}$, and $q=w_r$. Integrating, minding the strict boundary conditions gives the slope.

$$\frac{d\delta_f(x)}{dx} = -\frac{C_{44}F_{ext}}{w_{nom}}\left(\frac{ax}{p}+\frac{\left(bp-aq\right)ln\left(\frac{q+px}{q}\right)}{p^2}\right) \tag{3.77}$$

Integrating again gives the displacement as a function of the position:

$$\delta_f(x) = -\frac{C_{44}F_{ext}}{w_{nom}}\left(\frac{px\left(-2bp+2aq+apx\right)+2\left(bp-aq\right)\left(q+px\right)\ln\left(\frac{q+px}{q}\right)}{2p^3}\right) \tag{3.78}$$

Substituting in for a, b, p, and q, as well as setting $x=l$ gives the displacement at the tip of the actuator.

$$\delta_f(l) = -\frac{C_{44}F_{ext}l^3}{3w_{nom}}G_1 \tag{3.79}$$

Where G_1 is a function of the width ratio and extension ratio.

$$G_1 = \frac{6\left(w_r-1\right)\left(-3-2l_r+2\left(1+l_r\right)w_r\right)+3\left(w_r-2\right)\left(-2+2l_r\left(w_r-1\right)+w_r\right)\ln\left(\frac{2-w_r}{w_r}\right)}{8\left(1-w_r\right)^3} \tag{3.80}$$

Now again note that for a rigid extension, $\delta\left(l+l_{ext}\right)=\delta\left(l\right)+\frac{d\delta}{dx}\big|_{x=l}\,l_{ext}$. Substituting this into (3.79) yields the following:

$$\delta_f\left(l+l_{ext}\right) = -\frac{C_{44}F_{ext}l^3}{3w_{nom}}G_2 \tag{3.81}$$

where the parameter G_2 is given as follows:

$$G_2 = \frac{-6\left(w_r - 1\right)\left(-3 + 4l_r\left(w_r - 1\right) + 2w_r\right) + 3\left(-2 + 2l_r\left(w_r - 1\right) + w_r\right)^2 \ln\left(\frac{2-w_r}{w_r}\right)}{8\left(1 - w_r\right)^3} \tag{3.82}$$

Now add equation (3.68) to equation (3.81) and set to zero and solve for the blocked force.

$$F_{b,ext} = \frac{3P\left(E_3\right)w_{nom}}{2C_{44}l} G_{Fb} \tag{3.83}$$

Where the term G_{Fb} is called the blocked force geometry constant and is defined as follows:

$$G_{Fb} = \frac{\left(1 + 2l_r\right)}{G_2} \tag{3.84}$$

For convenience, call the term $(1 + 2l_r)$ in (3.68) G_δ, the free displacement geometry constant. Lastly, call G_U the product $G_\delta G_{Fb}$ thus the mechanical energy can be written as a function of G_U:

$$U_m = \frac{3P\left(E_3\right)^2 l w_{nom}}{8C_{44}} G_U \tag{3.85}$$

Thus G_U multiplies with the energy and also the energy density. Therefore G_U is a relative measure of the geometrically improved energy density. This parameter is plotted below as a function of the width and extension ratios.

Finally, the stiffness can be defined in terms of G_δ and G_{Fb}:

$$k = \frac{3w_{nom}}{C_{44}l^3} \frac{G_{Fb}}{G_\delta} \tag{3.86}$$

This completes the model for cantilever piezoelectric bending actuators including any number, anisotropy, or orientation of the constituent layers, number, placement, or makeup of piezoelectric layers, and overall geometry as is shown in Table 3.4.

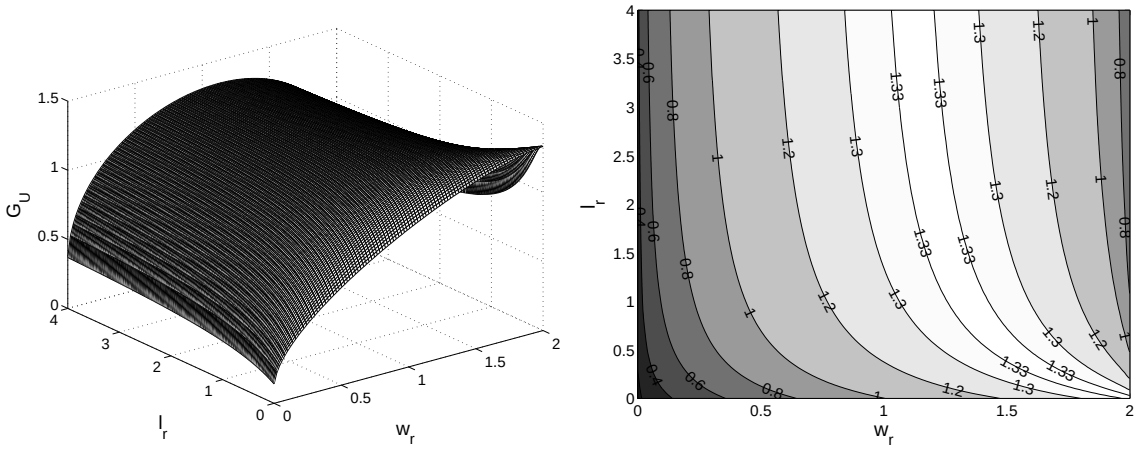

Figure 3.23: Energy improvement as a function of the geometry.

Table 3.4: Complete actuator parameter matrix.

Parameter	Abbreviation	Complete Model	Units
Displacement	δ	$\frac{Pl^2}{2}G_\delta$	m
Blocked Force	F_b	$\frac{3Pw_{nom}}{2C_{44}l}G_{Fb}$	N
Mechanical Energy	U_m	$\frac{3P^2lw_{nom}}{8C_{44}}G_U$	J
Energy Density	D_U	$\frac{\frac{3P^2}{8C_{44}}G_U}{\sum_n \rho_n t_n}$	Jkg^{-1}
Stiffness	k	$\frac{3w_{nom}}{C_{44}l^3}\frac{G_{Fb}}{G_\delta}$	Nm^{-1}

3.4 Fabrication

The actuators use a multistep fabrication process, incorporating all of the techniques described in section 3.2 and using the piezoelectric materials described in section 3.1.4. From the design analysis, UHM unidirectional carbon fiber composites are used for the passive layers. Carbon fiber-based composites have the added benefit of being decent ($\approx 1 \times 10^{-3} \Omega cm$) electrical conductors (for low current applications), thus no additional electrodes need to be implanted within the actuator layup. Ideally, such UHM materials would be used to create the rigid extension. However, because of concerns for shorting the piezo electrodes, non-conductive fiberglass layers are used. Since extension compliance is a significant concern, the highest modulus glass material, unidirectional S2Glass, is layered to stiffen the extension. Each layer is laser-micromachined into desired shapes using a computer controlled precision pulsed laser (QuickLaze from New Wave Research, Inc) to control dimensions and relative ply angles. The composite material matrices are thermoset polymers initially in a catalyzed uncured state (called prepreg) and are cut in this state. After all materials are cut, the layers are assembled with the desired layup and cured in a vacuum oven. The bonding between each layer is achieved by the flow of the composite matrix epoxy while curing. Thus, the actuator requires neither electrodes nor additional bonding layers. Figure 3.24 shows the steps in creating the bimorph actuators. First the central carbon fiber layer is laser-micromachined and aligned to the extension reinforcing SGlass layers (a-b). Next the piezoelectric layer is attached along with the remaining reinforcing layers (c-d). This structure is released from the substrate, flipped, and steps (a) through (d) are repeated. This is then cured and released. To determine what the geometric parameters

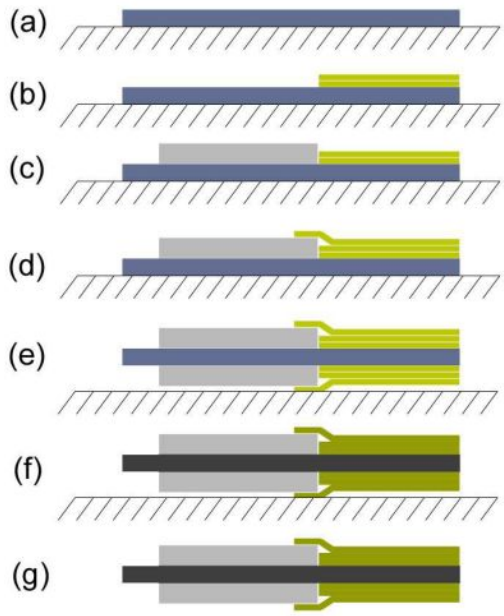

Figure 3.24: Process for creating composite bimorphs.

need to be for the desired application, the effects of the various constituent parameters in Table 3.4 on the output parameters are determined. First, the width ratio and the length ratio are maximized to the highest practical degree. For practical applications, the width ratio will not reach the maximum value of 2 since a distal end with zero thickness results in too fragile a structure, and the connection to the extension needs to be as rigid as possible. The length ratio cannot be increased indefinitely since the extension mass becomes a concern. The current design uses a width ratio of 1.5 and an extension ratio of 1.

The remaining parameters of length, width and thickness are determined through an optimization of the energy density based upon the desired displacement, blocked force, and stiffness parameters. This is done under the constraint that the piezoelectric plates are available only in one set thickness. The width affects only the blocked force and stiffness,

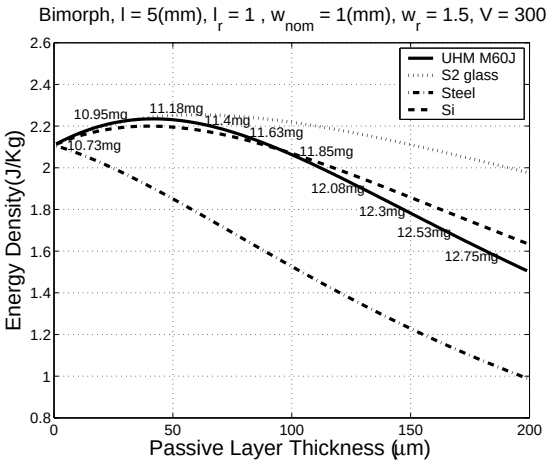

Figure 3.25: Effect of passive layer thickness on energy density for a bimorph.

not the displacement as was shown in section 3.3. The displacement scales with the length squared, the blocked force scales with the ratio of the nominal width to the length. The relation of these three parameters to the three output parameters is given as follows:

$$\begin{aligned} D_U &= g_1(t_r) \\ \delta &= g_2(t_r, l) \\ F_b &= g_3(t_r, l, w_{nom}) \end{aligned} \tag{3.87}$$

where l and w_{nom} are again the actuator length and nominal width respectively and t_r is the ratio of the passive layer thickness to a single piezoelectric plate thickness. First, for given constituent layer mechanical and piezoelectric properties, the energy density is maximized over the passive layer thickness.

From this plot it can be seen that the maximum energy density occurs at a passive layer thickness of approximately $40\mu m$ for a bimorph. Note that in both plots, the UHM energy density is plotted alongside similar curves for other common engineering materials

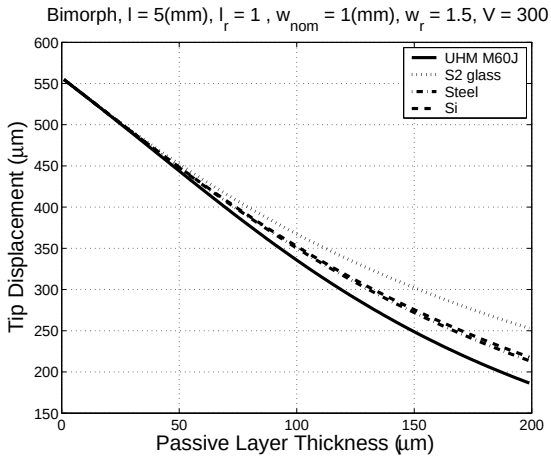

Figure 3.26: Effect of passive layer thickness on displacement for a bimorph.

for comparison reasons. Now the remaining two parameters, the displacement and blocked force, have two unknowns, the length and the nominal width. Solving these two equations, given a desired displacement of $400\mu m$ of displacement and $100mN$ of blocked force gives the length and width parameters for the bimorph and are listed in Table 3.5. Note that the actual results are slightly altered since the passive layer thickness is determined by how many UHM layers are used and the pressure applied during curing.

Again, for reasons of comparison, the displacement and blocked force as a function of thickness are given in Figures 3.26 and 3.27.

3.5 Driving Techniques

There are a number of traditional methods for how to apply a field to both unimorph and bimorph bending actuators. For unimorph actuators an electric field is applied across the thickness of the piezoelectric material. This is done either parallel or antiparallel

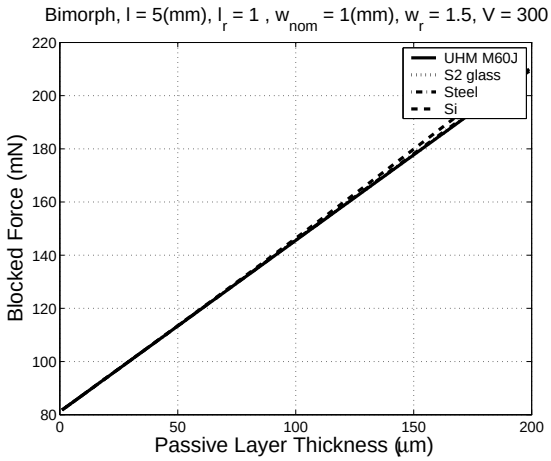

Figure 3.27: Effect of passive layer thickness on blocked force for a bimorph.

to the polarization direction. If the field is applied antiparallel, and either the field magnitude is sufficiently large or the ambient temperature is close to the Curie temperature, depoling or reverse poling can occur.

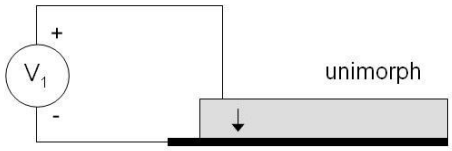

Figure 3.28: Unimorph drive.

For a bimorph actuator, four distinct methods will be described for how to apply an electric field across both piezoelectric layers and the associated benefits and difficulties associated with each technique. The first two methods require only a single source which is connected electrically in parallel or series with the three electrodes of the bimorph as described by Wang et al [90] as are shown in Figure 3.29. For the series case, the field is

applied across the two electrodes and the polarization of each piezoelectric layer is opposite. Thus the application of the electric field creates opposing strains in the two layers. For the case of the parallel configuration, the center electrode is grounded, while a positive voltage is applied to the outer two electrodes of similarly poled piezoelectric layers. Thus, instead of opposite polarizations, the field orientation creates the opposite strains. The major differences with these two methods are that the series configuration will require twice the voltage to obtain the same field, while the parallel method requires one additional connection. The overall problem with these two methods lies in the limit of the field that could be applied before depoling occurs within the layer that is poled opposite to the field direction. For PZT at room temperature, this is roughly $0.5V\mu m^{-1}$, however the desired field is approximately 2 to $3V\mu m^{-1}$ which would depole one of the layers, making the actuator useless. Again, this effect is amplified as the temperature approaches the Curie temperature. Therefore, to obtain the highest possible performance, each piezoelectric layer must be kept under positive field with respect to its polarization direction.

These two methods (shown in Figure 3.29) have the obvious benefit of requiring limited wiring, however for this application the combination of high stresses involved and electric field applied would depole one of the piezoelectric layers and possibly repole it with the opposite polarity. Thus the achievable energy density would be much too low for either of these techniques.

Thus independent drive is desired for each of the layers. The two source drive schematics are shown in Figure 3.30. The first of these two is termed the alternating drive and has two sources, one driving either layer. Each source is kept 180° out of phase with

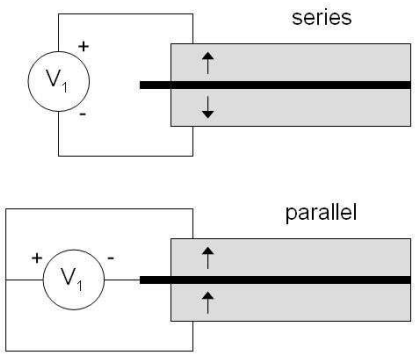

Figure 3.29: Single source bimorph drive schematic for (a) series connection and (b) parallel connection.

each other, each driven unipolar. This keeps each layer driven only in a positive sense, however requires two independent sources for each actuator, and thus a total of $2n + 1$ wires. The second option, termed the simultaneous drive, instead biases the entire actuator. Thus the bias and ground can be common for multiple actuators, requiring $n + 2$ wires per MFI actuator. Thus a total of nine wires are required for a 4DOF MFI driven with the alternating method, as compared to six for the simultaneous method.

3.6 Static Performance

The energy was derived by individually measuring the displacement and blocked force using custom built optical [4] and strain [97] sensors respectively. First, each driving method is evaluated based upon the static performance with no applied load. The results show that the alternating method exhibits greater saturation, while providing approximately 5% less displacement than the simultaneous drive for a given maximum field. Under cyclic actuation however, the simultaneous drive shows slightly greater hysteresis.

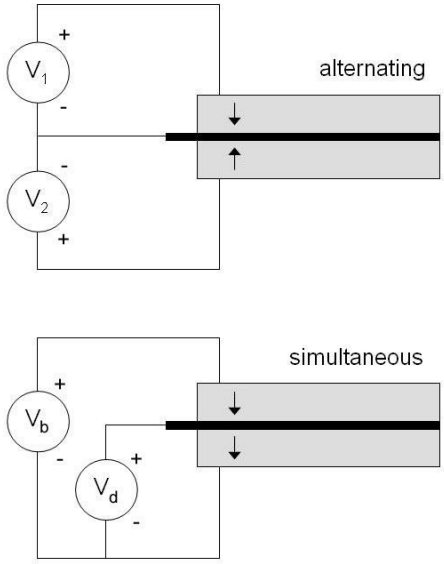

Figure 3.30: Dual source bimorph drive schematic for (a) alternate and (b) simultaneous drive.

These three differences can be seen by a comparison of the output traces in Figures 3.31 and 3.32(a). Since for the simultaneous case the relative magnitudes of the bias field and maximum drive field are variable, an attempt was made to compensate for this hysteresis increase by increasing the relative magnitude of the bias field. The idea is that the added hysteresis originates from stress depolarization of the piezoelectric plate which is experiencing relatively less magnitude field during any given half stroke. The field at this point is less than is required to maintain polarization while under high tensile stresses. The results of this test, in Figure 3.32(b), show that this principle of reducing the hysteresis does work, however the amplitude displacment decreases significantly.

For hysteresis comparison of the two driving schemes, first a valid parameter for the comparison must be generated. This is because the drive fields for the two methods are on different scales. Consider the total field which is seen across the thickness of the entire

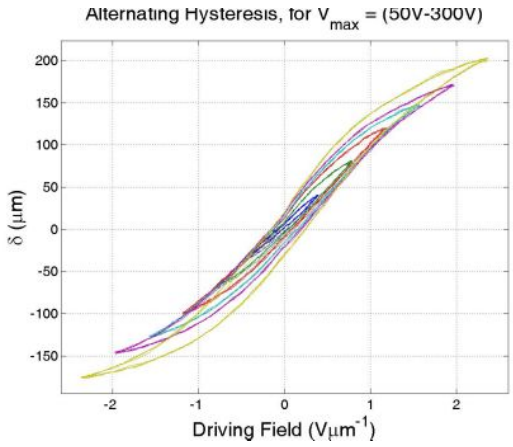

Figure 3.31: Hysteresis plots for alternating driving scheme.

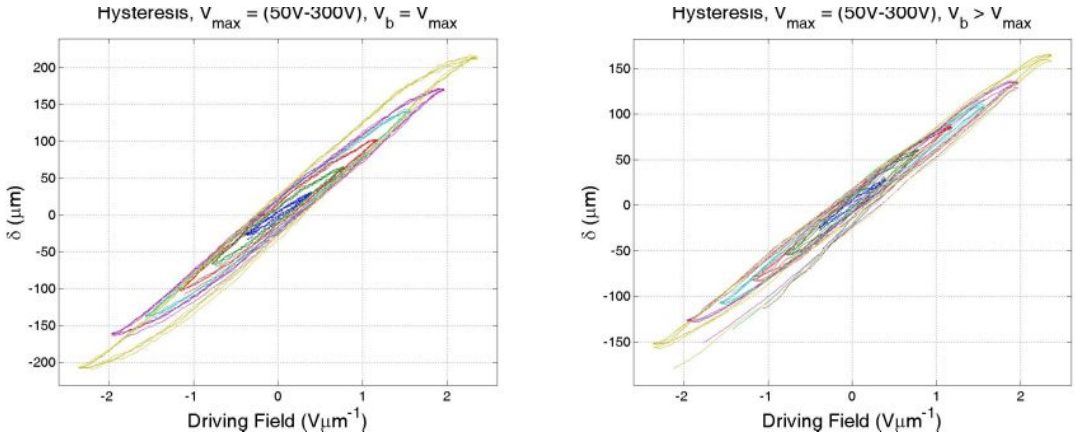

Figure 3.32: Hysteresis plots for (a) equal bias and (b) increased bias simultaneous driving methods.

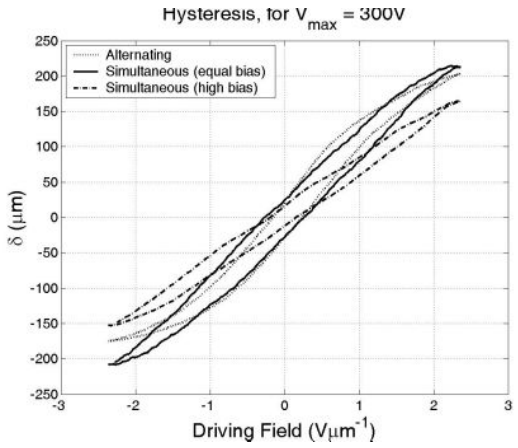

Figure 3.33: Comparison of hysteresis plots for all three two source driving methods.

bimorph parallel to the polarization direction. For the case of the alternating drive this is equivalent to $\Delta E = (V_1 - V_2)\, t_p^{-1}$. For the simultaneous case, this same total field is given by $\Delta E = (2V_b - V_d)\, t_p^{-1}$ where V_b is the bias voltage and V_d is the drive voltage.

Figure 3.33 shows a high-field comparison of each of the three two-source driving schemes for a bimorph actuator. Since the current application has the requirement of the highest possible mechanical power, without consideration for electric power, while at the same time requiring as simple a configuration as possible, the equal bias simultaneous method is used throughout the remainder of this discussion.

Next, the linearity and hysteresis in blocked force were examined using a custom built load cell [97]. This was done first by incrementally applying a field to a bimorph, optically zeroing the actuator displacement with the load cell, and measuring the resulting force. This gives a very linear curve for the blocked force as a function of field as is shown in Figure 3.34. To quantify the hysteresis in the blocked force, the load cell was put in contact with the free end of the actuator and the bimorph was driven from $V_d = 0$ to V_{max} where

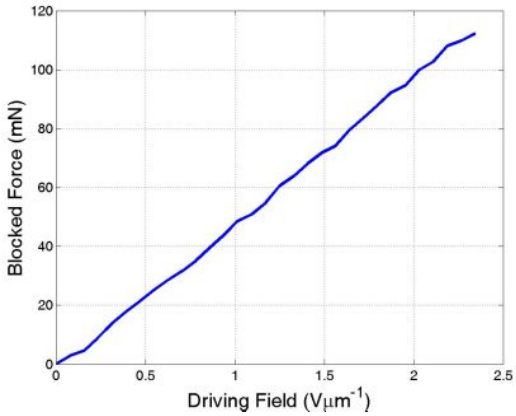

Figure 3.34: Blocked force with the drive field.

$V_{max} = V_b$ for incrementally increased bias fields. The results are shown in Figure 3.35.

It is well understood that piezoelectric materials undergo a softening at higher fields. This softening will be apparent when observing the Q and resonant frequencies as a function of the applied field. As an example of this effect, the frequency response of an unloaded bimorph was determined using custom built optical position sensors [4] for incrementally increased field magnitudes. Since the actuator is a high Q system, this could not be done up to the field magnitudes that will be experienced when connected to a load. The results are shown in figure 3.36.

From the frequency response seen in Figure 3.36, the resonant frequency and Q can be extracted as a function of the field magnitude. Note that the actuator is driven in simultaneous mode with $V_{max} = V_b$. The results are shown in Figure 3.37.

Finally, the performance of the bimorph actuators described here are given in Table 3.5. Note that in Tab. 3.5 there are two known causes of the difference between the predicted and experimental performance values. The first is due to stress based d_{31}

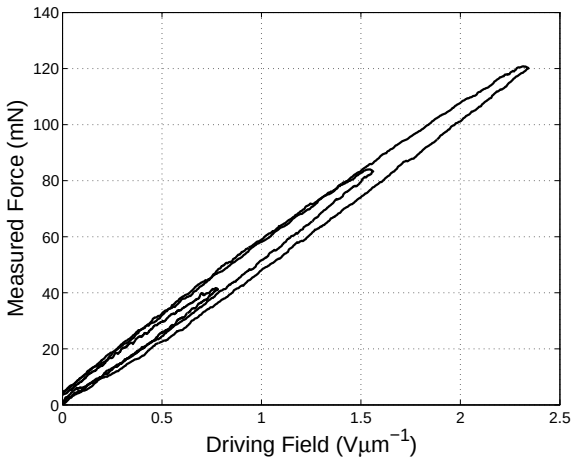

Figure 3.35: Force transducer measurements from bimorph showing hysteresis.

enhancements. It is known that the piezoelectric coupling coefficients of polycrystalline piezoceramics is increased with applied tensile stress and decreased with compressive stress [1, 56, 104]. For the case of the bimorphs described here, the piezoelectric plate performing work is always in tension (either imposed elastically from the opposite plate or from an external reaction force) and will increase both peak displacement and blocked force. The second cause for the discrepancy is piezoceramic softening under high drive fields (as is displayed in the decrease in resonant frequency shown in Figure 3.36(a)). This softening

Table 3.5: Performance results for energy density optimized bimorph piezoelectric bending actuators (for $N = 32$ actuators, simultaneous drive, $2.4V\mu m^{-1}$).

Parameter	Units	Predicted	Measured	Error
δ[1]	μm	406	520 ± 56.9	+28.1%
F_b[1]	mN	136	123 ± 20.5	−9.6%
m	mg	11.72	11.75 ± 0.8	+2.6%
U_m	μJ	28	32 ± 7.1	+14.3%
D_U	Jkg^{-1}	2.35	2.73 ± 0.5	+16.2%

[1]peak to peak

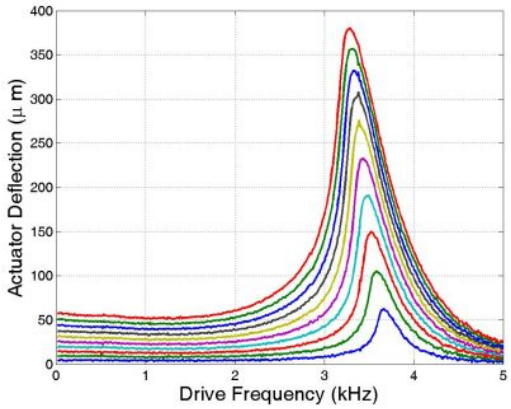

Figure 3.36: Bimorph frequency response for varying field magnitudes.

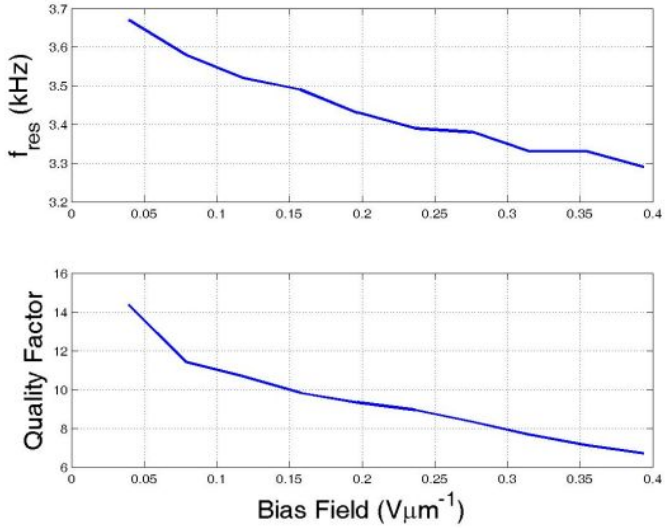

Figure 3.37: How the bimorph resonant frequency and Q change with an increase in applied field.

will result in an increase in displacement and a decrease in blocked force. Corrections for these effects will not be presented here, other than noting that altering d_{31} and the elastic modulus values as a function of applied field causes the predicted and measured performance

to be nearly identical.

At the beginning of this chapter, the concept of high energy density actuators was introduced as a structure in which all active materials are driven as close as possible to the maximum achievable strain of that given material (limited by either saturation, fracture, breakdown, etc). It is desirable at this point to estimate analytically the strain present in each layer of the actuators due to internal (thermal expansion, piezoelectric displacement) and external (external loads) excitations typically expected for the given application. This is readily accomplished by calculating the midplane strains and curvatures by substituting in the internal and external forces and moments into equation (3.17) and then applying this to each layer via equation (3.30). This ease of strain analysis is an ancillary benefit of using laminate plate theory for the design of bending actuators and sensors. The thermal, piezoelectric, external, and total strains (because of the principle of superposition) are shown for the outer surface of the top (because of symmetry) piezoelectric layer in Figure 3.38 for a bimorph. Note that the mechanical fracture strain for bulk free PZT-5H is approximately 0.3%.

The numerous improvements made to the actuators throughout the discussion of this chapter are quantified and shown in Table 3.6.

Table 3.6: Quantification of actuator improvements with respect to traditional rectangular.

Method	D_U Improvement	Fracture Load Improvement
Geometry	%30	%50
Use of UHM Materials	%10	—
Polishing	—	%20
Crack Closing Techniques	—	%10
High field drive	%300	—
Total	%340	%80

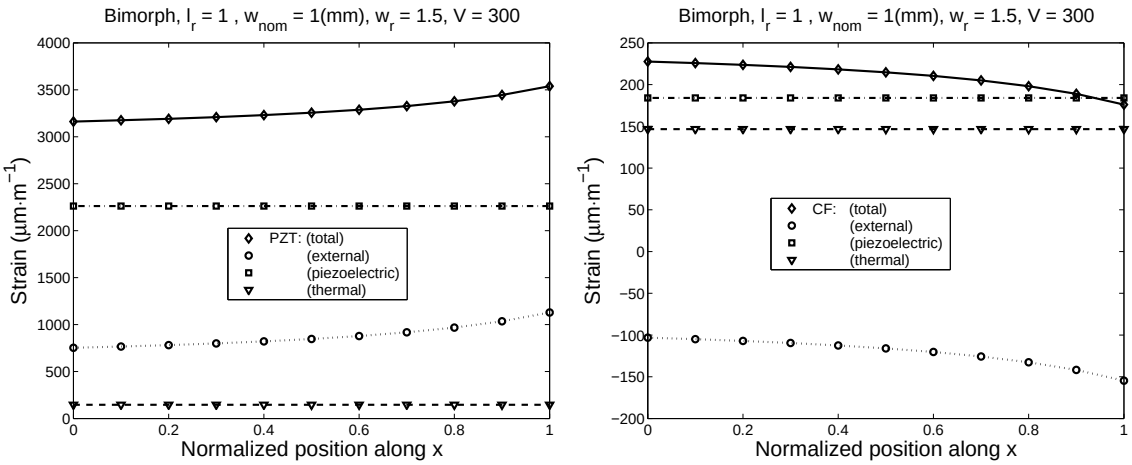

Figure 3.38: Strains in the piezoelectric layers and carbon fiber layer of the bimorph actuator with parameters described in Table 3.5.

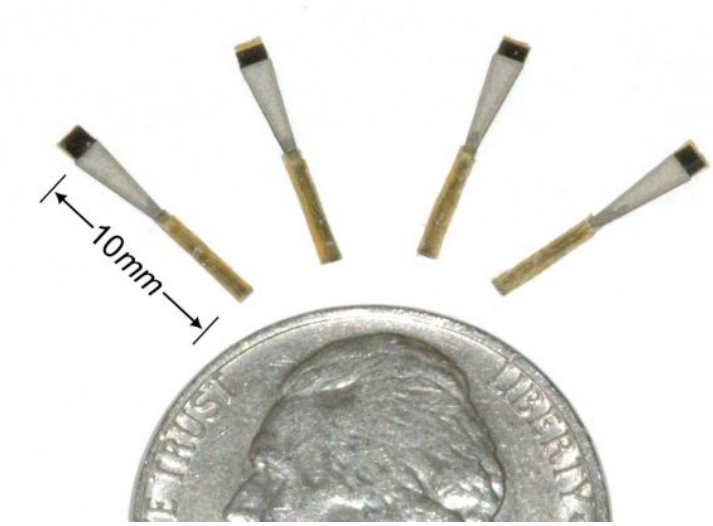

Figure 3.39: Completed bimorph actuator

3.6.1 Creep

Creep is a phenomenon which appears in the voltage-displacement characteristics of piezoelectric ceramics as a viscoelastic material property. The presence of creep can cause

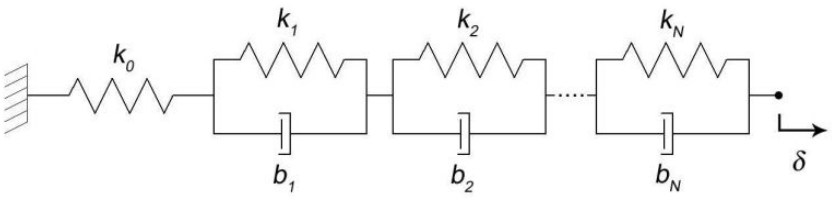

Figure 3.40: Generalized Kelvin-Voigt model for viscoelastic materials.

substantial errors for precision positioning actuators, or could affect the dynamics of power actuators at low frequencies. Creep exists in both the electrical and mechanical domains, however it is modeled by a series connection of parallel spring damper elements collectively called the generalized Kelvin-Voigt model and is shown below. This model for viscoelastic materials is similar to those in [55, 75]. As the number of elements N is increased, a very accurate fit to creep data can be obtained, however each additional spring damper element increases the order of the model. The displacement $\delta(t)$ for the system in Figure 3.40 is derived as follows:

$$\delta(t) = F_0 u(t) \left[\frac{1}{k_0} + \sum_{n=1}^{N} \frac{1}{k_n} \left(1 - e^{-\frac{t}{\tau_n}} \right) \right], \tag{3.88}$$

where $\tau_n = b_n/k_n$ and the the F_0 term is the static internally applied stress from the piezoelectric effect and $u(t)$ is the unit step. Ideally, creep would be observed by applying a static field and watching the displacement for $t > 0$. This is not practical for the case of a bending actuator however since the Q is typically high, thus such a test will cause mechanical failure. Instead, the applied field was ramped slowly to a set value (in this case $0.5V\mu m^{-1}$), but done so such that the ramp time was significantly lower than $\min(\tau_n)$ (for this test, the ramp was completed in $0.2s$) to mimic a step input. Finally, the steady state field value was kept small so as to eliminate the effects of high field displacement saturation

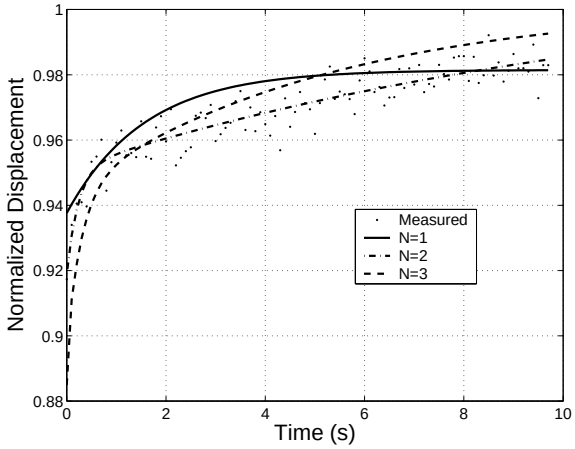

Figure 3.41: Creep data with fit to Kelvin-Voigt models of increasing order.

as in [19]. A nonlinear least squares regression fitting of this measured displacement to the model parameters in Figure 3.40 was done for various model orders and is shown in Figure 3.41. Note that this is done for one set field value. It is assumed that this will not scale with increasing field because of softening and other effects discussed later.

3.6.2 Saturation and Hysteresis

Displacement-voltage saturation is common for piezoelectric ceramics operating at high fields. This is due to the finite strain available through domain reorientation. The model for saturation is analogous to the Kelvin-Voigt model for creep but is instead a number of parallel series of spring dampers called the Maxwell slip model similar to that in [39] and is shown in Figure 3.42. The dampers in the above model are not viscous, but instead are analogous to Coulomb friction in which a break away force f^b must be overcome

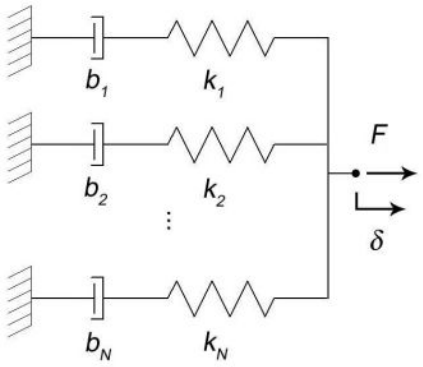

Figure 3.42: Maxwell stick-slip model for actuator saturation.

to achieve any motion. Since the elements are in parallel, the forces add as follows:

$$F = \sum_{n\in\Omega} k_n \left(\delta - \delta_n^d\right) + \sum_{m\in\Psi} f_m^b \operatorname{sgn}\left(\dot{\delta}\right), \tag{3.89}$$

and the individual damper positions are defined as:

$$\left[\delta^d\right] = \begin{cases} \delta_i^d : i \in \Omega \\ \delta - \frac{f_j^b}{k_j} \operatorname{sgn}\left(\dot{\delta}\right) : j \in \Psi \end{cases}, \tag{3.90}$$

where in equations 3.89 and 3.90 the sets Ω and Ψ are defined as $\Omega = \left\{i : \left|k_i\left(\delta - \delta_i^d\right)\right| < f_i^b\right\}$ and $\Psi = \left\{j : \left|k_j\left(\delta - \delta_j^d\right)\right| \geq f_j^b\right\}$. Note that the sum of the sizes of the two sets must equal N, the number of Maxwell slip elements. An experimentally measured hysteresis curve is shown in Figure 3.43 along with the model fit.

3.6.3 Stress-based Effects

Finally, it is desired to discover if the displacement properties of the actuator change with increased external loading. This is done by again performing hysteresis tests, however in this case static loads are applied to the actuator. For the case of the actuator

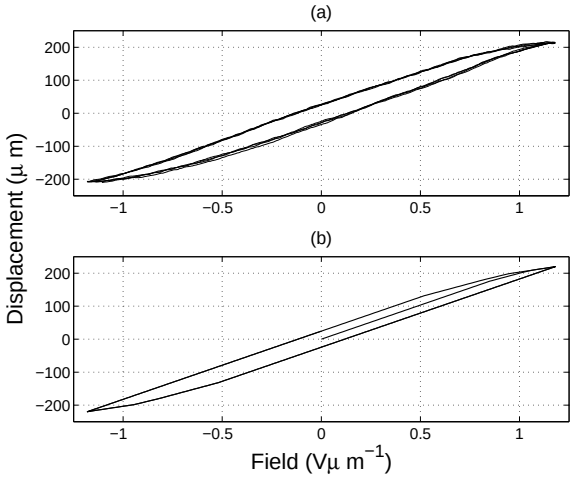

Figure 3.43: Measured hysteresis (a) and fit to Maxwell slip model (b).

in question, the loads chosen are of the order of the maximum loading expected during use (0, 50, and $100mN$). The actuator is brought to the neutral position, the load is applied, and the voltage is ramped from $V_b/2$ to V_b for a number of cycles while observing the tip displacement. If there is stress based saturation or softening of the piezoelectric material, the displacement magnitude will decrease with increasing external loading. For a linear actuator, the range of motion will remain the same for any arbitrary loading, thus any stress based effects will appear as another nonlinearity. The hysteresis loops for the three loads are shown in Figure 3.44. What is interesting from these results is that there is no saturation, however there is a slight inverse effect. Note that the magnitude of the displacement with an applied load is greater than that with no load. This is easily explained by the presence of stress based d_{31} enhancement. It has been shown [1, 56, 104, 112] that compressive stress on PZT degrades the piezoelectric coupling coefficients while tensile stress causes an enhancement. Applying a load to the distal end of a bimorph actuator puts the

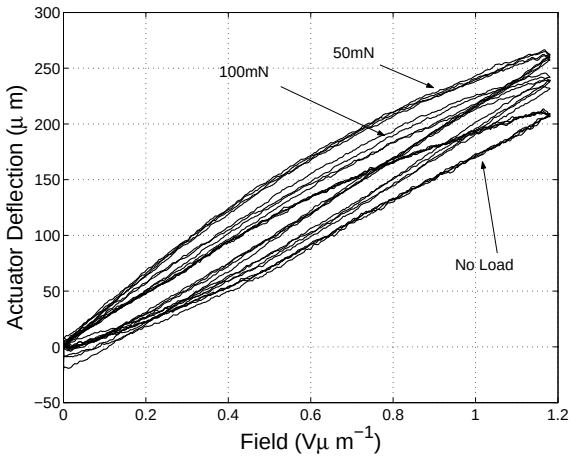

Figure 3.44: Work loop for various applied static loads (normalized to begin at 0 displacement).

PZT surface which is doing work on the load in tension, causing the above phenomena.

3.7 Dynamic Model

Wood [98] described how the quasi-static performance and stiffness of an actuator will vary with extension length and degree of tapering for a given field. Here, the remaining dynamic parameters are derived. The mechanical model used to describe the actuator dynamic performance is shown in Figure 3.45.

3.7.1 Stiffness

In section 3.3.3, the actuator stiffness is derived based upon the constitutive equations for actuator performance. Now this will be re-evaluated based upon empirical observations of softening. From Wood [98], the resonant frequency of the actuator falls as a function of the peak drive field as is shown in Figure 3.36. Since the effective cantilever

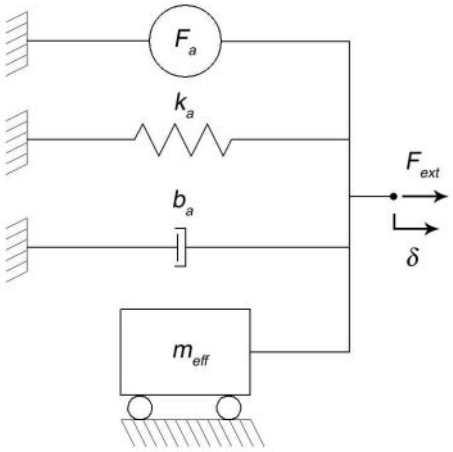

Figure 3.45: Mechanical model of actuator.

mass is static with respect to the applied field, and for a given fixed field, $2\pi f_0 = \sqrt{\frac{k_a}{m_{eff}}}$, the resonant frequency decrease is solely a function of the stiffness changing with the field. Thus highly accurate softening models can be extracted by frequency sweeps, such as the one in Figure 3.36, which would span the space of desired drive fields. Unfortunately, again this would fracture the actuator at high fields because of high unloaded Q. Thus, to determine the stiffness as a function of applied field, static loads are applied for increasing bias field strengths and the displacement is observed. This can be done because it is assumed that there are minimal saturation effects due to an applied load, as was shown in Figure 3.44. The stiffness is then extracted from this and is shown in Figure 3.46.

3.7.2 Equivalent Mass

The mass of a cantilever as represented by the mass in the system in Figure 3.45 is termed the effective mass, m_{eff}. This quantity is determined by calculating the kinetic

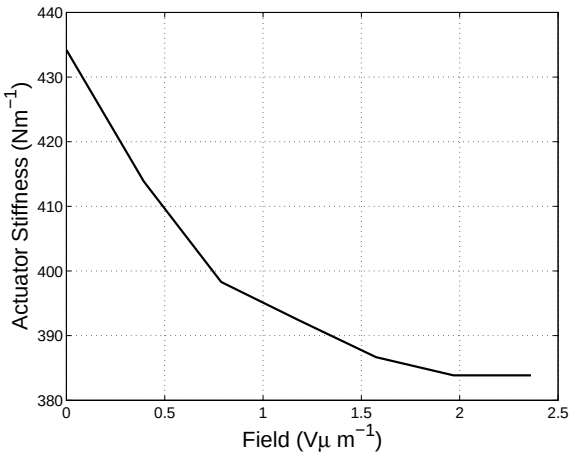

Figure 3.46: Empirically measured actuator stiffness with increased field.

energy of a massless rod with a point mass at the distal end and equating this to the sum of each particle in the beam. The kinetic energy of an oscillating point mass at the distal

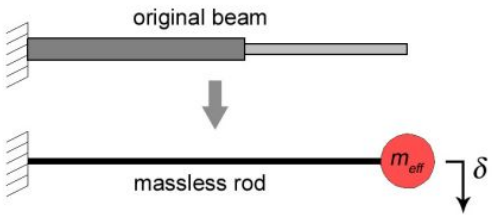

Figure 3.47: Model for calculating the effective mass of a cantilever.

and of a massless rod is given by the following:

$$T = \frac{1}{2} m_{eff} \dot{\delta}\left(l\right)^2 . \tag{3.91}$$

Equivalently the distributed kinetic energy of a cantilever beam is:

$$T = \frac{1}{2} wt\rho \int_0^l \dot{\delta}\left(x\right)^2 dx, \tag{3.92}$$

where w, t, and ρ are the width, thickness, and density of the beam respectively. Rearranging the terms in (3.91) and (3.92) and solving for m_{eff} for a homogeneous rectangular beam gives,

$$m_{eff} = m_{beam} \frac{\int_0^l \dot{\delta}(x)^2 \, dx}{l\dot{\delta}(l)^2}, \tag{3.93}$$

or $m_{eff} = m_{beam} M$ where m_{beam} is the gross beam mass defined as $wtl\rho$. For a rectangular beam with a point load, the term $\delta(x)$ is given in equation (3.24). Substituting this into equation (3.93) yields the result for a straight cantilever beam, $m_{eff} = \frac{33}{140} m_{beam}$. This gets to be more difficult when considering beams which are tapered along the length. For this case equation (3.93) becomes:

$$m_{eff} = m_{beam} \frac{\int_0^l \dot{\delta}(x)^2 \, \frac{w(x)}{w_{nom}} dx}{l\dot{\delta}(l)^2}, \tag{3.94}$$

where now m_{beam} is $w_{nom} tl\rho$, and $\delta(x)$ is given in equation (3.33). Now $M(w_r)$ can be explicitly defined (using the displacement defined in section 3.1.3):

$$M(w_r) = \frac{g_4 + g_5 + g_6 + g_7}{g_8}, \tag{3.95}$$

where the g_i terms are given in equation (3.96).

$$\begin{aligned}
g_4 &= 2g_1 \left(-39624 + w_r \left(135808 + w_r \left(-182782 + w_r \left(120878 + w_r \left(-39257 + 4992 w_r\right)\right)\right)\right)\right) \\
g_5 &= 450 g_2^6 \ln(2 - w_r)^2 \\
g_6 &= 15 g_2^4 \ln(2 - w_r) \left(-396 + (676 - 279 w_r) w_r - 60 g_2^2 \ln(w_r)\right) \\
g_7 &= 15 g_2^4 \ln(w_r) \left(396 + (-676 + 279 w_r) w_r + 30 g_2^2 \ln(w_r)\right) \\
g_8 &= 3600 g_1 \left(-6 + 10 w_r - 4 w_r^2 + g_2^2 \ln\left(\tfrac{2 - w_r}{w_r}\right)\right)
\end{aligned} \tag{3.96}$$

This function is plotted in Figure 3.48. Note that $\lim_{w_r \to 1} = \frac{33}{140}$ yields the same result as

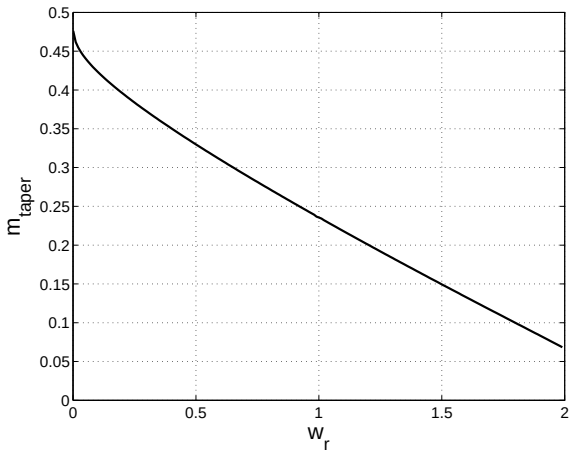

Figure 3.48: $M(w_r)$ for values of w_r.

for the rectangular beam. Next, the effective mass is determined for a rectangular cantilever with a rigid extension. This is done by splitting the integral in equation (3.93) to account for the discontinuity in displacement as a function of x.

$$m_{eff} = m_{beam} \frac{\int_0^l \dot{\delta}(x)^2 \, dx + d_r \int_l^{l(1+l_r)} \dot{\delta}(x)^2 \, dx}{l(1 + d_r l_r) \dot{\delta}(l + l_{ext})^2}, \tag{3.97}$$

here l_r is the extension ratio equal to l_{ext}/l, m_{beam} is again the gross mass of the beam, $wl \sum \rho_b t_b (1 + l_r d_r)$ where d_r is defined as:

$$d_r = \frac{\sum_{n=1}^{N_e} \rho_e(n) t_e(n)}{\sum_{n=1}^{N_b} \rho_b(n) t_b(n)}, \tag{3.98}$$

where $\rho_i(n)$ and $t_i(n)$ are the density and thickness of the n^{th} layer of i^{th} section ($i \in \{b, e\}$) respectively, and N_b and N_e are the number of layers in the beam and extension. For a beam with a rigid extension, the $\delta(x)$ term is defined in equations (3.61) and (3.64). Solving equation (3.97) yields the result shown in equation (3.99).

$$M(l_r, d_r) = \frac{33 + 7l_r(13 + 9l_r + 5d_r(4 + 3l_r(6 + l_r(11 + 2l_r(5 + 2l_r)))))}{140(1 + d_r l_r)(1 + 3l_r(1 + l_r))^2} \tag{3.99}$$

This solution is plotted as a function of both l_r and d_r in Figure 3.49. Note once again that $M(0, d_r) = \frac{33}{140}$. Finally, these two results are combined to form a solution for $M(w_r, l_r, d_r)$.

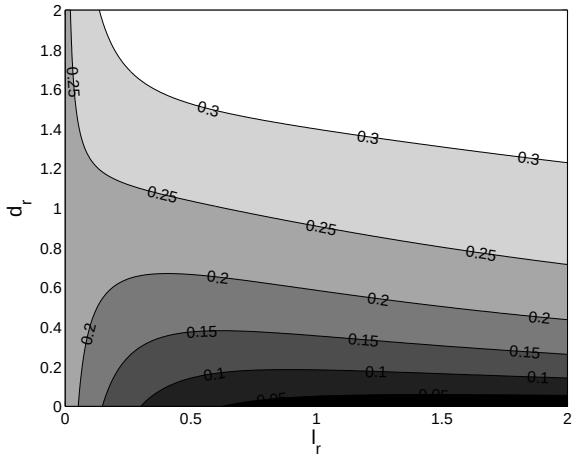

Figure 3.49: $M(l_r, d_r)$ for typical ranges of l_r and d_r

Again the effective mass is calculated as follows:

$$M = \frac{\int_0^l \dot{\delta}(x)^2 \frac{w(x)}{w_{nom}} dx + (2 - w_r) d_r \int_l^{l(1+l_r)} \dot{\delta}(x)^2 dx}{l(1 + d_r l_r (2 - w_r)) \dot{\delta}(l + l_{ext})^2}. \tag{3.100}$$

The displacement is defined as a combination of equations (3.33) and (3.61) and is shown in section 3.3.3. Substituting this into equation (3.100) yields the complete result for the effective mass of a tapered beam with a rigid extension. A few level sets are shown in Figure 3.50 for discrete values of d_r.

$$M(w_r, l_r, d_r) = \frac{g_{13} + g_{14} + g_{15} + g_{16}}{g_{17}} \tag{3.101}$$

The terms g_9, g_{10}, and g_{11} are $2l_r g_1 + w_r - 2$, $2w_r - 3$, and $5w_r - 9$ respectively while the remaining g_i terms are given in equation (3.102). This is shown for a few values of d_r in

Figure 3.50.

$$
\begin{aligned}
g_{12} &= 3g_2^3 + 8d_r l_r \left(3g_2^2 + 6l_r g_1 g_2 + 4l_r^2 g_1^2\right) g_1 \\
g_{13} &= 2g_1 \left(-39624 + 67200 d_r l_r^3 g_1^4 g_2 + 100 l_r^2 g_1^2 \left(-234 + 432 d_r g_1 g_2 g_{10} + \right.\right. \\
&\quad \left.\left. w_r \left(490 + w_r \left(-317 + 64 w_r\right)\right)\right) + g_{18} + g_{19}\right) \\
g_{14} &= 150 g_2 g_9^2 g_{12} \ln\left(2 - w_r\right)^2 \\
g_{15} &= 15 g_2 g_9 \ln\left(2 - w_r\right) \left(-3200 d_r l_r^3 g_1^4 - 960 d_r l_r^2 g_1^3 g_{11} - \right. \\
&\quad 10 l_r g_1 g_2 \left(96 d_r g_1 g_{10} + g_2 \left(31 w_r - 30\right)\right) - g_2^2 \left(396 + \right. \\
&\quad \left. w_r \left(279 w_r - 676\right)\right) - 20 g_9 g_1 2 \ln\left(w_r\right)\Big) \\
g_{16} &= 15 g_2 g_9 \ln\left(w_r\right) \left(3200 d_r l_r^3 g_1^4 + 960 d_r l_r^2 g_1^3 g_{11} + \right. \\
&\quad 10 l_r g_1 g_2 \left(96 d_r g_1 g_{10} + g_2 \left(31 w_r - 30\right)\right) + g_2^2 \left(396 + \right. \\
&\quad \left. w_r \left(279 w_r - 676\right)\right) + 10 g_9 g_1 2 \ln\left(w_r\right)\Big) \\
g_{18} &= 4 l_r g_1 \left(15156 + 1800 d_r g_1 g_2 g_{10}^2 + w_r \left(-41834 + w_r \left(41856 + w_r \left(-18039 + 2816 w_r\right)\right)\right)\right) \\
g_{19} &= w_r \left(135808 + w_r \left(-182782 + w_r \left(120878 + w_r \left(-39257 + 4992 w_r\right)\right)\right)\right)
\end{aligned}
\tag{3.102}
$$

Note that in all cases, the effective mass can be decreased through proper choice of geometry and material properties. This is a significant result since for a given stiffness, this will increase the actuator resonance. Thus for the same energy, this will yield higher power at the actuator resonance as well as give a higher bandwidth for control. For the example of a tapered actuator, the change in resonant frequency is determined via equations (3.52), (3.95) and is shown in Figure 3.51.

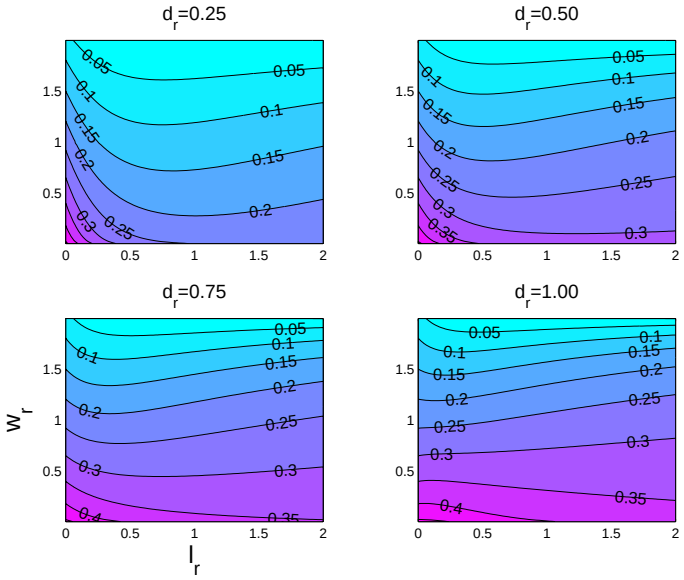

Figure 3.50: $M\left(w_r, l_r, d_r\right)$ for select values of d_r.

3.7.3 Losses

All of the loss elements are lumped into the damper in Figure 3.45, collectively called the actuator damping. Empirical measurements of damping for bending actuators is difficult to study since the Q of such structures is typically high, thus large DC motion will result in mechanical failure (fracture) of the system at resonance. Thus, such measurements must be made at either low fields or in the presence of an external damper. Models for structure damping such as in [18, 54] are useful for first order linear damping approximations, however it is known that the losses for such materials increase with increasing field. To empirically verify this, static hysteresis tests are performed for increasing field strengths and the loss as a function of this field is calculated by observing how the hysteresis area changes (assuming that the hysteresis is rate-independent). First, the model for the loss is

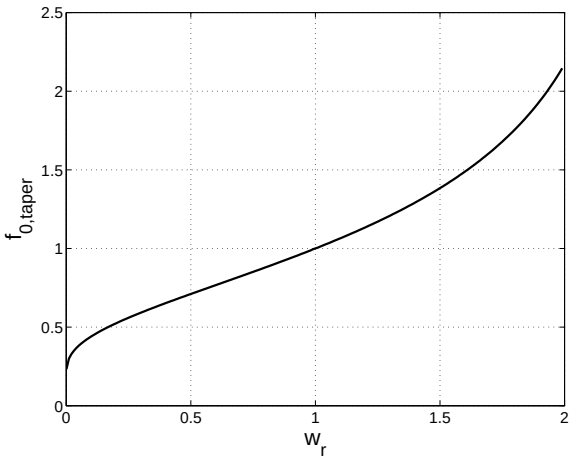

Figure 3.51: Change in resonant frequency with width ratio.

presented. This model is based upon the damping ratio and is given by the following:

$$b_a = 2\pi\zeta\sqrt{m_{eff}k_a}, \tag{3.103}$$

where ζ is the damping ratio which is related to the loss ratio $\eta = 2\zeta$ and the loss ratio (fraction of energy lost to total energy in one cycle) is defined as a transverse heat flow process in [18] by the following:

$$\eta = \frac{\alpha^2 E^Y T}{c_v} \frac{f_0/f_r}{1 + (f_0/f_r)^2}. \tag{3.104}$$

In the above equation, α, E^Y, T, and c_v are the coefficient of thermal expansion, Young's modulus, operating temperature, and specific heat respectively while f_0 is the resonant frequency and f_r is the relaxation frequency defined in equation (3.105).

$$f_r = \frac{\pi}{2} \frac{\kappa}{c_v t^2}. \tag{3.105}$$

In the above equation for the relaxation frequency, κ is the thermal conductivity and t is the beam thickness. For the composite actuator structure, this model gives a frequency

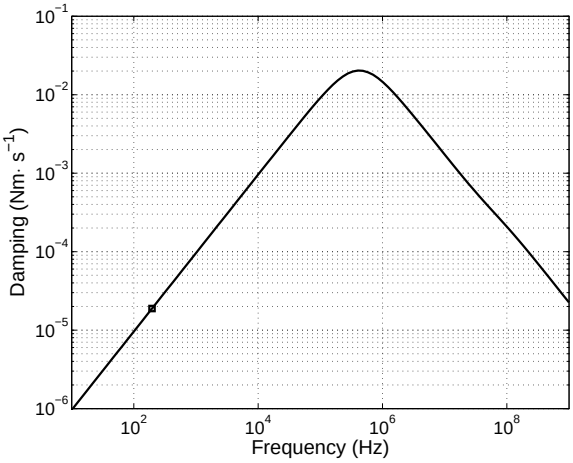

Figure 3.52: Mechanical actuator damping from [18].

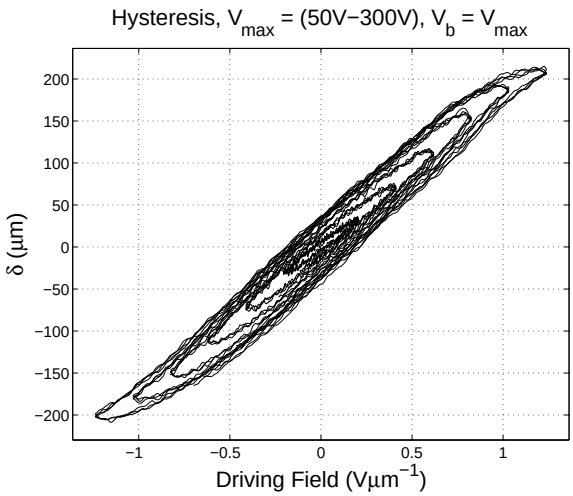

Figure 3.53: Hysteresis for increasing fields

dependent damping as is shown in Figure 3.52. Next the rate-independent losses from the actuator hysteresis are determined for increasing field strengths. Figure 3.53 shows the hysteresis loops for increasing fields with no load. From this, the loss can be measured by calculating the area in the hysteresis loop and comparing this to the total area under the

curve to calculate the loss ratio. Along with equation (3.103), this yields the damping curve shown in Figure 3.54. Note that it is assumed that this loss ratio is a function of amplitude but not frequency. The total actuator damping is the sum of the mechanical (traverse heat

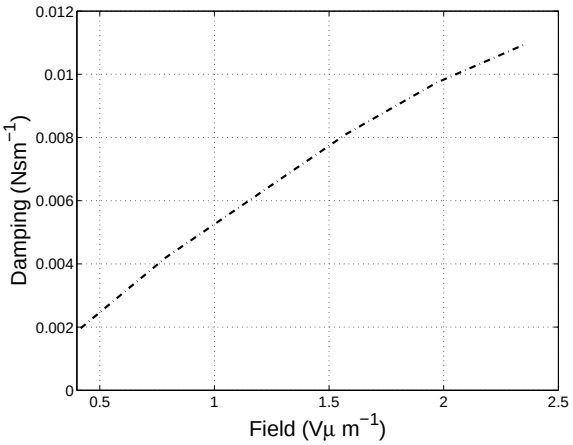

Figure 3.54: Damping extracted from measured loss along with model prediction.

flow) and hysteretic (electromechanical) damping terms.

Now all the pieces for the dynamic model are known and can be used to determine the equations of motion. Once this is complete, more interesting questions can be answered, such as actuator frequency response, power delivery capabilities, etc. The actuator model is:

$$m_{eff}\ddot{\delta} + b_a\left(E_3\right)\dot{\delta} + k_a\left(E_3\right)\delta = F_{ext} - F_a, \tag{3.106}$$

where δ represents $\delta\left(l + l_{ext}\right)$. This model can now be used to determine the dynamic response, for example the magnitude response for various fields as is shown in Fig. 3.55. A few interesting effects can be observed from the predicted frequency response. First, the Q degrades rapidly with increasing fields. Second, the peak displacement is a non-

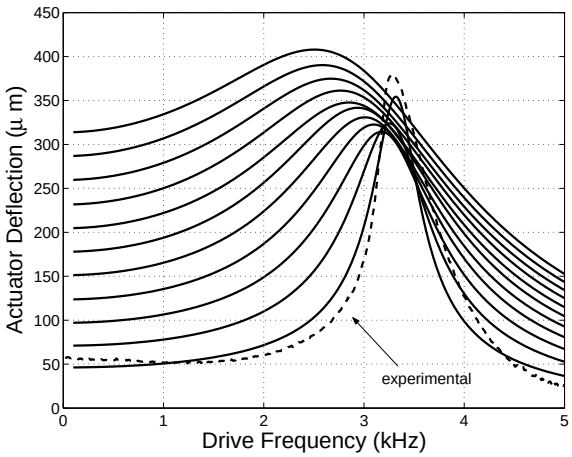

Figure 3.55: Magnitude frequency response predicted from dynamic model (high fields, $V_b = 50$ to $300V$) with $50V$ experimental response from Fig. 3.36 included.

monotonically increasing function of the drive field. Both of these are shown in Figure 3.56.

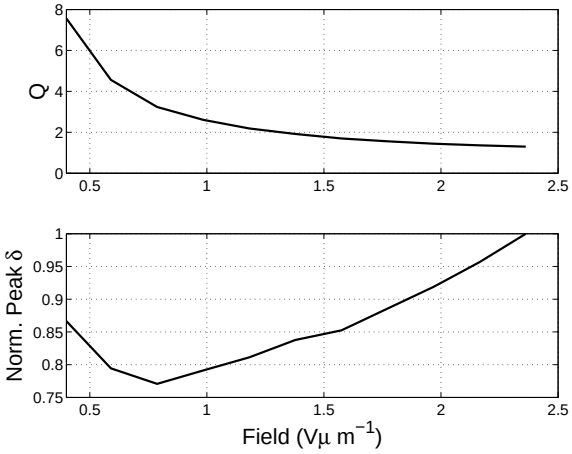

Figure 3.56: Quality factor (a) and peak displacement (b) as a function of drive field.

To calculate the power delivered to the load, it is important to know the load dynamics as well. Since this is a resonant system, all that is needed is the load damping b_l

from the wing. For the case of the MFI, each actuator sees approximately $9 \times 10^{-2} Nsm^{-1}$. The sum of the mechanical damping at $f_0 = 200Hz$ ($2 \times 10^{-5} Nsm^{-1}$) and the electromechanical damping at high fields ($1.1 \times 10^{-2} Nsm^{-1}$) yields the total actuator damping. The peak power delivered to the load is given by the following:

$$P_l = \frac{1}{2} \frac{F^2 b_l}{(b_l + b_a)^2} \tag{3.107}$$

where F is the peak blocked force. This yields a peak power of $10mW$ delivered to the load (placing the power density at $800Wkg^{-1}$ which is sufficient for the application [96]). It may appear that lowering the wing damping to match the actuator losses will increase the power delivered to the load. This is not true since decreased wing damping will increase the system Q. Observing Figure 3.38 it is apparent that the PZT layer is running very close to its fracture strain under normal operating conditions. Increasing the Q will increase the actuator displacement and thus the strain causing fracture. Finally, assuming that the wing inertia and actuator stiffness are the dominating components in determining the system quality factor, a Q of 2.4 is estimated for the complete system.

Chapter 4

Micromachined Composite Structures for the Thorax and Airframe

The MFI thorax, much as that of a flying insect's, converts the flight muscle work to motion required to drive the wings. As was previously stated, the MFI wings must be able to perform two of the three DOFs of real insects: simultaneous wing stroke and rotation. The wing drive for some insects is controlled directly as with the orders Odonata, Blattaria, Orthoptera, and Ephemeroptera. Such insects use muscles directly attached to the wing base to control the motion of the wings. In contrast, certain types of insects, such as the orders Diptera, Hymenoptera, and Coleoptera, control the wing stroke with one set of muscles (dorsolongitudinal and dorsoventral) and have smaller muscles (basalar and subalar) to do fine controlling of the wing rotations. The larger of the two sets of

muscles, the power muscles, actuate the wing through notal depressions [30] while the smaller muscles fine tune the wing motion by acting directly on the pleural wing process and the surrounding structure. Also similar to flying insects, the MFI wing drive is a resonant system. However, the direct muscles of certain insects have the ability to not only influence the wing's kinematics, but also the dynamics by adjusting the stiffness of the thorax. The MFI diverges from this method and uses two muscles per wing, both contributing equally to flapping and rotation. Since the actuators described in chapter 3 give small displacements and large forces, the MFI must also utilize a similar mechanical amplifying system. Along with the thorax, an airframe must be designed to connect all of the articulated sections of the MFI. This chapter describes in detail the transmission system which the actuators of the MFI use to drive the wings, along with the MFI exoskeleton.

4.1 Requirements and Design

The MFI consists of two wings, each with two degrees of freedom (DOF) driven by the bimorph piezoelectric actuators described in chapter 3. Because these actuators have relatively small displacements and large forces, a mechanical transmission system amplifies the motion and a differential mechanism maps two independent rotational motions to a flapping and a rotation of each wing. This mechanical transmission system consists of two planar four bar mechanisms and one spherical five bar differential per wing [96]. The MFI wing structure is a tuned resonant system, and as such, the compliances and inertias of each component within the four bars and five bar effect the output dynamics. Thus the link between the thorax and the actuators, as well as each individual member, must be as

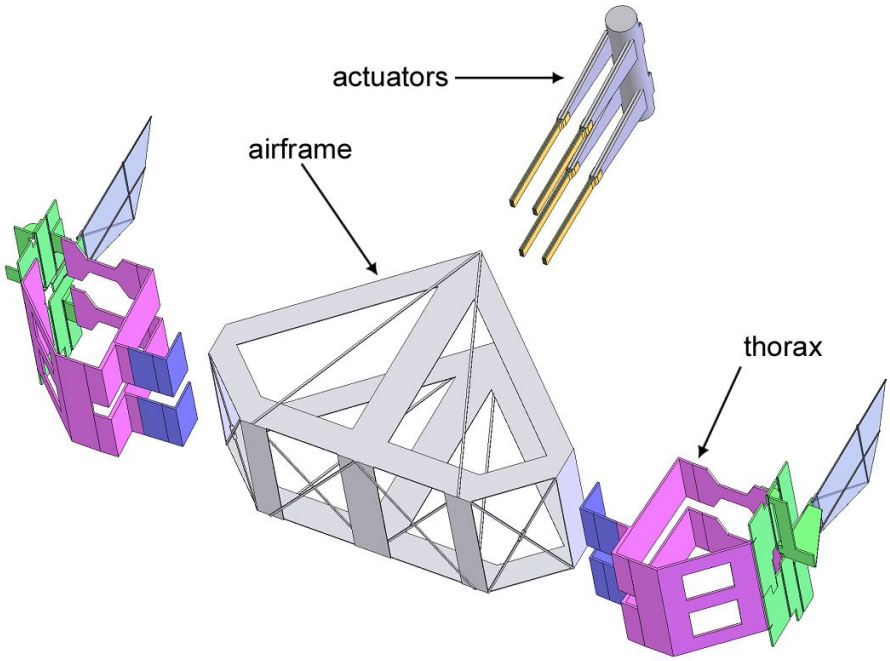

Figure 4.1: Exploded view of the MFI.

stiff and lightweight as possible. The total mass of all components must be kept small so as to create a complete insect with high maneuverability and extra payload capacity. The mass budget for each component within the MFI is given in Table 4.1.

Note that the data presented in Table 4.1 is for the final complete autonomous MFI. The work presented here has the goal of creating a prototype MFI which is capable of creating all of the necessary kinematics at the final scale, but which has off board power, control, and sensors. Thus, an interim mass budget is given in Table 4.2.

For the dynamic parameters of the thorax links, the inertias will be discussed later on. To motivate this discussion, it is prudent here to note that there are two problems that arise from heavy compliant elements of a serial resonant structure. First, high inertias

Table 4.1: Power and mass budget goals for the completed (two wing) MFI.

Component	Number	Mass (mg)	Power (mW)
four bar, s.c.	4	15	—
differential	2	4	—
wings	2	1	—
actuator	4	15	-30
airframe	1	10	—
battery	1	45	50
drive electronics	1	5	-5
control, comm.	1	5	-5
imager, lens[1]	1	15	-10
misc. payload	?	35	?
TOTALS	—	100 + 50	—

[1]estimated

Table 4.2: MFI mass budget goals for tethered MFI.

Component	Number	Mass (mg)
four bar, s.c.	4	20
differential	2	4
wings	2	1
actuators	4	50
actuator mount	1	10
airframe	1	15
TOTALS	—	100

decrease the resonant frequency, which for quasi-static mechanisms lowers the operating bandwidth. For resonant systems such as the MFI, the work done on the air is a quadratic function of the wing velocity, thus a lower resonant frequency will decrease the wing velocity and the magnitude of the lift generated. To maintain the same wing velocity, the kinematics would need to be adjusted for a higher stroke amplitude. This may not be an option for torque limited systems. Second, undesired compliance of any link (or joint) will result in either linear (elastic) or nonlinear (backlash or buckling) deformations which will affect the power delivery and controllability of the structure as a whole.

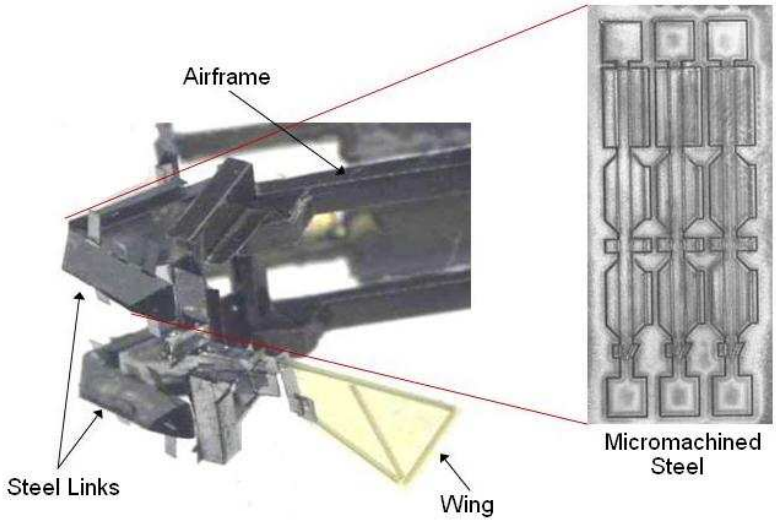

Figure 4.2: Previous steel-based version of the MFI.

4.2 Previous Methods

Previous to the inclusion of composite materials into the MFI thorax, the links were constructed from folded stainless steel beams. Such beams have high stiffnesses, however they are extremely difficult to make and are relatively massive. Figure 4.2 shows a previous version of the MFI which was constructed from folded triangle beams. Previous structures, such as the one shown in Figure 4.2, had a number of problems. First, the structural resonant frequency was too low, most often around $120Hz$. This was due to two underlying problems; the links had high inertias and high serial compliances due to peeling caused by poor bonding between the flexure material and the structural materials. Second, the mechanical Q was typically too high. This brings up a problem when attempting to control the motion of the wing. If the Q is too high, it will be difficult to drive the wing at any frequency other than resonance since the actuator torque is limited and will easily saturate.

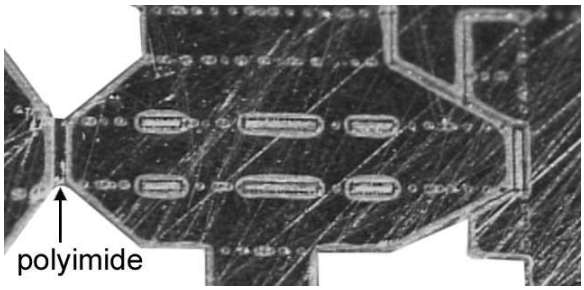

Figure 4.3: Polyimide coated laser micromachined steel with polyimide flexures.

Third, as will be discussed in section 4.5.1 the airframe which acts as a virtual ground for the thorax and actuators must be sufficiently stiff, thus designing a sufficiently lightweight airframe structure from metals may not be possible. Yan described a method of using similar folding techniques to create a $30mg$ steel airframe [102] however this needs to be reduced further and brought into the necessary form factor. Finally, the folded beam configuration used in previous designs causes a significant increase in construction time and difficulty. Each link contained three steel pieces which needed to be folded and bonded together and to the polymer flexure. Two configurations were used for the previous folded triangle MFI links, one using $12.5\mu m$ thick steel and the second, in an attempt to lower the inertias, used $6.25\mu m$ thick steel.

In an attempt to eliminate peeling and simplify the construction of the structure, polymer flexures were deposited onto the metal prior to folding. To do this, polyimide was spin coated onto the laser micromachined steel and cured to form the flexures. This is shown in Figure 4.3. Although the simplicity of construction was improved, numerous polyimides did not adhere well to the steel and peeling was rampant. Along with this, the deposited polyimide seemed to have a much lower fracture toughness than would be

expected for polyimide sheets and thus the resulting structures were very brittle.

Other attempts at high stiffness microstructures include hinged folded silicon triangle beams [106, 105]. The joints of these structures are polysilicon hinges which have limitations due to the limits of MEMs processing capabilities. The hinges essentially consist of square pegs in slightly larger square holes. Along with this, these hinges have high friction due to silicon on silicon contact. Thus not only is the range of motion limited, but the frequency of operation due to frictional losses. Another microrobot platform attempted to create articulated legs for a walking robot by embedding polyimide in between polysilicon links [31]. This device unified the actuation and transmission system through thermal actuation via the high CTE of the polyimide. This method has low friction, however is still limited in operation frequency due to the thermal conductivity of the constituent materials. It will also be shown that the performance of the materials used in these MEMs processes is eclipsed by composite materials.

To solve the thorax problems, subsequent designs used ultra high modulus (UHM) composite materials. The design of each piece of the composite MFI thorax along with the overall results is the main focus of this chapter. First, however, it is important to study whether or not it is possible to manufacture with composite materials at the millimeter scale and smaller.

4.3 Microfabrication of Composite Materials

Composite materials are considered for use in such high performance structures because of the high moduli and low densities associated with such materials. Also, certain

properties of the constituent materials are only possible when fibers are created. The first important consideration is the feasibility of using fiber-reinforced materials for the construction of micro devices. The links within the four bar and five bar structures have sizes ranging from $0.5mm$ to $6mm$ in length with widths of between $0.5mm$ to $3mm$. For these feature sizes, such construction is historically feasible. However when considering that the flexure width is crucial for proper rotation, calculations show that flexure lengths on the order of $100\mu m$ are necessary. Thus for fiber-reinforced composites with fiber diameters of roughly $10\mu m$, this is approximately the limiting feature size for these materials.

Using composites for this application assumes the ability to machine the laminates on a single ply basis, down to accuracies of approximately the fiber diameter. Thus traditional methods of cutting and handling these materials (stamp, saw, etc) is not possible at this scale. Instead, a laser micromachining stage (QuickLaze II from NewWave Research) [73] is used to cut the plies, both in a cured and an uncured state. To do this, all plies are designed using a two dimensional CAD package and a laser cuts the plies autonomously. For the links of the MFI, a material with a high stiffness-to-weight ratio was desired, thus M60J UHM carbon fiber reinforced epoxy was used. This is a common carbon fiber and thermoset epoxy combination that is available in single sheets of unidirectional prepreg down to $40\mu m$ thick. To eliminate errors during construction of the cut laminae, all angles are controlled within the 2D CAD layout, and the plies are aligned visually under a microscope before cutting. The last concern with laser micromachining these laminae is whether to cut the composite cured or uncured. Using uncured layers to construct the thorax has the great benefit of being able to layup the laminae for the links and a polymer for the joints at one

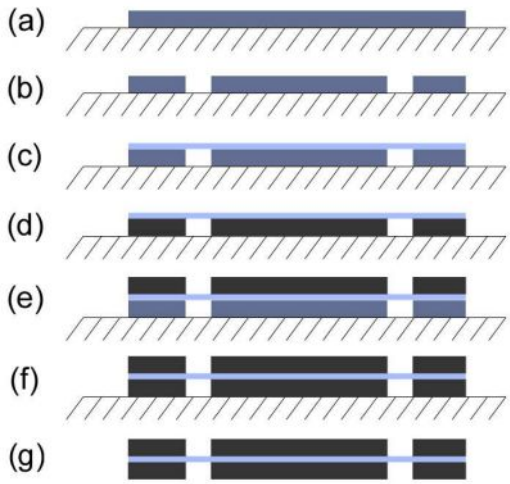

Figure 4.4: Process for creating composite articulated microstructures.

time, and cure this laminate without the need for extra adhesive layers. This simplifies construction, and cuts down on inertia by eliminating the need for any additional epoxy. Laser micromachining an uncured lamina has difficulties since the laser creates localized heating, causing the matrix epoxy to flow around the cutting area, possibly defocusing the laser. Thus laser cutting uncured lamina is possible, but becomes increasingly more difficult with smaller size parts and is only possible for one layer at a time. Also, since the uncured matrix is still in a viscoelastic state, smaller features can be easily destroyed in handling subsequent to cutting. Through careful practice and paying attention to these problems, the MFI thorax has evolved to using a construction based exclusively upon uncured prepreg laminae. Figure 4.4 shows the process for creating composite links and joints. First, the uncured composite material is aligned to the substrate (4.4(a)). The substrate in Figure 4.4 is a layer of Gelpac 8 upon glass. Next both the prepreg and flexure materials ($6\mu m$ thick polyester) are laser micromachined, layed up together, and cured (4.4(b-d)). Cur-

Table 4.3: Design parameters for MFI materials.

Parameter	M60J	S2Glass	Kevlar	Steel	Si	Units
E_1	350	60	73	193	190	GPa
E_2	7	7	7	193	190	GPa
ν_{12}	0.33	0.33	0.33	0.3	0.27	—
G_{12}	5	5	5	74	75	GPa
ρ	1500	1600	1600	7800	2300	$kg \cdot m^{-3}$

ing consists of four hours at $125°C$ under vacuum with a stress of approximately $100psi$ applied via loading or clamping. To separate the composites from the clamp faces teflon sheets are used. Subsequent to curing, this half structure is released from the substrate and layed up with another laser micromachined prepreg mirror layer and cured (4.4(e-f)). Finally this is again released from the substrate to create a planar assembly of links and joints which can then be folded into arbitrary articulated components. Table 4.3 shows the lamina parameters of each material considered throughout the designs.

4.4 Articulated Composite Mechanism Construction

Now the methods described in the previous section are applied to the design of the MFI thorax. This is done with structural dynamics in mind such that the resulting thorax is inherently controllable. The dynamic model of the MFI thorax and actuator system is shown in Figure 4.5 for a $1DOF$ system. It is assumed that the design of the entire system is such that all $4DOFs$ are completely independent. This section first describes joints and links which maximize k_s while minimizing k_p and J_{4R}. Next these joints and high links are used to create parallel mechanisms which form the thorax of the MFI.

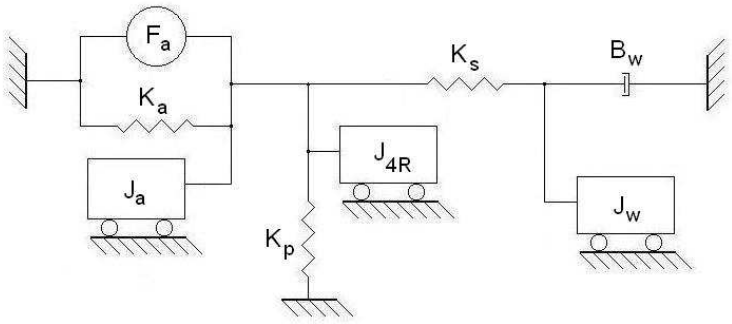

Figure 4.5: Mechanical model for a $1DOF$ MFI wing transmission system.

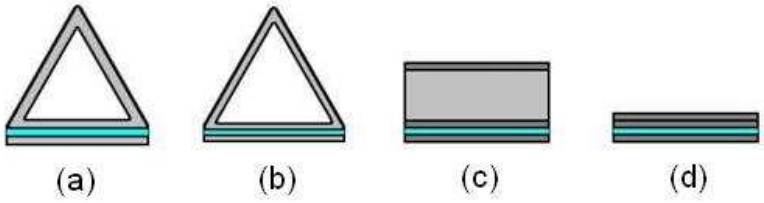

Figure 4.6: Cross sections of various link configurations. (a) $12.5\mu m$ folded steel, (b) $6.25\mu m$ folded steel, (c) carbon fiber honey comb, and (d) stacked carbon fiber sheets.

4.4.1 Link Design

The first goal of incorporating composite materials into the MFI thorax is to match the stiffness of the previous links while attempting to create links with a lower inertia and mass. Figure 4.6 shows example cross sections for the link design. To achieve a high stiffness-to-weight ratio, a honeycomb configuration was initially used as a substitute for the triangular beams with UHM prepreg as the face sheet and either laser micromachined carbon fiber or molded polyurethane as the core material. First, the stiffness of a honeycomb beam must be analyzed. To do this, an approximation for the product EI is introduced for a honeycomb structure assuming that the spacing layer contributes negligibly to the

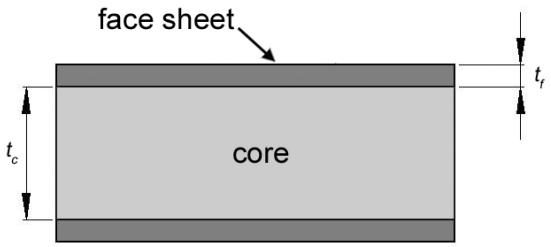

Figure 4.7: Drawing of honeycomb link.

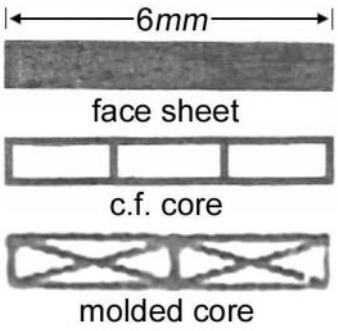

Figure 4.8: Face sheet and example cores for sample $6mm \times 1mm$ links.

beam stiffness. Figure 4.8 shows a face sheet, laser micromachined carbon fiber core, and a molded polyurethane core for a $6mm \times 1mm$ honeycomb link.

To estimate the EI term for honeycomb structures first note that since the beam is not homogeneous, this will have two terms:

$$EI = E'_f \left(I_f + nI_c\right) \tag{4.1}$$

where E'_f is the face sheet effective longitudinal modulus, I_f and I_c are the face sheet and core second moment of area respectively, and n is the ratio E_c/E'_f where E_c is the effective

longitudinal core modulus. Now, because of the parallel axis theorem:

$$EI = E'_f \left(\frac{wt_f^3}{6} + \frac{wt_f t_c^2}{2} + n\frac{wt_c^3}{12} \right) \tag{4.2}$$

Finally, for typical core and face sheet materials $n \approx 0$ and with $t_f << t_c$, the middle term in equation (4.2) dominates and the following approximation is made:

$$EI = E'_f \frac{wt_f t_c^2}{2} \tag{4.3}$$

4.4.2 Laminate Plate Theory for the Design of Flexure-Based Articulated Microstructures

Next an alternative to the honeycomb beams is described which entails layered composite sheets. Such an approach has the benefit of extremely simple construction. Again, since a layered approach is used to construct the links, laminate plate theory is used to describe the stresses and strains in the beam. In this instance, however, the stiffness-to-weight ratio is of the utmost importance. To determine the link stiffness, the equivalent quantity EI must be derived for a laminate consisting of any number layers in arbitrary orientations (however assumed to be symmetric about the mid-plane).

Similar to section 3.1.3, the interaction between the external moments per unit width and the strains and curvatures of the beam are given as follows:

$$[M_i] = [B_{ij}]\,\epsilon_j^0 + [D_{ij}]\,\kappa_j \tag{4.4}$$

The B_{ij} terms in equation (4.4) are extension-twisting coupling. The only instance in which these terms will be non-zero is if the laminate is asymmetric about its mid-plane. Thus this term can be ignored and to explore the effective EI, note that for a homogeneous beam

Table 4.4: Formulations for the various beam cross sections considered for the MFI links.

Morphology	Triangular	Honeycomb	Laminate
EI	$E\frac{\sqrt{3}}{96}\left(w^4-(w-t_s)^4\right)$	$\frac{E't_f t_c^2 w}{2}$	$D_{11}w$
mass	$3wlt_s\rho$	$wl\left(2t_f\rho_f+t_c\rho_c\right)$	$wl\sum_n t_i\rho_i$
$EI\left(mNm^2\right)$[1]	0.17 (s.s.) 0.17 (Si)	1.80	0.07
mass (mg) [1]	1.75 (s.s.) 0.52 (Si)	2.16[2]	1.08

[1]for a typical $6mm \times 1mm$ link

[2]for a core material with twice the mass of the face sheets

with a pure moment applied $M = EI\kappa$ where κ is the inverse of the radius of curvature. Equating this to equation (4.4) yields the following result:

$$[M_i] = [D_{ij}]\,\kappa_j = \frac{EI_{xx}}{w}\kappa_x \tag{4.5}$$

where w is the beam width which is used since the laminate plate formulation uses forces and moments per unit width. Thus, for a laminated beam, the equivalent EI_{xx} is given by $D_{11}w$. A summary of the three cross sections is given in Table 4.4.

From the data presented in Table 4.4 it can be seen that the stiffness-to-weight ratio for a stainless steel triangle beam is approximately the same as for a laminated carbon fiber beam. Using silicon as in [106] with the same dimensions increases this by nearly a factor of three while the carbon fiber honeycomb beam increases this by an additional factor of nearly three. What is not shown in this table is the relative difficulty in manufacturing each type of beam. Qualitatively, the most difficult and costly is the silicon triangle beam, followed by the steel triangle beam. The core molding and face sheet alignment necessary for the construction of the honeycomb beam causes this construction to be more difficult than that of the laminated beam. The laminated beam construction is stressed for its comparable performance to the former steel beam structures, but also for the remarkable

ease of construction and repeatability. Regardless of the complexity of the desired three dimensional structure, laminated carbon fiber links and joints can be created with a few hours of micromachining and a few hours of curing with a minimal amount of manual labor involved.

4.4.3 Joint Design

Since the size constraints of the MFI prevent the use of traditional pin and spherical joints used in larger scale robotic systems, such joints are simulated using flexure mechanisms. The important design criterion for such joints is to obtain low parallel stiffness while keeping as high a series stiffness as possible. To illustrate this point, a mechanical model of a $1DOF$ MFI wing transmission system is shown in Figure 4.5. If the parallel stiffness, denoted k_p of the transmission is increased to ∞ then the actuator sees an infinite stiffness and is blocked. Similarly, if the serial stiffness, denoted k_s is reduced to 0, there is an open circuit between the actuator and the wing. In either instance, no power is delivered to the wing. Thus, in conjunction with the links, the joints must be designed with these two quantities in mind.

The flexures in the MFI wing transmission system are created by sandwiching a compliant layer between two rigid layers of high modulus material. The flexure occurs where there is a gap in the rigid material and is shown in Figure 4.9. The key parameters in the design of the flexures are the geometric parameters of length, width, and thickness, as well as the modulus of the material used. It is important that the material be as thin and compliant as possible, however, as the thickness and modulus decrease, the buckling load decreases, which lowers the effective stress range of the flexure. The rotational parallel

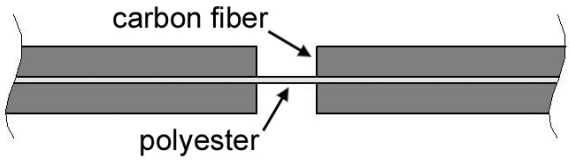

Figure 4.9: Laminated link and flexure layup.

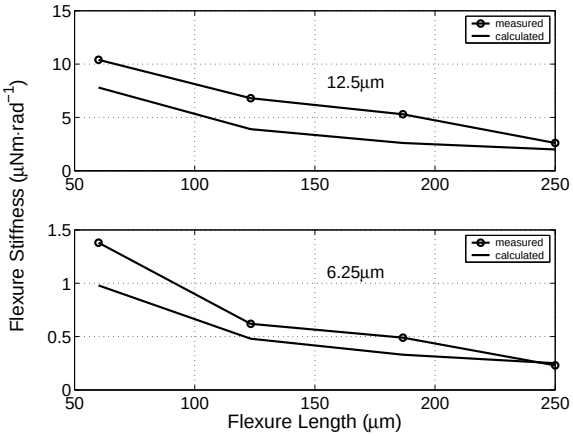

Figure 4.10: Flexure stiffness as a function of length.

stiffness of a flexure is (from [40]):

$$k_p = \frac{Ewt^3}{12l} \tag{4.6}$$

Polyester is used as the flexure material and films of $12.5\mu m$ and $6.25\mu m$ were obtained and equation (4.6) was tested for these two thicknesses. These results are shown in Figure 4.10.

The serial stiffness of a flexure is a nonlinear function of the axial load applied to the flexure. Below a certain stress point, the serial stiffness of the flexure is the stiffness seen by applying a load to a rectangular prism of the dimensions and material properties

of the flexure material. Above this point, which is the buckling point of the flexure, the beam experiences an unstable decrease in length for an applied axial load. Assuming that the flexure acts as a double clamped beam, the buckling load is given by the following [40]:

$$F_{cr} = \frac{\pi^2 EI}{4l^2} \tag{4.7}$$

The flexure buckles if the load is applied axially, which is true for the slider crank flexures at low displacement angles and for some of the links in the four bar. Note that it is possible that joints can be loaded transversely. Thus the serial stiffness for these flexures are not dependent upon the buckling of these beams, but the transverse displacement of the distal end of the flexure due to an applied load.

$$k_t = \frac{Ewt^3}{4l^3} \tag{4.8}$$

The four bar is constructed such that there is polar symmetry in the wing stroke. All joints are constructed such that at the neutral position, the flexures are flat. Thus any serial or parallel stiffnesses will be symmetric about the midstroke. For practical purposes, if the flexure buckles it no longer acts as a pin joint, thus the stiffness can be considered to be naught. Thus the serial stiffness of the flexure is given by:

$$k_s = \begin{cases} \frac{EA}{l} & F \text{ normal}, < F_{cr} \\ 0 & F \text{ normal}, > F_{cr} \\ \frac{Ewt^3}{4l^3} & F \text{ transverse} \end{cases} \tag{4.9}$$

Knowing what loads the flexures will see during operation will help to design the flexures so as to avoid buckling. From that point an optimization can be performed to obtain the highest possible serial stiffness for a desired parallel stiffness.

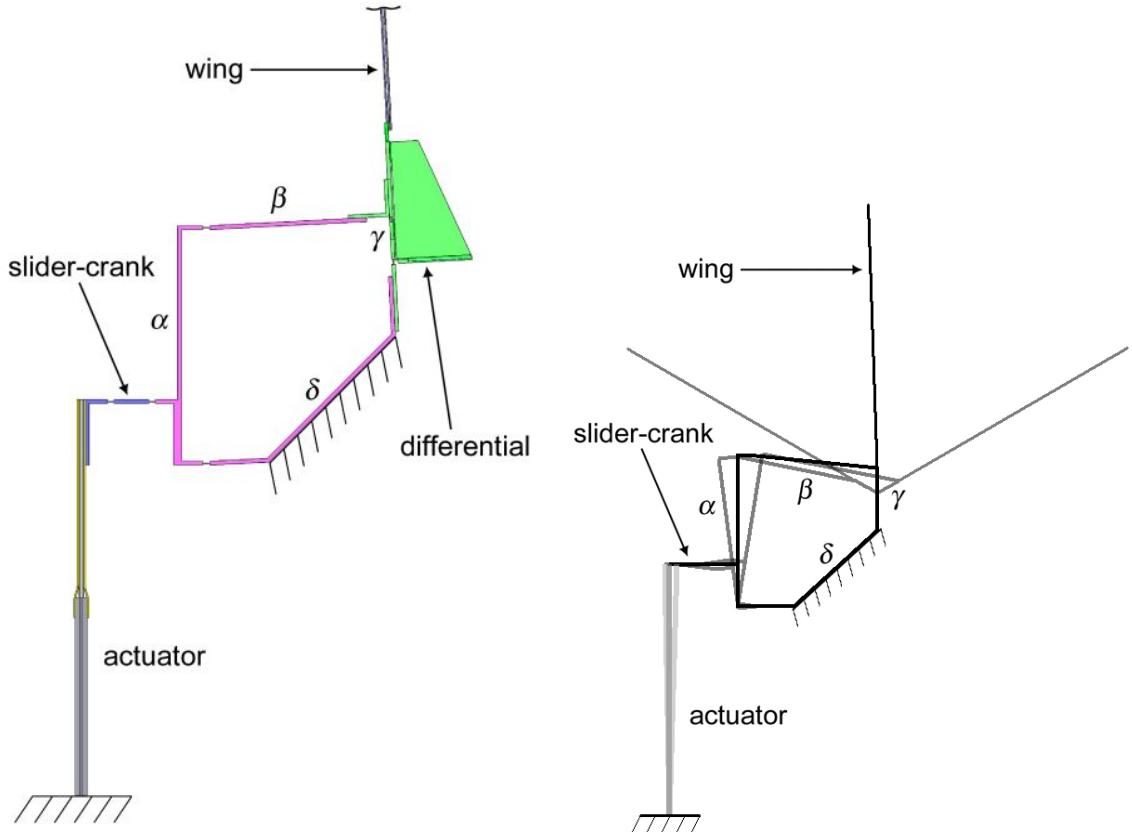

Figure 4.11: $1DOF$ section of the MFI actuator and thorax structure showing link and flexure detail (a) and kinematic detail (b).

4.4.4 Parallel Four Bar

To amplify and convert the small approximately linear motion of the actuator to a large angular deflection at the base of the wing hinge, a mechanical gearing system must be used. To accomplish this motion amplification, a parallel four bar mechanism is used. This structure consists of a four rigid links connected at rotational joints. This is shown along with the actuator in Figure 4.11.

To study the motion of the thorax it is first necessary to study the forward kinematics of the parallel four bar. The four bar consists of four links labeled respectively the

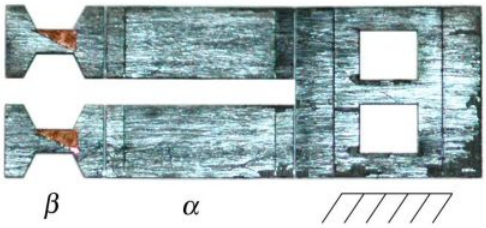

Figure 4.12: Planar view of four bars.

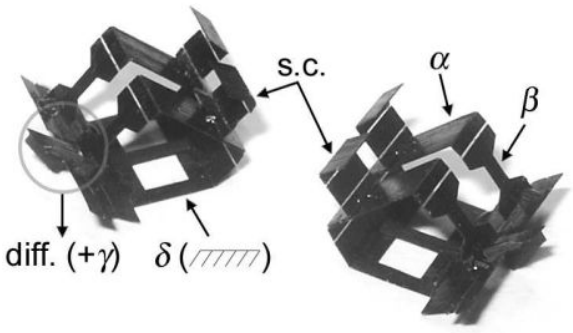

Figure 4.13: Completed 2DOF thorax containing slider cranks, four bars, and differential.

α, β, γ, and δ links. These are also referred to as the input, connector rod, output, and ground links. As a first order approximation, the four bar transmission ratio is the ratio of the input and the output links, $T = l_\alpha / l_\gamma$. Figure 4.12 shows constructed four bar before folding into the parallel mechanism. Note that the δ link is not shown. This is because it is included in the construction of the spherical five bar differential. Subsequent to connection to the differential (which will be discussed in section 4.4.6), the completed thorax is shown in Figure 4.13.

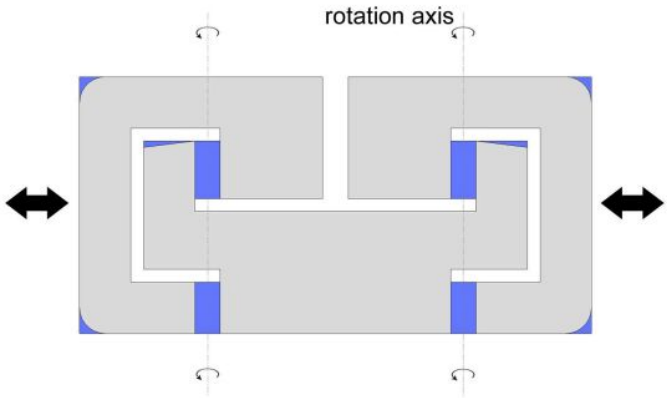

Figure 4.14: Drawing of the no buckling slider crank.

4.4.5 Slider Crank

To convert the approximately linear motion of the actuator tip to a rotation at the base of the α link, a slider-crank mechanism is used. The flexures of the slider-crank will not undergo large angular displacements, however the highest axial loads will be experienced by the these flexures. To compensate for this, one of two things can be done. First, the modulus and geometry of the flexures can be designed with the critical axial load in mind. Or, as is shown in Figure 4.14, a no-buckling slider crank can be constructed. In this embodiment, compressive or tensile axial loads cause one of the two adjacent flexures to be in tension. This was attempted with the previous folded steel process, but was ineffective due to the inability to create links stiff enough while maintaining the strict geometric requirements. For the completed no-buckling slider crank shown in Figure 4.15, a $[0/90]_s$ layup was used. The individual layers were laser micromachined and assembled into a silicone rubber mold along with the polyester flexure layer. To decide which of the two morphologies to use, it is important to note that the in line slider crank fails at the critical compressive normal

Figure 4.15: Completed no buckling slider crank.

load as defined in equation (4.7) while the no-buckling slider crank survives any tensile or compressive load up to the elastic limit of the flexure material. If small loads are expected ($F << F_{cr}$), then the no-buckling slider crank is unnecessary. However, buckling can be equated to a backlash element which will both decrease the power delivered to the load and cause uncontrollable regimes. For the case of the MFI actuators, the slider crank will see approximately $\pm 100mN$ of force and thus for a width of $3mm$, thickness of $12.5\mu m$, and length of $100\mu m$ this puts the slider crank flexures approximately an order of magnitude below the critical load.

4.4.6 Spherical Five Bar

Avadhanula et al. [4] described how to implement similar processes as described in section 4.4.3 to create another parallel mechanism, but in this case a spherical mechanism. Spherical parallel mechanisms have all joint axes aligned to a single point. Note that in Figure 4.16, θ_1 and θ_2 are the outputs of the individual four bars respectively and these two independent rotations are mapped to wing flapping and rotation about the Ψ axis.

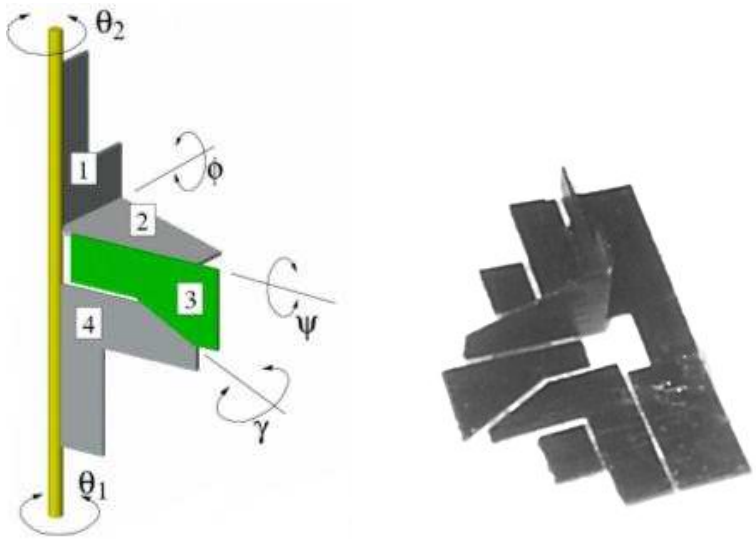

Figure 4.16: Conceptual drawing of the spherical five bar.

Thus this five bar is used as a differential mechanism. The kinematics and dynamics of this structure are not trivial and are discussed in detail in [3, 4], however it will be noted here that such a structure was attempted and determined to be infeasible using the previous stainless steel technique. To achieve the necessary degrees of freedom using folded steel links required two additional joints [103].

4.5 Rigid Composite Microstructures

As an antithesis to the articulated structures described in the previous section, certain aspects of the MFI need to be kept as rigid as possible. With the added constraint of being lightweight, this causes significant design and construction difficulties. Ideally, a rigid structure would contain thin high modulus beams oriented along the loading axes. The creation of rigid microstructures is discussed here with the two MFI examples of the

airframe and wing.

4.5.1 Exoskeleton

The exoskeleton or airframe for the MFI acts as a mechanical ground for the actuators and all links for the thorax. Certain flying insects utilize functional compliance of their pterothorax as an amplification mechanism. Since the MFI thorax is designed in order to achieve four independent degrees of freedom, such a structural compliance would be detrimental. Thus the airframe is designed with a more traditional engineering approach aimed at creating as stiff a structure as possible. The wing drive stiffness is dominated by the actuator stiffness, and as such the airframe will be judged by its stiffness relative to the actuator. The stiffness is not the only concern in the airframe design. The airframe geometry not only must align the thorax and actuators, but must do so in such a manner so as to align the center of mass and center of lift. This last point is crucial for any hope of stability since it was shown that very small changes in opposing wing kinematics in flying insects creates significant body torques, capable of producing enormous angular accelerations [37].

Calladine [10] gave an overview of the stiff and ultra-lightweight class of mechanical systems with tensional integrity called tensegrity structures. Such structures consist of beams (stiff in tension and compression) and reinforcing bars (stiff in tension) connected at joints. Joints of a tensegrity structure are defined as points where two or more beams (or bars) meet. No assumption is made about the joints, in fact they can be completely unconstrained. A remarkable relation is made between the sum of the beams and bars (b) and the total number of joints (j) which implies if the structure is stiff or not. For a

structure which is loaded with any combination of point loads at the joints, this is given by the following:

$$b \geq 3j - 6 \tag{4.10}$$

If this inequality is met then the structure is stiff, if not it will have specific infinitesimal degrees of freedom which will appear as compliances for this application. Note that this is for three dimensional structures; a similar result exists for two dimensional approximations. There are exceptions to this rule, but such exceptions generally are accompanied by states of prestress within the structure's beams and thus will not be discussed here.

Thus the design of a tensegrity structure entails that the inequality in equation (4.10) be met and that the loads are concentrated at the joints of the structure (where the γ link connects to ground). To test the validity of the tensegrity airframe, finite element analysis is performed by simulating loads upon the output section of the airframe shown in Figure 4.17. It is assumed that this area will see the largest inertial loads. For consistency, it is also assumed that the thorax links, as well as the actuator ground links coincide perfectly with joints of the airframe. To simplify this structure, it is assumed that the composite planks are rigid in tension and compression and the bars are only stiff in tension. A simplified drawing of the airframe is given in Figure 4.18. Note that two bars connecting two different sets of joints may intersect, but the intersection should not form another joint. Thus the number of joints in the airframe is 12 and thus to satisfy equation (4.10), the number of beams must be 30. The number of beams inherent in the structure for alignment and balancing reasons is 20, thus the number of reinforcing bars must be 10. To conveniently observe the change in airframe stiffness with the addition or subtraction

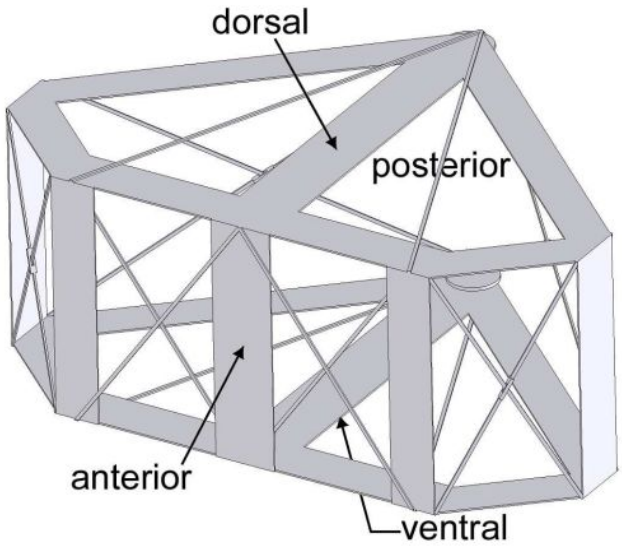

Figure 4.17: Drawing of the "diamond" airframe showing approximate beams and lines.

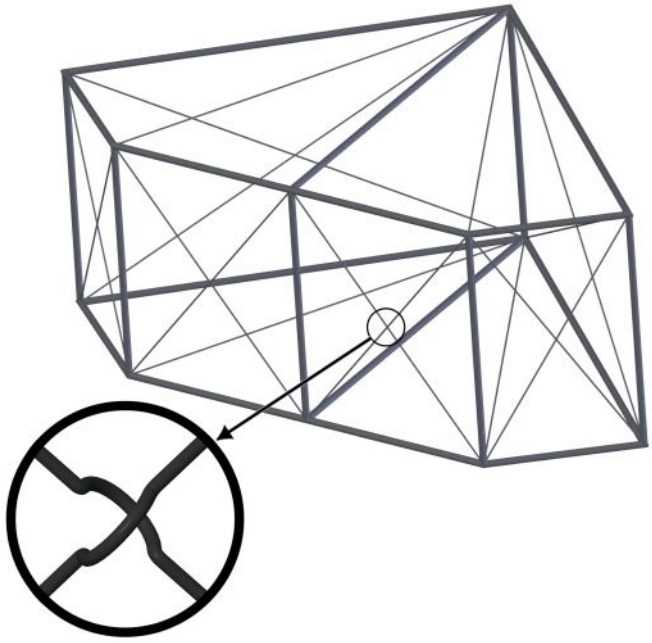

Figure 4.18: Beam and line drawing of the airframe with emphasis on bar independence (inset).

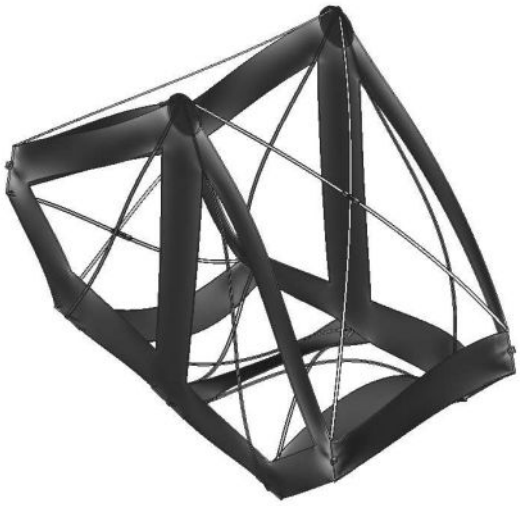

Figure 4.19: Example FEA deformation analysis from tangential loads. Note that the deformation scale is approximately 1:200,000.

of reinforcing bars, the finite element analysis is performed upon the airframe for various loading conditions. This is done while iteratively adding more reinforcing bars while keeping the loading conditions the same and observing the airframe deflections. The simulated loads are applied at the output joints with bilaterally opposed orientations in the lift (normal), drag (tangential), and radial directions. The relative airframe stiffness is determined by dividing these static loads by the maximum airframe deflection predicted by the FEA. The FEA software used was CosmosExpress, an addition to the SolidWorks CAD package. An example FEA output is shown in Figure 4.19. The results of this simulation are shown in Figure 4.20 and do show a drastic increase in airframe stiffness above a specific number of reinforcing bars. Note however that this jump occurs after 30 bars are connected. This offset is explained by the fact that the anterior face of the airframe has six coplanar joints causing the five beams and bars connecting them to be redundant. Thus an additional five

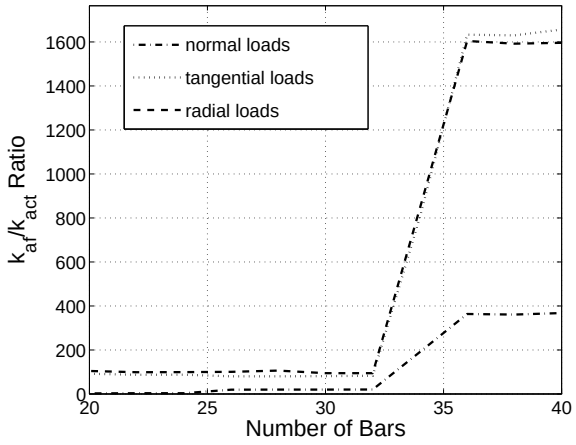

Figure 4.20: Airframe stiffness relative to the nominal actuator stiffness.

reinforcing bars are required to create an airframe which is simply stiff. The construction of the airframe is similar to that of the links of the thorax. First, unidirectional UHM prepregs are laser micromachined into the shapes of the beams. Since the beams lie on three planes (dorsal, anterior, and ventral), the cut prepreg beams are layed out coplanar with joints placed on the intersections of the dorsal and anterior planes and the ventral and anterior planes. This is shown in Figure 4.21. This assembly is then cured, folded into shape and the joints are frozen at right angles. At this point, the actuators are connected to the airframe.

Since the thorax has a large transmission ratio, the largest forces and moments will be experienced by the actuators. Note that in the drawing of the airframe (Figure 4.17) the actuators are not shown and there is an empty space in the posterior. For the case of the airframe tensegrity structure, the actuator mount is assumed to be another rigid beam connected at the posterior connecting the dorsal and ventral airframe faces. Thus the

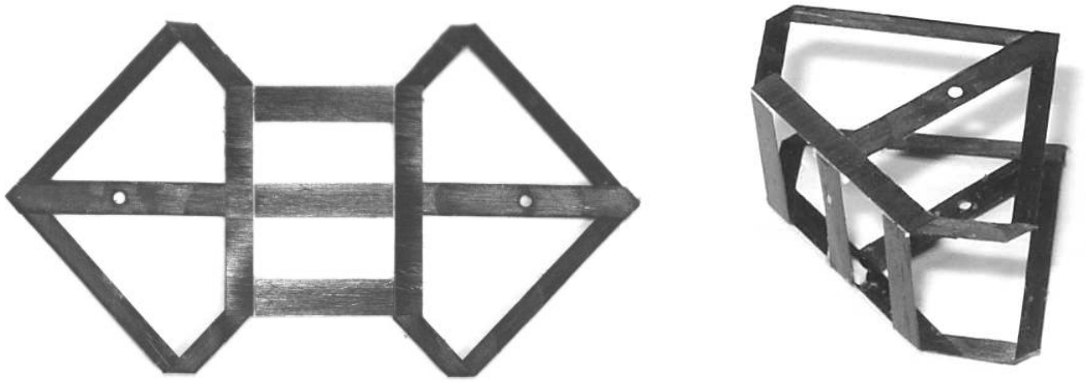

Figure 4.21: Completed airframe previous to folding into shape (a) and folded (b).

remaining question is how to mount the actuators to a beam which is stiff to both point loads and moments. To accomplish this, the actuators are embedded in a mold in which glass reinforced polyurethane is injected. This creates a short fiber composite cylindrical beam which is rigid to torques and loads. To estimate the torsional stiffness of the beam, first it is necessary to estimate the short fiber composite modulus. As a first order approximation, the new material is assumed to be isotropic with a modulus defined in [46]:

$$E' = \frac{3}{8}E_L + \frac{5}{8}E_T \tag{4.11}$$

where E' is the equivalent modulus and E_L and E_T are the longitudinal and transverse moduli of an aligned short fiber composite with identical constituent relations to the short fiber composite in question. These two quantities are defined as follows:

$$\begin{aligned} E_L &= E_m \frac{1+\left(2l_f/d_f\right)\eta_L V_f}{1-\eta_L V_f} \\ E_T &= E_m \frac{1+2\eta_T V_f}{1-2\eta_T V_f} \end{aligned} \tag{4.12}$$

where E_m is the matrix modulus, V_f is the fiber volume fraction, l_f is the fiber length, d_f

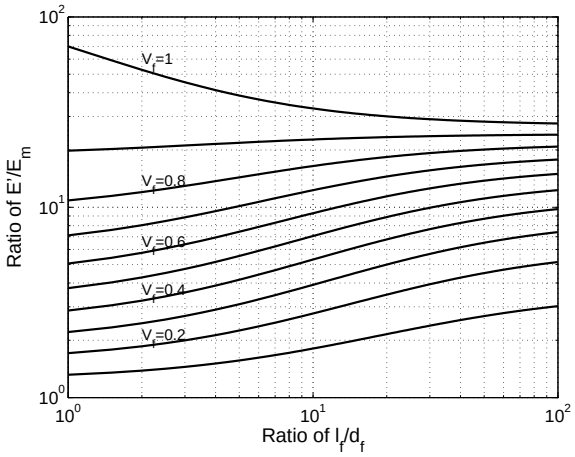

Figure 4.22: Short fiber composite modulus for changes in volume fraction and fiber length

is the fiber diameter, and the coefficients of mutual influence are defined as:

$$\eta_L = \frac{\frac{E_f}{E_m} - 1}{\frac{E_f}{E_m} + (2l_f/d_f)}, \qquad \eta_T = \frac{\frac{E_f}{E_m} - 1}{\frac{E_f}{E_m} + 2} \tag{4.13}$$

where E_f is the fiber modulus. The effect of the volume fraction and the fiber length on the effective modulus are shown in Figure 4.22 for glass reinforced polyurethane. Finally, the torsional stiffness of this cylindrical beam is calculated.

$$k_\theta = \frac{G' I_b}{l_b} \tag{4.14}$$

where l_b is the beam length, G' is the effective shear modulus defined to be:

$$G' = \frac{E'}{2\left(1 + \nu'\right)} \tag{4.15}$$

where ν' is the effective Poisson's Ratio defined by the rule of mixtures as $\nu' = V_f \nu_f + \left(1 - V_f\right) \nu_m$ and I_b is the polar second moment of area:

$$I_b = \frac{\pi}{2} r^4 \tag{4.16}$$

Table 4.5: Engineering parameters for short fiber composite (SFC) actuator mount.

parameter	E_f	E_m	ν_f	ν_m	ρ_f	ρ_m	l_f	d_f	r	l_b	V_f
value	70	1	0.33	0.27	1500	1200	70	10	1.5	1	0.4
unit	GPa	GPa	—	—	kgm^{-3}	kgm^{-3}	μm	μm	mm	mm	—

SFC parameters	E'	k_θ	m_{am}
value	6.2	19	10
unit	GPa	$Nm \cdot rad^{-1}$	mg

where r is the beam radius. To determine the worst-case torque that will be applied upon the cylinder, consider the maximum inertial load on the tip of the actuator for a thorax with a Q of 2. For a maximum deliverable actuator force of $50mN$, this gives $100mN$ on the tip of the $10mm$ long actuator for $1Nmm$ of torque. For two bilaterally symmetric actuators, any load applied to the tip of one actuator will result in an angular displacement of the other, creating undesirable thorax motions. Thus, an acceptable coupling needs to be established for the undesirable motion excited from neighboring actuators. For a wing stroke of 120°, a 1% coupling will give approximately 1°($17.5mrad$) of acceptable undesired wing stroke. Thus the acceptable stiffness for the actuator mount beam is $57Nmm \cdot rad^{-1}$. The matrix material is a castable polyurethane and the reinforcing fibers are milled E-glass. The effective modulus, and thus the beam stiffness increase monotonically with the volume fraction. The greatest practical volume fraction before the catalyzed resin became too difficult to inject was empirically found to be approximately 0.5. Calculating the effective modulus and using a combination of equations (4.14) through (4.16) yields the predicted actuator mount stiffness. This, along with the constituent material parameters is given in Table 4.5. The actuators were connected to the mount via a two part silicone rubber mold

Figure 4.23: Detail of actuator mount for use in the airframe.

in which the actuators are held in place by the top half. The reinforced catalyzed epoxy is injected into either of the open ends of the mold to form the cylinder. The resulting structure is shown in Figure 4.23. Finally, the actuator electrodes are connected via $25\mu m$ insulated wires. This is done so as to minimize any interference the wires could induce upon the body dynamics.

4.5.2 Wing

Another rigid structure created with the same process is the wing. Insect wings consist of reinforcing bars running from the wing base to the tip typically along the longitudinal direction separated by thin membranes [13]. These reinforcing bars are hollow tubes created by veins. Although the morphology of the wings varies immensely from species to species [30], certain characteristics are common. The stiffness of insect wings is typically anisotropic with respect to the longitudinal and chordwise directions. This is due mostly to the orientation of the venal structure and the concentration of veins toward the leading edge in many insects. It has been suggested that insect wing compliances play an important role in lift production [30]. Wings with anisotropic stiffnesses for example can change direction of camber from one half stroke to the next.

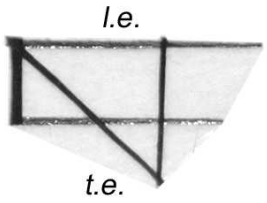

Figure 4.24: Carbon fiber wing (spar layout courtesy of A. Bachrach).

Similar to the insect wings, the MFI wings are created with discrete reinforcements. Previous to the introduction of the carbon fiber process, the wings were reinforced with polyimide tubes very similar to insect wings. The current MFI wings are created by unidirectional carbon fiber planks cured to a polymer face sheet. Since it is difficult to quantify the aerodynamic advantage of insect wing compliance, the MFI wings are designed to create as rigid a structure as possible. Along with the stiffness properties of the wing, the inertial matching plays a crucial role in the overall dynamics [3]. The latest version of the carbon fiber spar reinforced MFI wing is shown in Figure 4.24. This wing has the same second moment of area as a typical *Calliphora* with similar stiffnesses and half the inertia as is shown in Table 4.6.

4.6 Results

By understanding the construction difficulties described in section 4.3, the thorax was created utilizing the high modulus and low density of composite materials. This process involves laser micromachining feature sizes on the order of the fiber diameter and thus represents the smallest possible use of these materials. Since all critical alignment is done

under the laser and kept constant through the curing process, this step typically does not introduce errors which could effect the system dynamics. In addition to creating a lighter transmission system, the overall dynamics of the system are improved in several ways. First, serial compliances are minimized through use of geometric constraints and/or reduction of flexure peeling. Second, the system resonant frequency is increased via the lower serial compliance and the decreased link inertias. Finally, serial compliance reduction removes spurious modes within the structure dynamics. In addition to the performance benefits, the ease and rapidity of this manufacturing process causes the prototyping time to reduce from approximately one week to one day. The repeatability of the thorax performance is inherently enhanced for this process with respect to the steel process. The reasons for this are two-fold. First, the elimination of peeling and the lack of manual allignment creates flexures which are very uniform throughout a structure and from one version to the next. Also, since no epoxies are required in the layup, there is no chance of epoxies flowing into the flexures during construction. A final benefit to the composite process is an increased lifetime compared to the previous steel structures.

Table 4.6 shows the parameters for the MFI thorax in comparison to the previous steel triangle version.

Table 4.6: Design joint parameters for each member of the MFI thorax.

Parameter	Steel Triangle	CF Laminate	Units
link stiff.	38	20	kNm^{-1}
link mass	2.3	1.5	mg
4bar k_p	120	100	Nm^{-1}
4bar k_s	140	$> 1 \times 10^3$	Nm^{-1}
4bar inertia	20	5	$mg \cdot mm^2$
wing inertia[1]	20	10	$mg \cdot mm^2$
airframe mass	30	15	mg
Q	3.5	1.8	—
f_0	120	200	Hz
const. time	7	1	$days$
life time[1]	1	10	hrs

[1]previous wings with polyimide tubing reinforcements

[2]for continuous actuation

Part III

A Biomimetic Sensor Suite

Chapter 5

Biologically Inspired Attitude Sensing

Though limited in neural processing power, insects have the ability to effectively and efficiently traverse their environments. To examine this further, insect sensory perception was investigated [71, 72, 59, 60]. What is clear is that flying insects use a number of both photo- and mechano- receptive devices to obtain information about their environment. The photo-receptor based sensors (compound eyes and ocelli) lack a high spatial resolution but have a very high temporal resolution. The combination of these two sensors gives readings of optical flow for obstacle avoidance and angular and linear velocity estimation, and horizon detection respectively. In conjunction with vision based sensing, many two-winged flying insects have developed gyroscopes called halteres. These halteres consist of two non-coplanar vibrating cantilevers driven at the wing beat frequency which are able to sense coriolis forces. Through an ingenious demodulation scheme, insects are able to es-

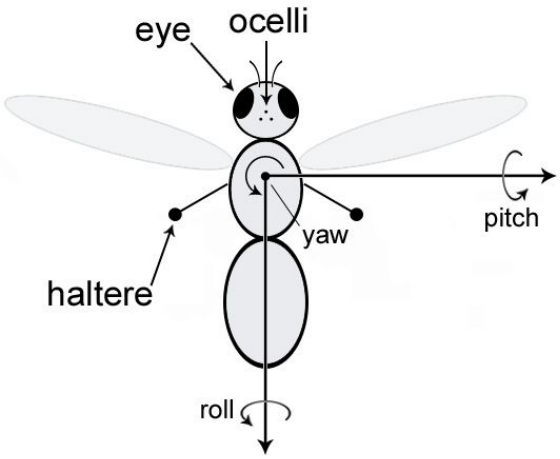

Figure 5.1: Sensor diagram for the blowfly *Calliphora*.

timate their roll, pitch, and yaw angular velocities with an extremely high dynamic range. A simplified diagram of these three sensor morphologies is shown in Figure 5.1.

Insects use a hierarchical sensory system which is broken into various levels of control [72]. For example, forward flight may use the compound eye to measure optic flow and the ocelli to sense attitude. When an object appears in the image plane high optic flow is measured. When this optic flow exceeds a threshold, a saccade is triggered. During the saccade, the haltere is used to sense angular velocity until forward flight is resumed. An example of this control strategy is shown in Figure 5.2.

These three sensors (optic flow, ocelli, and haltere) have all been created using similar rapid prototyping construction techniques as for the thorax of the MFI (both the previous stainless steel micro-origami and composite structures described in chapter 4). This chapter serves as both example applications and a verification of the microactuators and microstructures described in chapter 3 and 4.

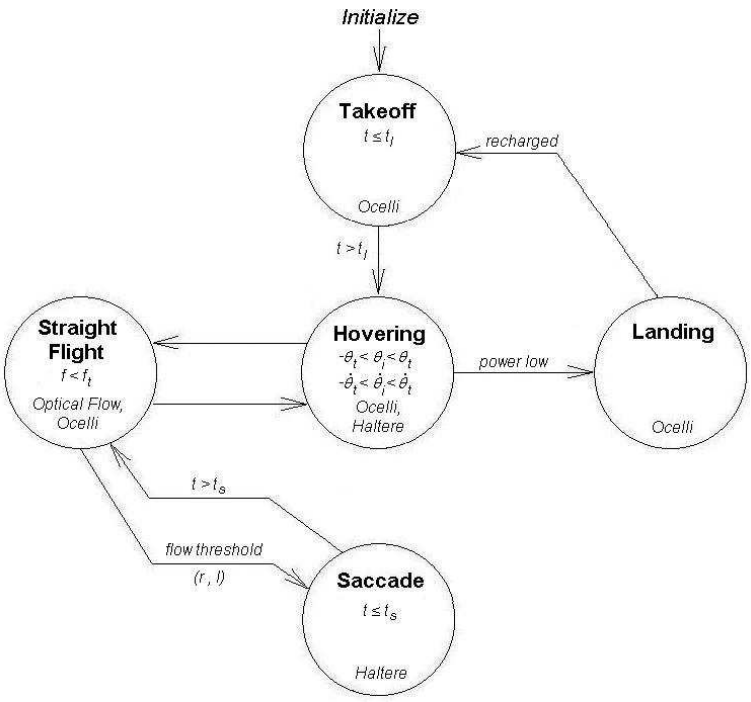

Figure 5.2: Hybrid control strategy for a MAV.

5.1 Mechanoreceptor-based

Insects can generally measure local strains in a binary nature using mechanoreceptors called campaniform sensilla. These structures have a ball-and-socket type morphology which is bistable in nature. When enough stress is applied to the campaniform sensilla, the 'ball' changes states and triggers a neural impulse. Thus an individual sensilla cannot accurately measure a range of stresses, however multiple sensillae in the same region can be used to give accurate responses to local stresses.

Analogous to the sensilla in insect appendages, strain gages are used as the fundamental sensing element for the mechanoreceptor-based sensors. However, unlike the sensilla

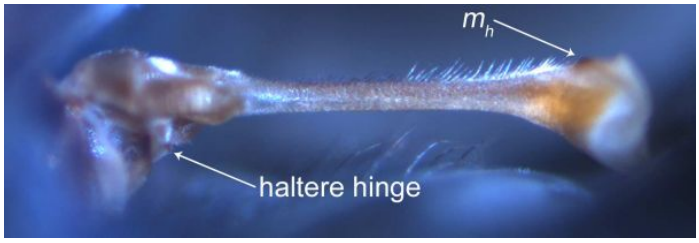

Figure 5.3: Haltere of a *Calliphora*.

these gages have a linear response over a large range of strains.

5.1.1 Halteres

Certain two-winged insects, for example the flies of order *Diptera*, have evolved from an initial four-wing configuration by a reduction of the hind wings. Instead of having aerodynamic significance, the reduced hind wings are used as sensors to detect body angular velocities in three dimensions [59, 60]. This is done through measurement of the coriolis force. The halteres are analogous to a ball at the end of a thin rod which beat anti-phase to the wings at the wing beat frequency. In fact, because of the evolutionary development of this sensor, the same musculature that drives the wings (indirect flight muscles) also drives the halteres along with a set of kinematic tuning muscles (direct flight muscles) [30]. Figure 5.3 shows a haltere of the blowfly *Calliphora*. Because of the motion of the haltere, there is a complex force acting on the mass at the distal end. This force is given by the following:

$$F_h = m_h g - m_h a_h - m_h \dot{\omega} \times r - m_h \omega \times (\omega \times r) - 2 m_h \omega \times v_h \tag{5.1}$$

where m_h, g, a_h, ω, r, and v_h are the haltere mass, acceleration due to gravity, instantaneous haltere acceleration, body angular velocity, haltere length, and instantaneous haltere

velocity respectively. The first term in (5.1) is the gravitational force and is small compared to the coriolis force. The second is the haltere inertial force which is in the radial and tangential directions. The third term represents the inertial force due to body angular acceleration. This is again mostly in the radial and tangential directions. The fourth term is the centrifugal force and acts in the radial direction. The last term is the coriolis force which contains information about the magnitude of the body angular velocity. This force acts in the lateral direction and is thus decoupled from the other terms. Therefore, a recreation of the haltere should be able to sense the forces in the lateral direction, but be impervious to those in the radial and tangential directions.

Note that the coriolis force term depends upon the instantaneous velocity and mass of the haltere. For a given body angular velocity, this force should be maximized so as to achieve the greatest sensitivity in the measurement. Thus, m_h and v_h should be as large as possible. The mechanical haltere structure is designed similarly to the wing drive transmission system of the thorax. The only difference is that only 1DOF is necessary, thus the differential is eliminated and in place of the five bar and wing is replaced by the haltere. This is shown conceptually in Figure 5.4.

Using the same 1DOF thorax as for the MFI, the haltere is designed to have a stroke amplitude of $A_h = \pm 60^\circ$ at $f_0 = 200Hz$. Assuming that the haltere mass describes an arc, the velocity is given as follows:

$$v_h = 4A_h r f_0 \cos(2\pi f_0 t) \tag{5.2}$$

To obtain the same resonant frequency as the MFI wing beat, the haltere inertia ($J_h = m_h r^2$) is set to half the wing inertia (since a single four bar will have half the parallel

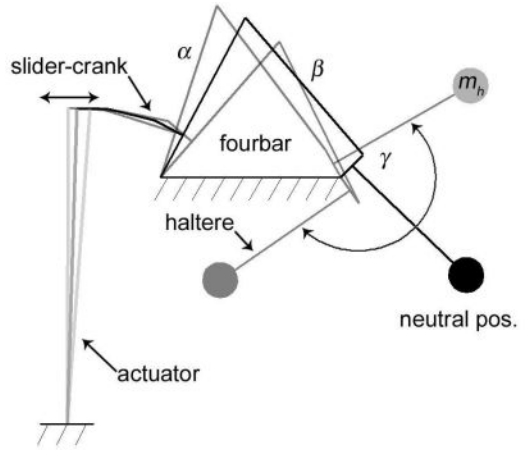

Figure 5.4: Haltere functional drawing.

stiffness as the dual four bar in the 2DOF thorax).

To achieve maximum sensitivity to lateral loads while being insensitive to tangential and radial forces, the haltere rod is a flat plate with thickness t_h and width w_h. The strain gages used are semiconductor resistors which change resistance when a strain is seen. Two gages are bonded to the proximal end of the haltere on opposite faces of the beam in a half bridge configuration. This half bridge signal is amplified with a Techkor 9000s strain gage signal conditioner. Empirically, the minimum strain readable by this setup is found to be approximately 1×10^{-6}. The strain from a lateral force F_c is given by the following:

$$\epsilon_h = \frac{F_c t_h r}{2EI} \tag{5.3}$$

Thus, the combinations of equations (5.1), (5.2), (5.3) and the haltere inertia leave the four unknowns of r, m_h, t_h, and w_h. Solving these with the known parameters of A_h, f_0, EI, J, and ϵ_{min} completes the analysis and allows the remaining variable, ω to be set based upon expected angular velocities.

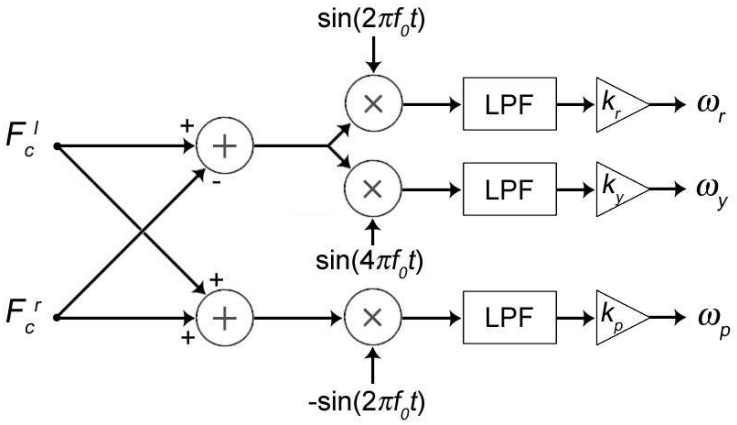

Figure 5.5: Demodulation scheme for bilaterally symmetric halteres.

A *Calliphora* has only two halteres, yet it can measure all three body angular velocities [59]. This is due to geometry and an ingenious demodulation scheme based upon the relative temporal properties of the roll, pitch, and yaw force modulation on the haltere mass. To the haltere, left and right roll induced coriolis forces are seen 180° out of phase with each other at the beat frequency. Left and right pitch induced forces are in phase at the beat frequency. Yaw angular velocities cause the left and right forces to be 180° out of phase at twice the haltere beat frequency [101, 59]. Thus the demodulation scheme shown in Figure 5.5 is proposed.

The haltere is constructed by laser micromachining a stainless steel sheet to the required dimensions and depositing metal to the distal end to create the mass. Next, the strain gages are attached (as close to the proximal end as possible) and connected using insulated $25\mu m$ ribbon cable. The completed haltere is then attached to the transmission system and is shown in Figure 5.6. To test this haltere it was placed on a damped harmonic oscillator to simulate a pitch orientation. Note that only one haltere was tested and thus

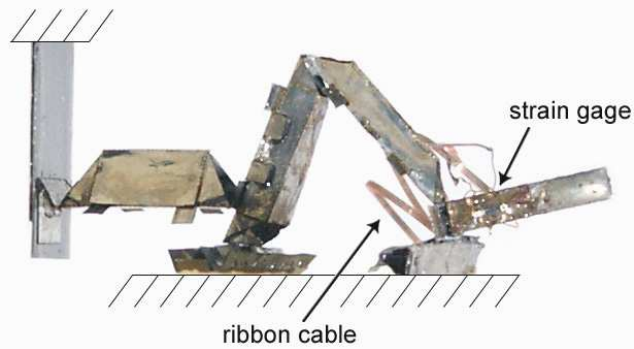

Figure 5.6: Completed single haltere.

only pitch angular velocities can be sensed. The angular position of the harmonic oscillator was sensed with a high speed video camera that was triggered with a computer to begin recording exactly when the haltere signal began to be recorded. This video sequence was then processed off line and, using a Hough transform, the angular displacement of the system was determined for each frame. This was then differentiated to yield the actual pitch angular velocity. The haltere signal was demodulated as with the pitch signal in Figure 5.5. The haltere beat frequency and phase are known via actuator displacement measurements (see [97]). The gains on the outputs are proportional to $1/m_h$. Finally this estimated pitch angular velocity was low pass filtered to remove any remnant of the drive signal, compared to the actual angular velocity and is shown in Figure 5.7.

The creation of a gyroscope is not terribly impressive, however the halteres have a few features which make them more appropriate for the MFI than existing commercial off the shelf gyroscopes. Table 5.1 compares the haltere performance with that of existing gyroscopes.

Thus the haltere has the benefits of low power, light weight, and high dynamic

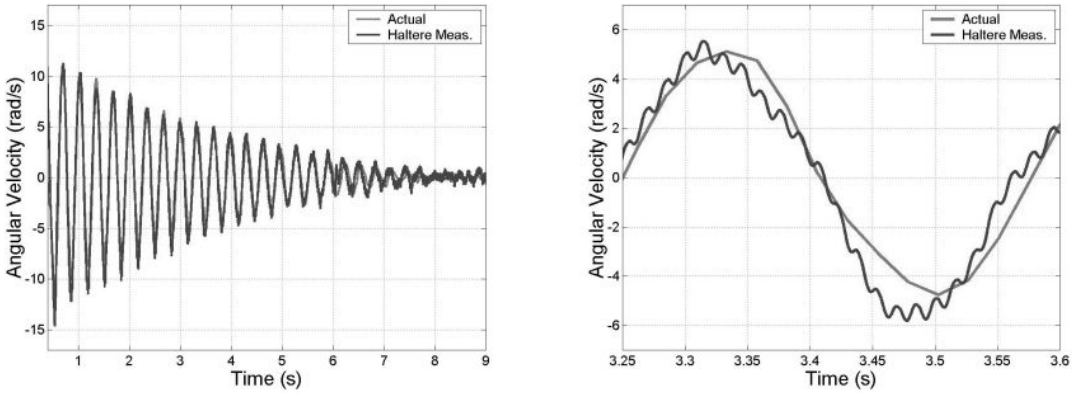

Figure 5.7: Results of pitch test for single haltere (a) and zoomed in to show accuracy (b).

range with respect to COTS gyros. The first two are obvious benefits, however a high dynamic range is also necessary since during saccades the insect will see angular velocities in excess of $1000°s^{-1}$. Note also it is assumed that when integrated to the MFI airframe the actuator will not be necessary since small body vibrations should be sufficient to excite this high Q system.

5.2 Photoreceptor-based

Photoreceptor-based sensors are analogous to either the compound eye or light sensitive areas of insects. Two large patches containing an array of individual photoreceptors are very distinct upon the head of insects. These photoreceptors have fixed lenses and give a pixelated view of the world to the fly, however they have the benefits of yielding relatively simple images to process and a very high temporal bandwidth.

Much more discrete: dorsally between the compound eyes lie three small photoreceptors collectively called the ocelli. Each individual ocellus senses light levels from one

Table 5.1: Comparison of haltere performance to available MEMs angular rate sensors.

	Mass (mg)	Sensitivity ($mV/(^\circ s^{-1})$)	Max Rate ($^\circ s^{-1}$)	BW (Hz)	Power (mW)
Haltere [1]	30 [5]	0.1	$\pm$300000	15	1
ADRXS300 [2]	< 500 [6]	5.0	$\pm$300	40	30
KGF01-1002 [3]	< 600 [7]	8.0	$\pm$250	75	125
MicroRing Gyro. [4]	< 600 [7]	25.0	$\pm$60	10	75

[1] Assuming parasitic drive and 1% duty cycle strain gauge sampling.

[2] Analog Devices, Inc., http://www.analog.com/

[3] Kionix, Inc., http://www.kionix.com/

[4] MicroSensors, Inc., http://www.microsensors.com/

[5] Including the weight of the four bar structure.

[6] Including the weight of the BGA surface-mount package ($7mm \times 7mm \times 3mm$).

[7] Including the weight of the 24-pin SOIC package ($7.52mm \times 15.36mm \times 2.35mm$).

area of the sky sphere. Thus together the ocelli can form an estimate of where the light is most intense. In outdoor daylight regimes, this is an excellent estimate of where the horizon is with respect to the insect body frame.

To recreate these sensors, custom made photodiodes are used as the photoreceptors. These photodiodes are shown in Figure 5.8 and have a mass of approximately $1mg$.

5.2.1 Ocelli

The visual system of flying insects is primarily dependent upon the compound eye which lacks the ability to adjust focal length, but has an array of discrete elements which are conducive to measurements of the image velocity. However, it has been shown that insects also use their ocelli for crude estimations of body attitude [71]. Under the influence of the ocelli, insects tend to try to align themselves to the horizon. The photoreceptors of the ocelli are lensed but defocused [71] and situated one anterior and two laterally and

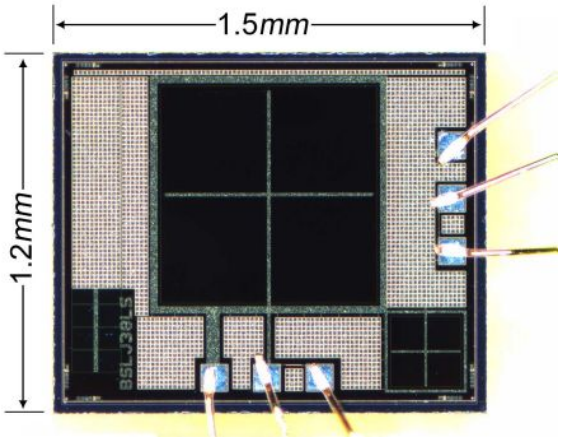

Figure 5.8: Custom photodiode for use in photoreceptor-based biomimetic sensors.

dorsally from the first as is shown in Figure 5.9. Since an ocellus is defocused, each gives a spatial low pass filtered view of the sky sphere. This is significant since this separates these sensors functionally from the compound eye. It is hypothesized that the insect estimates the position of the horizon by pairwise subtraction of the three ocellus signals. To recreate this, four photodiodes are used to create two uncoupled angular measurements. Initially, on a test fixture, the optimal angle between opposing ocelli is determined experimentally to be approximately 40°. A millimeter scale circuit board is then created by laser micromachining $5\mu m$ thick copper traces onto an electrically insulated trapezoidal shaped carbon fiber layer. Four of these trapezoidal layers are joined with flexures and the four photodiodes are populated to the four appropriate areas. All that is needed additionally are four resistors to put in parallel with the photodiodes to generate a readable output voltage which is included in the photodiode in Figure 5.8. A completed ocelli is shown in Figure 5.10. As in [100], it is assumed that pairwise subtraction of opposing ocelli signals will give a

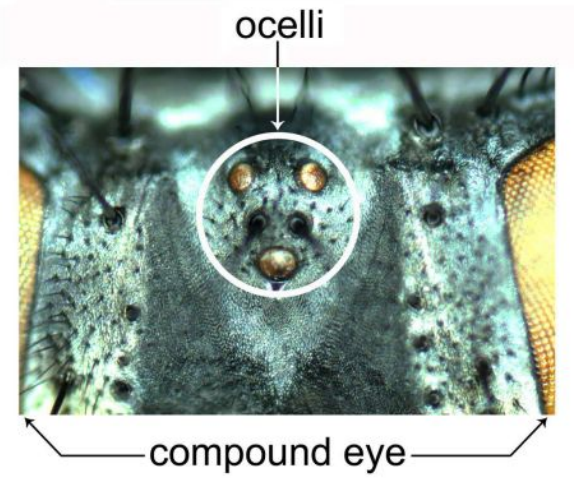

Figure 5.9: Ocelli of the blowfly *Calliphora*

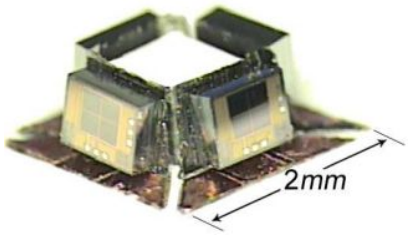

Figure 5.10: Completed $12mg$ ocelli.

monotonic correlation of the body angles to the horizon. This is only true if the light intensity in question is a monotonically decreasing function of latitude. This was verified for various indoor and outdoor conditions as described in [100]. The setup to verify the ocelli performance is shown in Figure 5.11. The ocelli was tested for angular orientations in one dimension and assumed that since the two axis of sensing in this ocelli are decoupled the results can be extrapolated to the full two axes. The ocelli was rotated around one axis while a light source was fixed above. The individual ocellus signals were measured as

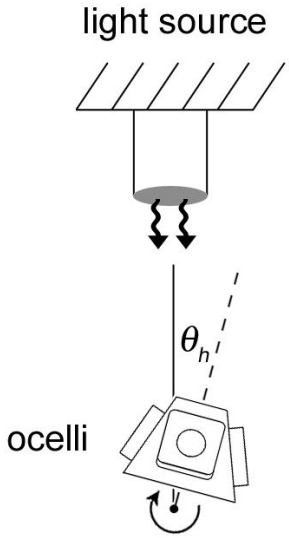

Figure 5.11: Setup for ocelli verification.

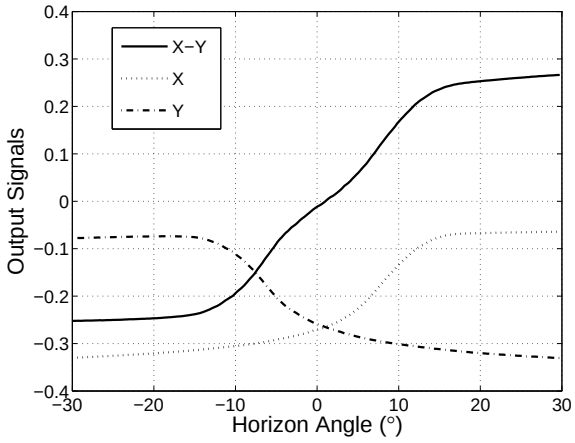

Figure 5.12: Individual ocellus output and resulting ocelli response to simulated horizon angular motion.

a function of the angle and subtracted to give the output as is shown in Figure 5.12.

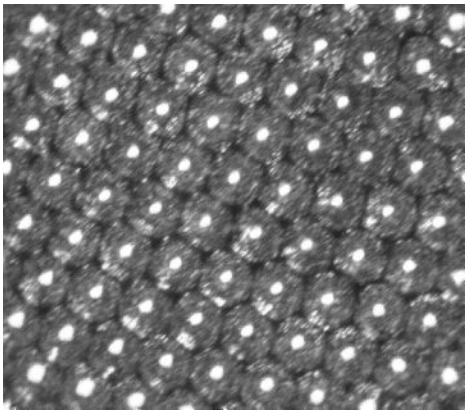

Figure 5.13: Section of the compound eye.

5.2.2 Optic Flow

The compound eye of insects consists of thousands of lensed photoreceptors arranged in a course array. This gives the insect a mosaic view of its environment which has a poor representation of static detail, but the discrete nature of the photoreceptors yields an excellent response to motion. An image of a section of the compound eye of the blowfly *Calliphora* is shown in Figure 5.13. The individual lensed photoreceptors in this image are approximately $20\mu m$ to $25\mu m$ in diameter. It is hypothesized that the compound eye is able to view motion by using the individual photoreceptors in a two dimensional elementary motion detector. An elementary motion detector gives a measure of optic flow, or how an image moves on the visual plane. This is accomplished by comparing adjacent photoreceptor values to give localized vector fields for each part of the image plane. A diagram of an elementary motion detector is shown in Figure 5.14. The photoreceptor values are correlated with the delayed (the low pass filters in Figure 5.14) values from the adjacent photoreceptors. These are then subtracted to give a magnitude and direction of optic flow.

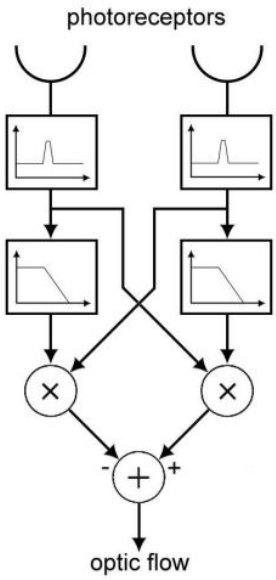

Figure 5.14: Elementary motion detector.

The realization of a physical optic flow sensor is similar to that in [8] on a simpler scale. Such optic flow sensors give very accurate measurements of the velocity of numerous objects in the image plane, however what is desired for this application is a sensor for use in obstacle avoidance. For example, a simple heuristic control for the MFI could use the magnitude of the measured optic flow to initiate saccades. When the raw optic flow number exceeds some predetermined value, this indicates that an object is near and the insect must turn. Thus, a minimal number of photoreceptors is used in the realization of the MFI optic flow sensor. Figure 5.15 shows a two by two photodiode array created for use on the MFI.

To test this sensor, a simulated obstacle was passed in front of the photodiodes. This simulated obstacle consisted of a black stripe on a white background as is shown in Figure 5.16. The photodiode values were recorded and processed off line using the elementary motion detector architecture from Figure 5.14. The results show an excellent

Figure 5.15: Prototype optic flow sensor for MFI obstacle avoidance.

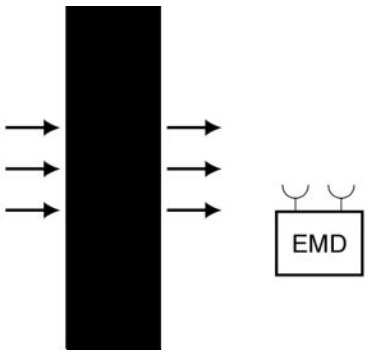

Figure 5.16: Moving stripe test setup for optic flow sensor.

response to the simulated obstacle as is displayed in Figure 5.17.

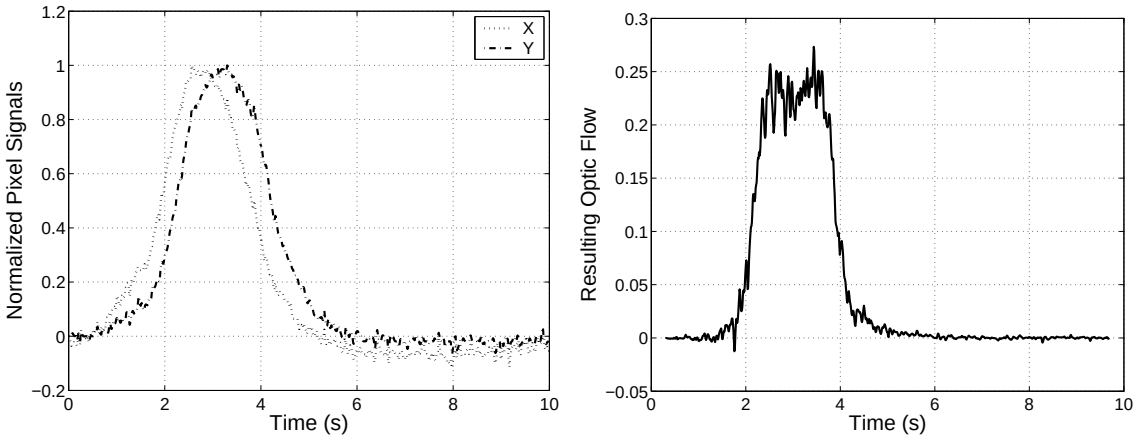

Figure 5.17: X and Y photodiode signals (a) with resulting optic flow measurement (b).

Part IV

Conclusion and Appendices

Chapter 6

Conclusion

This work describes the development of the components necessary for the realization of a flying robotic insect on the scale of and with the functionality of a *Calliphora*. A number of enabling technologies are created such as the high power density actuators described in chapter 3 and composite microstructures described in chapter 4. From these two enabling technologies, a number of example applications are presented such as parallel and spherical serial mechanisms (4.4.4 and 4.4.6), rigid microstructures (4.5.1), and attitude sensors (5).

6.1 Integration

The MFI integration involves mounting all components to the airframe. Since the thorax and actuators are inherently aligned, this step does not involve precision placement. However, each component must be mounted to the airframe at the airframe joints as rigidly as possible. Another aspect of this process is modularity. The completed MFI contains 30

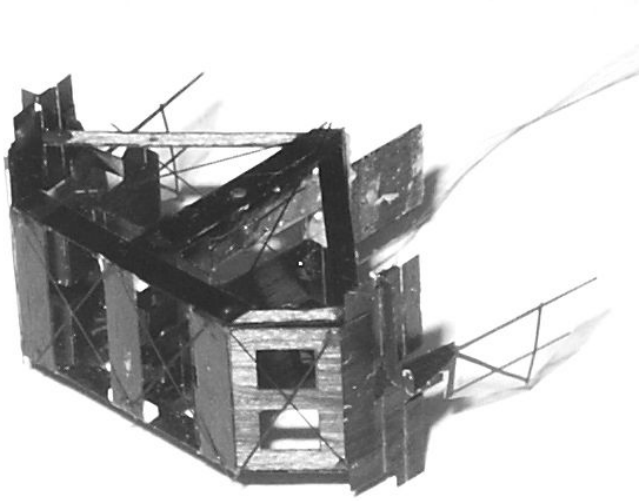

Figure 6.1: Most recent version of the 2DOF MFI.

joints and greater than 80 rigid members. One failure in any of these ensures that the MFI will not be able to generate the proper kinematics. Thus each component is connected in a non-permanent fashion to the airframe and thorax.

6.2 Characterization

One method of verification for the performance of the structure is to test whether it can generate enough lift to overcome it's body weight. To do this, a complete 4DOF MFI is developed and wired. Characterization is performed on the thorax dynamics by generating bode plots of each thorax. Each thorax is a two input two output system. It is desirable to have each four bar of the thorax mutually independent. This is accomplished by having as low a differential stiffness as possible, but it is also crucial that the wing inertia matrix be as close to diagonal as possible [3]. Thorax characterization is done via custom

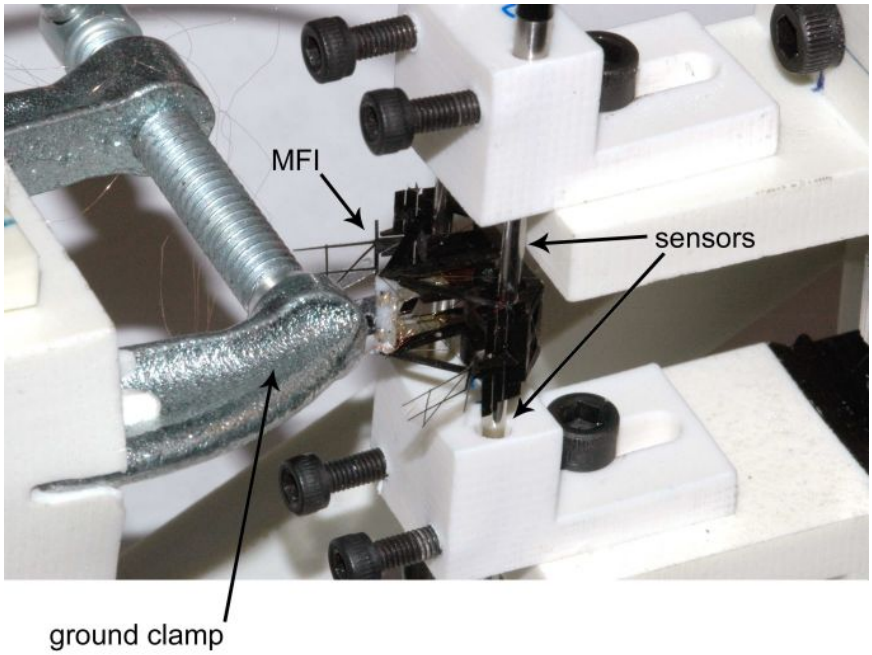

Figure 6.2: MFI in characterization nest.

built non-contact displacement sensors [80]. These sensors are positioned inside the four bar to watch the movement of the β link. A reflective triangle is connected to the interior of the β link to give adequate position resolution. The MFI in the characterization nest is shown in Figure 6.2.

The first test on the 4DOF MFI is to test for bilateral wing coupling. This is done by exciting one wing and measuring the displacement of each of the opposite four bars. The results of this are shown in Figure 6.3. To determine the significance of this coupling, and to characterize the structural dynamics the next step for a 4DOF MFI structure is to obtain system bode plots for each wing. This is done from the input voltage to the wing angular displacement. Since this is a 2×2 system, each wing will have four bode plots

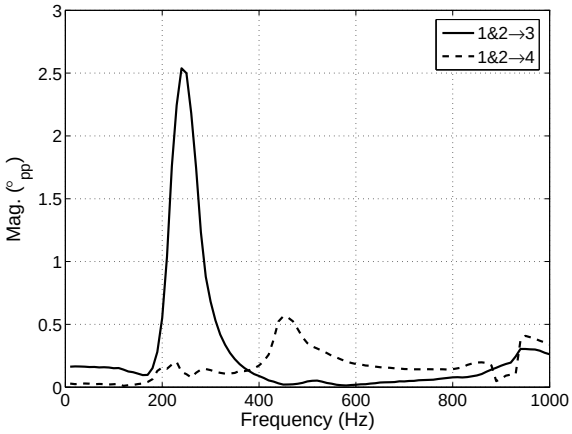

Figure 6.3: Bilateral wing coupling.

[3] representing the diagonal and off diagonal terms of the transfer function matrix. To create a controllable system in which the leading and trailing four bars can be actuated independently, the magnitudes of the off diagonal bode plots are desired to be kept as small as possible. The thorax structure itself is a nonlinear system, thus fitting to linear bode plots may not be sufficient to fully describe the system. The input-output characteristics of the system have nonlinearities associated with drive amplitudes, offsets, and possibly further parameters. As an initial compensation for this, the bode plots were taken while spanning the space of respective drive amplitudes and offsets until an optimal configuration was determined. These results are shown in Figure 6.4. From the results shown in Figure 6.4, the wing drive parameters (wing amplitudes, offsets, frequency, and phase) are determined. An example wing trajectory at DC is shown in Figure 6.5 while the trajectory at resonance is shown in Figure 6.6.

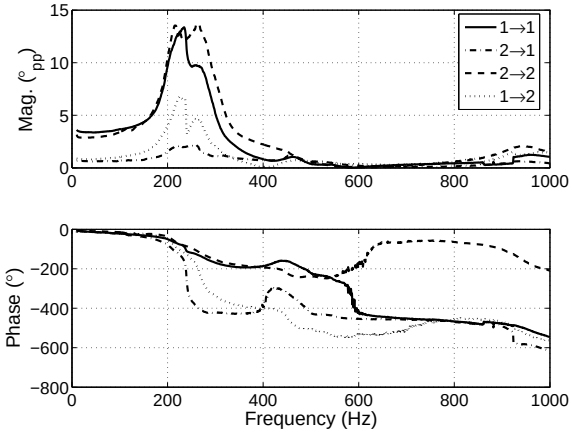

Figure 6.4: Example characterization results for one wing.

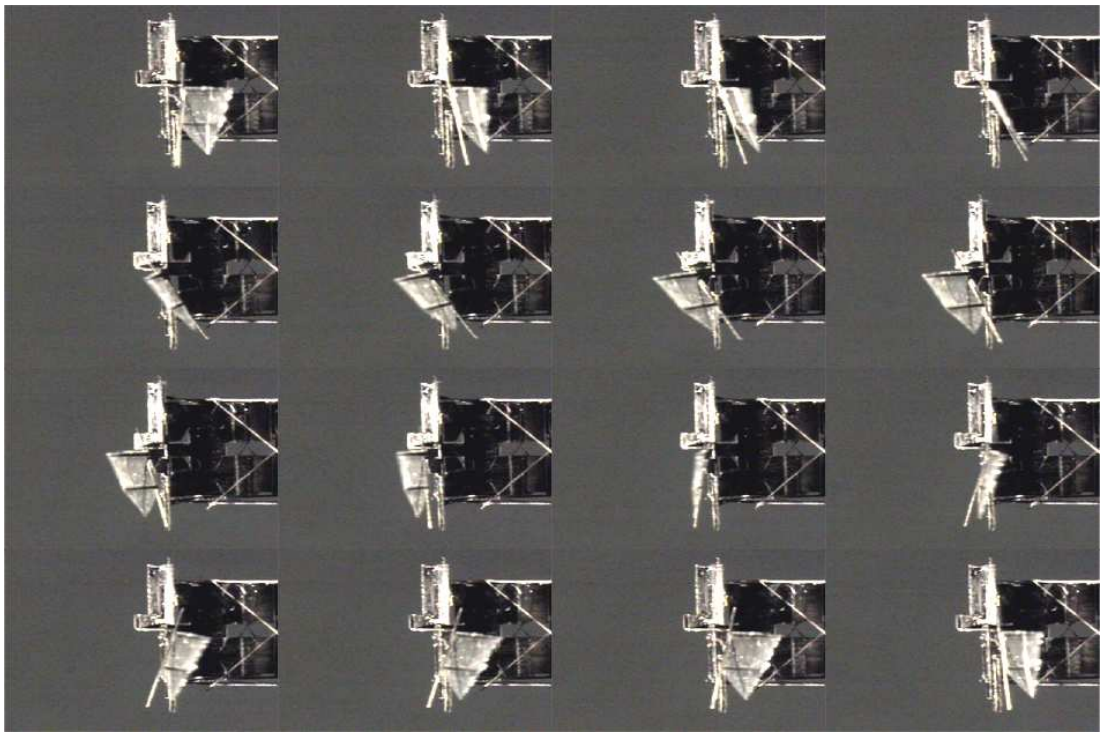

Figure 6.5: Image sequence from DC wing excitation.

Figure 6.6: Image sequence from resonance wing excitation.

6.3 Future Work

The claim is made in chapter 3 that the edge processing and crack closing techniques increase the fracture toughness of the actuators. To verify this, the toughness and ultimate stress of treated and control PZT samples should be examined via an accepted ASTM standard.

On the whole, to demonstrate the ability to generate sufficient lift, a take off test should be performed. This could be done by initially limiting the degrees of freedom while optimizing the lift force. Finally, the MFI could incrementally loose its "training wheels" while incorporating additional attitude sensors (from chapter 5) to obtain the final goal of

stable flight.

Insects typically initiate flight with a jump from their hind legs ([30]). This can be due to either the intimate connection between the leg muscles and the wing drive muscles, or the need to clear the ground before aerodynamic stability is achieved. Regardless, the MFI takeoff test should occur on a perch such that the wings are sufficiently clear of the ground.

Finally, to create an autonomous MFI, the power supply, high voltage amplifiers, and control circuitry needs to be shrunk to fit into the final mass budget.

Bibliography

[1] M. Algueró, B.L. Cheng, F. Guiu, M.J. Reece, M. Poole, and N. Alford. Degradation of the d_{33} piezoelectric coefficient for pzt under static and cyclic compressive loading. *Journal of the European Ceramic Society*, 21:1437–1440, 2001.

[2] W.T. Ang, F.A. Garmón, P.K. Kholsa, and C.N. Riviere. Modeling rate-dependent hysteresis in piezoelectric actuators. In *IEEE/RSJ International Conference on Intelligent Robots and Systems*, Las Vegas, Nevada, October 2003.

[3] S. Avadhanula, R.J. Wood, D. Campolo, and R.S. Fearing. Dynamically tuned design of the MFI thorax. In *IEEE International Conference on Robotics and Automation*, Washington, DC, May 2002.

[4] S. Avadhanula, R.J. Wood, E. Steltz, J. Yan, and R.S. Fearing. Lift force improvements for the micromechanical flying insect. In *IEEE/RSJ International Conference on Intelligent Robots and Systems*, Las Vegas, Nevada, October 2003.

[5] Arthur Ballato and Jan G. Smits. Network representation for piezoelectric bimorphs. *IEEE Transactions on Ultrasonics, Ferroelectrics, and Frequency Control*, 38(6):595–602, November 1991.

[6] S. K. Banala, Y. Karakaya, S. McIntosh, Z. Khan, and S. K. Agrawal. Design and optimization of a mechanism for out of plane insect wing motion with twist. In *Proc. of DETC, ASME Design Engineering Technical Conferences*, Salt Lake City, Utah, September 2004.

[7] Ron Barrett, Phillip Frye, and Michael Schliesman. Design, construction and characterization of a flightworthy piezoelectric solid state adaptive rotor. *Journal of Smart Materials and Structures*, 7:422–431, 1998.

[8] G. Barrows and C. Neely. Mixed-mode VLSI optic flow sensors for in-flight control of a micro air vehicle. In *SPIE* 45^{th} *Anual Meeting*, San Diego, CA, August 2000.

[9] J.M. Birch and M.H. Dickinson. Spanwise flow and the attachment of the leading-edge vortex of insect wings. *Nature*, 412:729–733, August 2001.

[10] C.R. Calladine. Buckminster Fuller's "tensegrity" structures and Clerk Maxwell's rules for the construction of stiff frames. *Int. J. Solids Structures*, 14:161–172, 1978.

[11] Domenico Campolo, Ranjana Sahai, and Ronald S. Fearing. Development of piezoelectric bending actuators with embedded piezoelectric sensors for micromechanical flapping mechanisms. In *IEEE International Conference on Robotics and Automation*, Taipei, Taiwan, September 2003.

[12] Javaan Chahl, Sarita Thakoor, Naig Le Bouffant, Gert Stange, M. V. Srinivasan, Butler Hine, and Steven Zornetzer. Bioinspired engineering of exploration systems: A horizon/attitude reference system based on the dragonfly ocelli for mars exploration applications. *Journal of Robotic Systems*, 20(1):35–42, 2003.

[13] S.A. Combes and T.L. Daniel. Flexural stiffness in insect wings i. scaling and the influence of wing venation. *Journal of Experimental Biology*, 206:2979–2987, 2003.

[14] S.A. Combes and T.L. Daniel. Flexural stiffness in insect wings ii. spacial distribution and dynamic wing bending. *Journal of Experimental Biology*, 206:2989–2997, 2003.

[15] Adam Cox, Ephrahim Garcia, and Michael Goldfarb. Actuator development for a flapping microrobotic microaerial vehicle. In *SPIE Conference on Microrobotics and Micromanipulation*, volume 3519, Boston, MA, November 1998.

[16] Adam Cox, Daniel Monopoli, Dragan Cveticanin, Michael Goldfarb, and Ephrahim Garcia. The development of elastodynamic components for piezoelectrically actuated flapping micro-air vehicles. In *Journal of Intelligent Material Systems and Structures*, volume 13, pages 611–615, September 2002.

[17] Adam Cox, Daniel Monopoli, Michael Goldfarb, and Ephrahim Garcia. The development of pizeoelectrically actuated micro-air vehicles. In *SPIE Conference on Microrobotics and Microassembly*, volume 3834, pages 101–108, Boston, Massachusetts, September 1999.

[18] S.H. Crandall. The role of damping in vibration theory. *J. of Sound and Vibration*, 11(1):3–18, 1970.

[19] D. Croft, G. Shed, and S. Devasia. Creep, hysteresis, and vibration compensation for piezoactuators: Atomic force microscopy application. *J. of Dynamic Systems, Measurement, and Control*, 123:35–43, March 2001.

[20] D. Croft, G. Shed, and S. Devasia. Creep, hysteresis, and vibration compensation for piezoactuators: Atomic force microscopy application. *Journal of Dynamic Systems, Measurement, and Control*, 123:35–43, 2001.

[21] J. M. Cruz-Hernández and V. Hayward. On the linear compensation of hysteresis. In *Proc. of the* 36^{th} *Conf. on Decision & Control*, pages 1956–1957, San Diego, California, December 1997.

[22] X. Deng, L. Schenato, and S. Sastry. Attitude control of a micromechanical flying insect including sensor and thorax models. In *IEEE International Conference on Robotics and Automation*, Taipei, Taiwan, September 2003.

[23] Don L. DeVoe and Albert P. Pisano. Modeling and optimal design of piezoelectric cantilever microactuators. *Journal of Microelectrical Mechanical Systems*, 6(3):266–270, September 1997.

[24] M. Dickinson, L. Tammero, and M. Tarstino. Sensory fusion in free-flight search behavior of fruit flies. In *Neurotechnology for Biomimetic Robots*, pages 573–591. The MIT Press, September 2002.

[25] M.H. Dickinson and K.G. Gotz. The wake dynamics and flight forces of the fruitfly *Drosophila Melanogaster*. In *Journal of Experimental Biology*, volume 199, pages 2085–2104, 1999.

[26] M.H. Dickinson, F.-O. Lehmann, and W.P. Chan. The control of mechanical power in insect flight. *Amer. Zool*, 38(4):718–728, 1998.

[27] M.H. Dickinson, F.-O. Lehmann, and S.P. Sane. Wing rotation and the aerodynamic basis of insect flight. *Science*, 284:1954–1960, June 1999.

[28] M.H. Dickinson and J.R.B. Lighton. Muscle efficiency and elastic storage in the flight motor of *Drosophila*. *Science*, 268:87–90, April 1995.

[29] M.H. Dickinson and M.S. Tu. The function of dipteran flight muscle. In *Comp. Biochem. Physiol.*, volume 116A, pages 223–238, 1997.

[30] R. Dudley. *The Biomechanics of Insect Flight: Form, Function and Evolution*. Princeton University Press, 1999.

[31] Thorbjörn Ebefors, Johan Ulfstedt Mattsson, Edvard Kälvesten, and Göran Stemme. A walking silicon micro-robot. In *The 10th Int Conference on Solid-State Sensors and Actuators (Transducers '99)*, pages 1202–1205, Sendai, Japan, June 1999.

[32] Eyal Elka, David Elata, and Haim Abramovich. The electromechanical response of multilayered piezoelectric structures. *Journal of Microelectrical Mechanical Systems*, 12(2):332–341, April 2004.

[33] C.P. Ellington, C. van der Berg, A.P. Willmott, and A.L.R. Thomas. Leading-edge vortices in insect flight. *Nature*, 384:626–630, December 1996.

[34] R.S. Fearing, S. Avadhanula, D. Campolo, M. Sitti, J. Yan, and R. Wood. A micromechanical flying insect thorax. In *Neurotechnology for Biomimetic Robots*, pages 469–480. The MIT Press, September 2002.

[35] R.S. Fearing, K.H. Chang, M. Dickinson, D.L. Pick, M. Sitti, and J. Yan. Wing

transmission for a micromechanical flying insect. In *IEEE International Conference on Robotics and Automation*, April 2000.

[36] T. Fett and G. Thun. Determination of room-temperature tensile creep of pzt. *Journal of Materials Science Letters*, 17:1929–1931, 1998.

[37] S.N. Fry, R. Sayaman, and M.H. Dickinson. The aerodynamics of free-flight maneuvers in *Drosophila*. *Science*, 300:495–498, April 2003.

[38] Michael Gogola, Gregory Fischer, Michael Goldfarb, and Ephrahim Garcia. The development of two piezoelectrically-actuated mesoscale robot quadrupeds. In *SPIE Conference on Microrobotics and Microassembly*, volume 3834, pages 76–84, Boston, Massachusetts, September 1999.

[39] M. Goldfarb and N. Celanovic. A lumped parameter electromechanical model for describing the nonlinear behavior of piezoelectric actuators. *Trans. of the ASME J. of Dynamic Systems, Measurement, and Control*, 119:478–485, September 1997.

[40] M. Goldfarb and J. E. Speich. A well-behaved revolute flexure joint for compliant mechanism design. *Journal of Mechanical Design*, 121:424–429, September 1999.

[41] Micheal Goldfarb, Michael Gogola, Gregory Fischer, Nikola Celanovic, Ivan Celanovic, and Ephrahim Garcia. A piezoelectrically actuated mesoscale robot quadruped. In *Neurotechnology for Biomimetic Robots*, pages 187–203. The MIT Press, September 2002.

[42] Nam Seo Goo, Cheol Kim, Young-Doo Kwon, and Kwang Joon Yoon. Behaviors and

performance evaluation of a lightweight piezo-composite curved actuator. *Journal of Intelligent Material Systems and Structures*, 12:639–646, September 2001.

[43] William E. Green and Paul Y. Oh. An aerial prototype for situational awareness in closed quarters. In *IEEE/RSJ International Conference on Intelligent Robots and Systems*, pages 61–66, Las Vegas, Nevada, October 2003.

[44] William E. Green, Paul Y. Oh, Keith Sevcik, and Geoffrey Barrows. Autonomous landing for indoor flying robots using optic flow. In *ASME International Mechanical Engineering Congress*, Washington, DC, November 2003.

[45] H. T. Hahn and N. J. Pagano. Curing stresses in composite laminates. *Journal of Composite Materials*, 9(1):91–106, January 1975.

[46] H. T. Hahn and S. W. Tsai. Nonlinear elastic behavior of unidirectional composite laminae. *Journal of Composite Materials*, pages 102–118, January 1973.

[47] S. Hollar, A. Flynn, C. Bellew, and K.S.J. Pister. Solar powered 10mg silicon robot. In *MEMS*, Kyoto, Japan, January 2003.

[48] M.W. Hyer and A. Jilani. Predicting the deformation characteristics of rectangular unsymmetrically laminated piezoelectric materials. *Journal of Smart Materials and Structures*, 7:784–791, 1998.

[49] M.R. Kermani, M. Moallem, and R.V. Patel. Optimizing the performance of piezoelectric actuators for active vibration control. In *IEEE International Conference on Robotics and Automation*, Washington, DC, May 2002.

[50] Hazem Kioua and Shaukat Mirza. Piezoelectric induced bending and twisting of laminated composite shallow shells. *Journal of Smart Materials and Structures*, 9:476–484, 2000.

[51] F.-O. Lehmann and M.H. Dickinson. The changes in power requirements and muscle efficiency during elevated force production in the fruit fly *Drosophila Melanogaster*. *Journal of Experimental Biology*, 200:1133–1143, 1997.

[52] F.-O. Lehmann and M.H. Dickinson. The production of elevated flight force compromises manoeuverability in the fruit fly *Drosophila Melanogaster*. *Journal of Experimental Biology*, 204:627–635, 2001.

[53] Guang Li, Eugene Furman, and Gene H. Haertling. Stress-enhanced displacements in PLZT rainbow actuators. *Journal of the American Ceramic Society*, 80(6):1382–1388, 1997.

[54] Nicolae Lobontiu, Michael Goldfarb, and Ephrahim Garcia. Achieving maximum tip displacement during resonant excitation of piezoelectrically actuated beams. *Journal of Intelligent Material Systems and Structures*, 10, November 1999.

[55] L.E. Malvern. *Introduction to the Mechanics of a Continuous Medium*. Prentice-Hall, Englewood Cliffs, NJ, 1969.

[56] S.W. Meeks and R. W. Timme. Effects of one-dimensional stress on piezoelectric ceramics. *Journal of Applied Physics*, 46(10):4334–4338, October 1975.

[57] Robert C. Michelson. The entomopter. In *Neurotechnology for Biomimetic Robots*, pages 481–509. The MIT Press, September 2002.

[58] Yong-Mo Moon, Brian Patrick Trease, and Sridhar Kota. Design of large-displacement compliant joints. In *Proceddings of DETC'02: MECH 27th Biennial Mechanisms and Robotics Conference*, Montreal, Canada, October 2002.

[59] G. Nalbach. The halteres of the blowfly *Calliphora* i. kinematics and dynamics. *Journal of Comparative Physiology A*, 173:293–300, 1993.

[60] G. Nalbach and R. Hengstenberg. The halteres of the blowfly *Calliphora* ii. three-dimensional organization of compensatory reactions to real and simulated rotations. *Journal of Comparative Physiology A*, 175:695–708, 1994.

[61] Craig D. Near. Piezoelectric actuator technology. In *SPIE Smart Structures and Materials: Smart Structures and Integrated Systems*, San Diego, California, February 1996.

[62] Jean-D. Nicoud and Jean-C. Zufferey. Towards indoor flying robots. In *IEEE/RSJ International Conference on Intelligent Robots and Systems*, pages 787–792, Lausanne, Switzerland, October 2002.

[63] N. J. Pagano and H. T. Hahn. Evaluation of composite curing stresses. In *Composite Materials: Testing and Design (Fourth Conference), ASTM STP 617*, pages 317–329. American Society for Testing and Materials, 1977.

[64] Seung-Eek Park and Thomas R. Shrout. Ultrahigh strains and piezoelectric behavior in relaxor based ferroelectric single crystals. *Journal of Applied Physics*, 82(4):1804–1811, August 1997.

[65] Jérôme Pasquero and Vincent Hayward. STReSS: A practical tactile display system with one millimeter spatial resolution and 700hz refesh rate. In *Proc. Eurohaptics*, pages 94–110, 2003.

[66] Jérôme Pasquero, Vincent Lévesque, Vincent Hayward, and Maryse Legault. Display of virtual braille dots by lateral skin deformation: A pilot study. In *Proc. Eurohaptics*, Munich, Germany, June 2004.

[67] T. N. Pornsin, S. W. Lee, H. Nassef, J. Grasmeyer, Y. C. Tai, C. M. Ho, and M. Keennon. Mems wing technology for a battery powered ornithopter. In *The* 13_{th} *IEEE Anual Intl. Conf. on MEMS*, pages 709–804, Miyazaki, Japan, January 2000.

[68] T. N. Pornsin-shiriak, Y. C. Tai, H. Nassef, and C. M. Ho. Titanium-alloy mems wing technology for a micro aerial vehicle application. *Journal of Sensors and Actuators, A: Physical*, 89:95–103, March 2001.

[69] Adam J Rutkowski, Shaun Edwards, Mark A. Willis, Roger D. Quinn, and Gregory C. Causey. A robotic platform for testing moth-inspired plume tracking strategies. In *IEEE International Conference on Robotics and Automation*, New Orleans, Lousiana, May 2004.

[70] J. Schäfer and H. Janocha. Compenstion of hysteresis in solid-state actuators. *Journal of Sensors and Actuators A: Physical*, 49:97–102, 1995.

[71] H. Schuppe and R. Hengstenberg. Optical properties of the ocelli of *Calliphora erythrocephala* and their role in the dorsal light response. *Journal of Comparative Physiology A*, 173:143–149, 1993.

[72] A. Sherman and M.H. Dickinson. A comparison of visual and haltere-mediated equilibrium reflexes in the fruit fly *Drosophila melanogaster*. *Journal of Experimental Biology*, 206:295–302, 2003.

[73] E. Shimada, J.A. Thompson, J. Yan, R.J. Wood, and R.S. Fearing. Prototyping millirobots using dextrous microassembly and folding. In *Symposium on Microrobotics ASME Int. Mechanical Engineering Cong. and Exp.*, November 2000.

[74] Yasuhide Shindo, Heihachiro Murakami, Katsumi Horiguchi, and Fumio Narita. Evaluation of electric fracture properties of piezoelectric ceramics using the finite element and single-edge precracked-beam methods. *Journal of the American Ceramic Society*, 85(5):1243–1248, 2002.

[75] U. Singh and R.S. Fearing. Tactile after-images from static contact. In 7^{th} *Symp. on Haptic Interfaces for Virtual Environment and Teleoperator Systems ASME IMECE*, Anaheim, CA, November 1998.

[76] Metin Sitti, Domenico Campolo, Joseph Yan, Ronald S. Fearing, Tao Su, David Taylor, and Timothy D. Sands. Development of pzt and pzn-pt based unimorph actuators for micromechanical flapping mechanisms. In *IEEE International Conference on Robotics and Automation*, Seoul, Korea, May 2001.

[77] Jan G. Smits and Arthur Ballato. Dynamic admittance of piezoelectric cantilever bimorphs. *Journal of Microelectrical Mechanical Systems*, 3(3):105–112, September 1994.

[78] Jan G. Smits and Wai shing Choi. The constituent equations of piezoelectric hetero-

geneous bimorphs. *IEEE Transactions on Ultrasonics, Ferroelectrics, and Frequency Control*, 38(3):256–270, May 1991.

[79] M. V. Srinivasan, J. S. Chahl, K. Weber, S. Venkatesh, M. G. Nagle, and S. W. Zhang. Robot navigation inspired by principles of insect vision. *Robotics and Autonomous Systems*, 26:203–216, 1999.

[80] E. Steltz, R.J. Wood, S. Avadhanula, and R.S. Fearing. Characterization of the micromechanical flying insect by optical position sensing. In *IEEE International Conference on Robotics and Automation*, 2005.

[81] S. Sunada and C.P. Ellington. A new method for explaining the generation of aerodynamic forces in flapping flight. *Mathematical Methods in the Applied Sciences*, 24:1377–1386, 2001.

[82] S. Sunada, T. Yasuda, K. Yasuda, and K. Kawachi. Comparison of wing characteristics at an ultralow reynolds number. *Journal of Aircraft*, 39(2):331–338, 2002.

[83] Ellad B. Tadfor and Gábor Kósa. Electromechanical coupling correction for piezoelectric layered beams. *Journal of Microelectrical Mechanical Systems*, 12(6), December 2003.

[84] Toshio Tanimoto, Kiyoshi Okazaki, and Kohji Yamamoto. Tensile stress-strain behavior of piezoelectric ceramics. *Journal of Applied Physics*, 32:4233–4236, 1993.

[85] Takaaki Tsurumi, Young-Bae Kil, Kouhei Nagatoh, Hirofumi Kakemoto, Satoshi Wada, and Sadayuki Takahashi. Intrinsic elastic, dielectric, and piezoelectric losses in

lead zirconate titanate ceramics determined by an immittance-fitting method. *Journal of the American Ceramic Society*, 85(8):1993–1996, 2002.

[86] D. Viehland, L. Ewart, J. Powers, and J. F. Li. Stress dependence of the electromechanical properties of $Pb(Mg_{1/3}Nb_{2/3})O_3-PbTiO_3$ crystals: Performance advantages and limitations. *Journal of Applied Physics*, 90(5):2479–2483, September 2001.

[87] Qing-Ming Wang and L. Eric Cross. Constituative equations of symmetrical triple layer piezoelectric benders. *IEEE Transactions on Ultrasonics, Ferroelectrics, and Frequency Control*, 46(6):1343–1351, November 1999.

[88] Qing-Ming Wang and L. Eric Cross. Tip deflection and blocking force of soft PZT-based cantilever RAINBOW actuators. *Journal of the American Ceramic Society*, 82(1):103–110, 1999.

[89] Qing Ming Wang and L. Eric Cross. Estimation of the effective d_{31} coefficients of the piezoelectric layer in rainbow actuators. *Journal of the American Ceramic Society*, 84(11):2563–2569, 2001.

[90] Qing-Ming Wang, Xiao-Hong Du, Baomin Xu, and L. Eric Cross. Electromechanical coupling and output efficiency of piezoelectric bending actuators. *IEEE Transactions on Ultrasonics, Ferroelectrics, and Frequency Control*, 46(3):638–46, May 1999.

[91] Qing-Ming Wang, Qiming Zhang, Baomin Xu, Ruibin Liu, and L. Eric Cross. Nonlinear piezoelectric behavior of ceramic bending mode actuators under strong electric fields. *Journal of Applied Physics*, 86(6):3352–3360, September 1999.

[92] Z.J. Wang, J.M. Birch, and M.H. Dickinson. Unsteady forces and flows in low reynolds number hovering flight: two-dimensional computations *vs* robotic wing experiments. *Journal of Experimental Biology*, 207:449–460, 2004.

[93] Marc S. Weinberg. Working equations for piezoelectric actuators and sensors. *Journal of Microelectrical Mechanical Systems*, 8(4):529–533, December 1999.

[94] Stephanie A. Wise. Displacement properties of RAINBOW and THUNDER piezoelectric actuators. *Journal of Sensors and Actuators A: Physical*, 69:33–38, 1998.

[95] R.J. Wood. Flight force measurements for a micromechanical flying insect. Master's thesis, University of California at Berkeley, December 2001.

[96] R.J. Wood, S. Avadhanula, M. Menon, and R.S. Fearing. Microrobotics using composite materials: The micromechanical flying insect thorax. In *IEEE International Conference on Robotics and Automation*, Taipei, Taiwan, September 2003.

[97] R.J. Wood and R.S. Fearing. Flight force measurements for a micromechanical flying insect. In *IEEE/RSJ International Conference on Intelligent Robots and Systems*, Maui, HI, October 2001.

[98] R.J. Wood, E. Steltz, and R.S. Fearing. Optimal energy density piezoelectric bending actuators. *Journal of Sensors and Actuators A: Physical*, 1(1):1–13, 2004.

[99] R.J. Wood, E. Steltz, and R.S. Fearing. Nonlinear performance limits for high energy density piezoelectric bending actuators. In *In Review: IEEE International Conference on Robotics and Automation*, April 2005.

[100] W.C. Wu, L. Schenato, R.J. Wood, and R.S. Fearing. Biomimetic sensor suite for flight control of a micromechanical flying insect: Design and experimental results. In *IEEE International Conference on Robotics and Automation*, Taipei, Taiwan, September 2003.

[101] W.C. Wu, R.J. Wood, and R.S. Fearing. Halteres for the micromechanical flying insect. In *IEEE International Conference on Robotics and Automation*, Washington, DC, May 2002.

[102] J. Yan. *Design, Fabrication and Wing Force Control for a Micromechanical Flying Insect*. PhD thesis, University of California at Berkeley, December 2002.

[103] J. Yan, R.J. Wood, S. Avadhanula, and M. Sitti amd R.S. Fearing. Towards flapping wing control for a micromechanical flying insect. In *IEEE International Conference on Robotics and Automation*, Seoul, Korea, May 2001.

[104] G. Yang, S.-F. Liu, W. Ren, and B. K. Mukherjee. Uniaxial stress dependence of the piezoelectric properties of lead zirconate titanate ceramics. In *Proceedings of the 2000 12th IEEE International Symposium on Applications of Ferroelectrics*, pages 431–434, 2001.

[105] R. Yeh, S. Hollar, and K.S.J. Pister. Design of low-power silison articulated microrobots. *Journal of Micromechatronics*, 1(3):191–203, 2002.

[106] R. Yeh, E.J.J. Kruglick, and K.S.J. Pister. Surface-micromachined components for articulated microrobots. *Journal of Microelectrical Mechanical Systems*, 5(1):10–17, March 1996.

[107] Jianhua Yin, Bei Jiang, and Wenwu Cao. Elastic, piezoelectric, and dielectric properties of $0.995Pb(Zn_{1/3}Nb_{2/3})O_3 - 0.45PbTiO_3$ single crystal with designed multidomains. *IEEE Transactions on on Ultrasonics, Ferroelectrics, and Frequency Control*, 47(1):285–291, January 2000.

[108] K Joon Yoon, Seokjun Shin, Hoon C Park, and Nam Seo Goo. Design and manufacture of a lightweight piezo-composite actuator. *Journal of Smart Materials and Structures*, 11:163–168, 2002.

[109] Huai yu Wu, Dong Sun, Zhao ying Zhou, Shen shu Xiong, and Xiao hao Wang. Micro air vehicle: Architecture and implementation. In *IEEE International Conference on Robotics and Automation*, pages 534–539, Taipei, Taiwan, September 2003.

[110] Huai yu Wu, Zhao ying Zhou, and Dong Sun. Autonomous hovering control and test for micro air vehicle. In *IEEE International Conference on Robotics and Automation*, pages 528–533, Taipei, Taiwan, September 2003.

[111] R. Żbikowski. On aerodynamic modelling of an insect-like flapping wing in hover for micro air vehicles. *Phil. Trans. R. Soc. Lond.*, 360:273–290, 2002.

[112] Q. M. Zhang, Jianzhong Zhao, and Jiehui Zheng. Change of the weak-field properties of $Pb(ZrTi)O_3$ piezoceramics with compressive stresses and its links to the effect of dopants on the stability of the polarizations in the materials. *Journal of Materials Research*, 12(1):226–234, 1997.

[113] Mei-Ling Zhu, Shi-Wei Ricky Lee, Hing-Leung Li, Tong-Yi Zhang, and Pin Tong. Modeling of torsional vibration induced by extension-twisting coupling of anisotropic

composite laminates with piezoelectric actuators. *Journal of Smart Materials and Structures*, 11:55–62, 2002.

[114] Jean-Christophe Zufferey, Antoine Beyeler, and Dario Floreano. Vision-based navigation from wheels to wings. In *IEEE/RSJ International Conference on Intelligent Robots and Systems*, page 29682973, Las Vegas, Nevada, October 2003.

Appendix A

Appendix A: Example Applications

Search and rescue, hazardous environment exploration, and surveillance are a few of the obvious scenarios to which the MFI would be suitable.

One feature of the MFI is the low cost inherent in both the scale and material selection. Fleets of hundreds or thousands of MFIs can effectively explore areas with computationally simple dispersion techniques. For example, if each MFI is equipped with a radio transceiver, an individual MFI could attempt to maximize the distance to its nearest neighbor by minimizing the received signal strength. This concept is shown in Figure A.1. One example of a complex environment is the rubble created by a collapsed building. MFIs could explore areas which would be inaccessible to either search crews or existing mobile robots. When fitted with simple sensors (for example a $C0_2$ sensor), survivors could hypothetically be located. An artist's rendition of a group of MFI scouts in a collapsed building is shown in Figure A.2. Micro air vehicles with the ability to hover have a huge advantage for use in cluttered urban environments. An example of this application is in

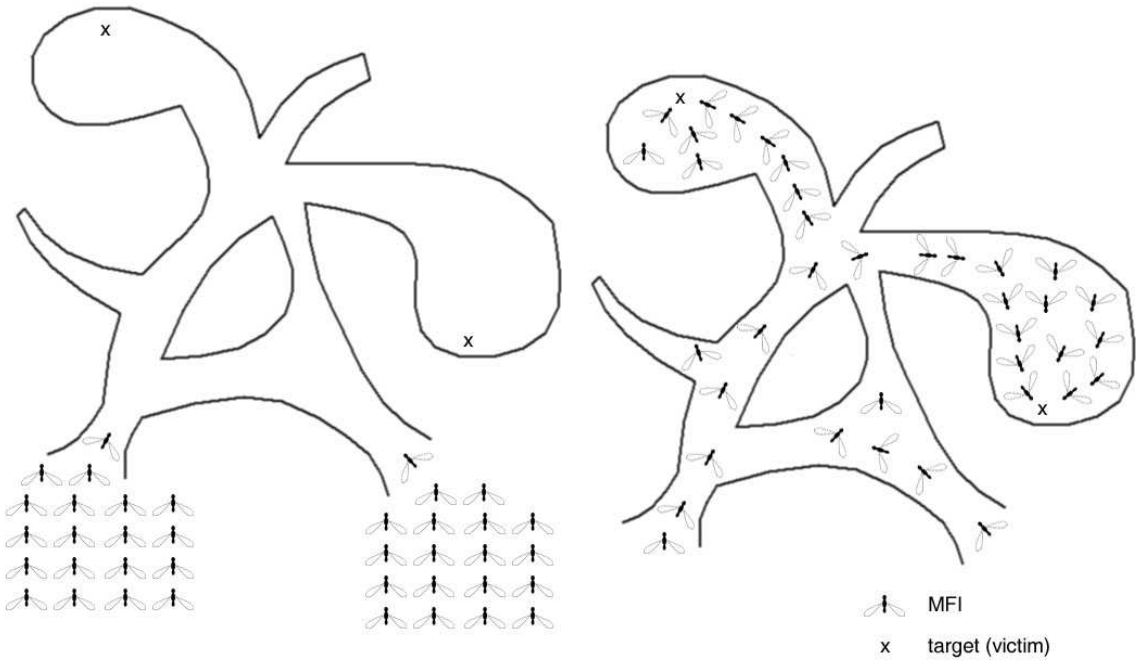

Figure A.1: Swarms of MFIs entering (a) and percolating through a complex area (b).

assisting police units to either be aware of their environment or track suspect vehicles. This concept is shown in Figure A.3.

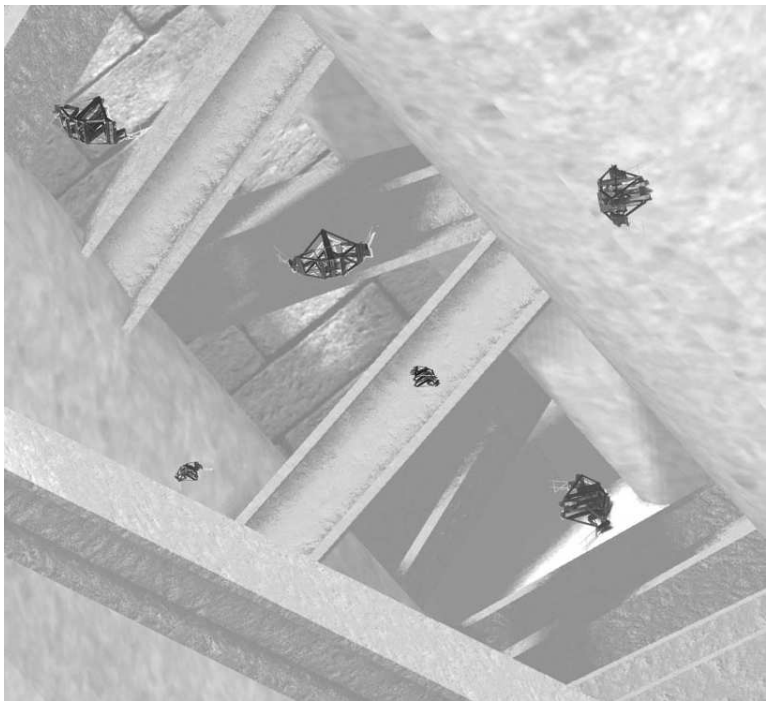

Figure A.2: MFIs navigating through rubble.

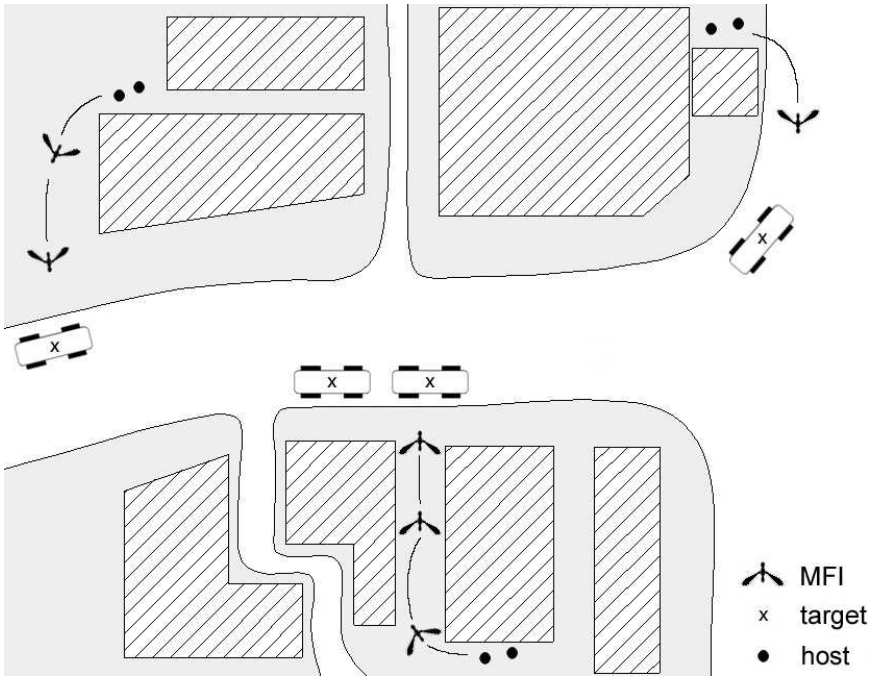

Figure A.3: MFIs navigating an urban environment

Appendix B

Appendix B: Actuator Failure

Further verification of the fracture mechanics model described in section 3.2 and of the strain uniformity described in chapter 3 is given by observations of the actuator failure. Two failure modes, electrical breakdown and mechanical fracture, are observed and associated with the assumptions presented in chapter 3. First, the actuator is subjected to higher and higher fields to test whether mechanical or electrical failure occurs first. This is done for the case of a unimorph and bimorph actuators to isolate mechanical and electrical failure. In the case of the unimorph, electrical failure occurs at approximately $5.5V\mu m^{-1}$ while the bimorph fractures when approximately $3.2V\mu m^{-1}$ is applied. For the case of the bimorph fracture, the piezoelectric plate which is not being driven is unanimously where fracture occurs. From the fact that the unimorph experiences electrical breakdown prior to fracture justifies the bimorph fracture as well as the fracture mechanics model of the PZT. It was stated in section 3.2 that while the piezoelectric effect creates a strain in a free plate, it creates no local stresses. When used in a bimorph configuration, the piezoelectric plate

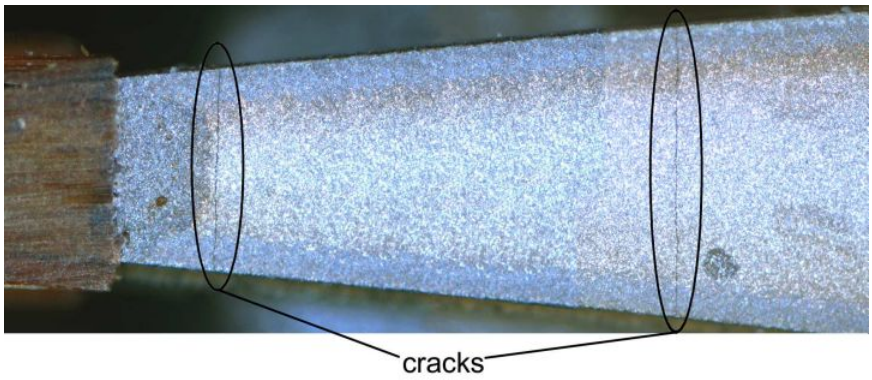

Figure B.1: Example of PZT surface with multiple cracks.

experiencing a field will see stresses only due to its interfacial conditions, and these will be compressive. Alternatively, the passive plate will experience the highest tensile stresses and will thus cause fracture prior to breakdown.

With respect to stress uniformity, the passive plate is expected to fracture at a relatively random location along the x axis, as opposed to at the proximal end for a rectangular actuator. Note that this is true for only external loads. For internal piezoelectric loads on the passive plate a uniform moment is created by the active layer in both the case of the actuators described in chapter 3 as well as for rectangular cantilever actuators. Thus a number of actuators were mounted and had a load applied to the distal end of the extension which increased monotonically to fracture. Invariably, it was not possible to predict exactly where the fracture would occur (sometimes in numerous places), however it was universal that the fracture occurred parallel to the y axis. These cracks always spanned the entire width of the actuator verifying the importance of improving the edge conditions. An example of a fractured actuator is shown in Figure B.1.